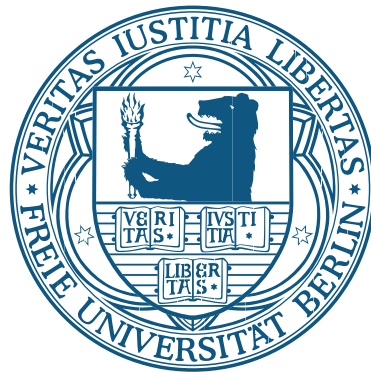# Optimization of a
Controlled Phasegate
for Ultracold Calcium Atoms
in an Optical Lattice

Diplomarbeit

Michael Goerz

April 1, 2010
Fachbereich Physik
Freie Universität Berlin
Supervisor: Dr. Christiane Koch

Thanks and Acknowledgments

Contents

Chapter 1

Introduction

There are two motivations for quantum computing, the processing of information through the basic quantum properties of matter. One is pragmatic: According to Moore's well-known law, the number of transistors on an integrated circuit follows an exponential curve, doubling about every 24 months. We could also reformulate this to say that the number of atoms required for a given computation decreases exponentially. At some point in the next few decades, we will arrive at the limit of a single atom, prompting the question: How can we perform a computation at this atomic level? Traditional microelectronics will already break down when the structures inside computer chips become so small that they are dominated by quantum effects. In this light, there is no alternative to looking for more fundamental ways of computing if we want to continue increasing computing power.

The other motivation is more visionary: Can we find the concepts of information and computation in the most fundamental laws of physics? Does the universe in its building blocks contain the power to perform computations? Can we find ways of processing information that are fundamentally more basic and more powerful than what we have today?

From both perspectives, we arrive at quantum computing. In quantum computation, information is stored in the eigenstates of some quantized property, which then can be manipulated according to the laws of quantum mechanics.

1.1 Qubits

A *bit* is the basic building block of a classical computer. In quantum computation, we replace this with a quantum bit, or *qubit* for short. Just like a bit, which has the logical values 0 and 1, physically encoded in low or high voltage in an electronic circuit, the qubit has logical values $|0\rangle$ and $|1\rangle$, encoded in two eigenstates of a quantum mechanical system. What makes the qubit unique compared to the classical bit, is that not only it can be $|0\rangle$ or $|1\rangle$, but also any superposition of the two. The state of the qubit can be written as

$$|\Psi\rangle = \alpha_0 |0\rangle + \alpha_1 |1\rangle \, ; \qquad |\alpha_0|^2 + |\alpha_1|^2 = 1, \qquad (1.1)$$

with two complex amplitudes α_0 and α_1. According to the laws of quantum mechanics, this means that if a measurement is performed on a qubit in the state $|\Psi\rangle$, it will come out as $|0\rangle$ with a probability of $|\alpha_0|^2$ and as $|1\rangle$ with a probability of $|\alpha_1|^2$. In that sense a qubit can be 30% $|0\rangle$ and 70% $|1\rangle$ (for example), at the same time. Mathematically, the qubit is defined in a two-dimensional Hilbert space with the basis states $|0\rangle$ and $|1\rangle$.

Often, qubits are represented intuitively as pointers in the Bloch sphere, shown in Figure 1.1.
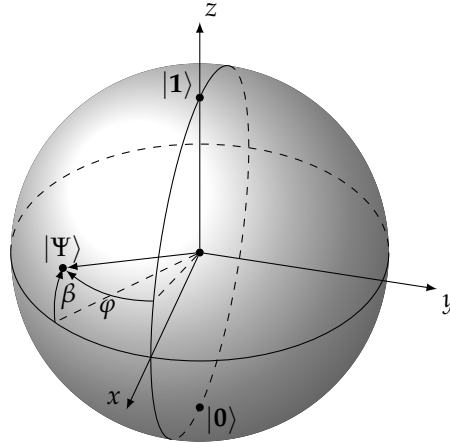
Figure 1.1: Bloch sphere representation of a single qubit

To go to the Bloch description, Equation (1.1) is rewritten as

$$|\Psi\rangle = e^{i\gamma}\left(\cos\frac{\theta}{2}\,|0\rangle + e^{i\varphi}\sin\frac{\theta}{2}\,|1\rangle\right); \qquad \theta \equiv \frac{\pi}{2} - \beta. \tag{1.2}$$

Instead of the original α_0, α_1, the qubit is now described by $\theta \in [0, \pi]$, which is the angle from the z-axis, and $\varphi \in [0, 2\pi]$, which is the angle from the x-axis. The global phase γ has no consequence for any measurement of observables and is not represented in the Bloch sphere picture.

We have described the qubit abstractly as a quantum mechanical two-level system, where one level is labeled $|0\rangle$ and the other is labeled $|1\rangle$. What these levels are physically is of secondary importance, as long as we can make sure that any measurement will find either $|0\rangle$ or $|1\rangle$, that we can manipulate the qubit controllably, and that the information in the qubit is stable (low decoherence). One of the simplest physical systems that fits this description is the spin of a single electron, which can be either up ($|1\rangle$) or down ($|0\rangle$) and is a natural two-level system. However, we can also encode a qubit in more complicated physical systems as long as the above conditions are met. In this thesis, we will use the electronic levels of a Calcium atom to encode the qubit. We simply pick two "suitable" levels from the spectrum and label them $|0\rangle$ and $|1\rangle$. The qubit encoding in Calcium will be the topic of Chapter 2.

Instead of writing the qubit as an expansion into the eigenstates in Equation (1.1), we can also represent it as a vector of the two complex amplitudes

α_0 and α_1:

$$|\Psi\rangle = \alpha_0 \begin{pmatrix} 1 \\ 0 \end{pmatrix} + \alpha_1 \begin{pmatrix} 0 \\ 1 \end{pmatrix} = \begin{pmatrix} \alpha_0 \\ \alpha_1 \end{pmatrix} \tag{1.3}$$

In order to describe a collection of two qubits, we combine the two one-qubit Hilbert spaces with a Kronecker product to get a four-dimensional two-qubit Hilbert space. A two-qubit state can then be written as

$$|\Psi\rangle_{2q} = \alpha_{00}(|0\rangle \otimes |0\rangle) + \alpha_{01}(|0\rangle \otimes |1\rangle) + \alpha_{10}(|1\rangle \otimes |0\rangle) + \alpha_{11}(|1\rangle \otimes |1\rangle)$$
$$\equiv \alpha_{00}|00\rangle + \alpha_{01}|01\rangle + \alpha_{10}|10\rangle + \alpha_{11}|11\rangle \tag{1.4}$$

If the two-qubit state is just the simple combination of two individually defined single qubits, the first one with coefficients α_0, α_1, the second one with coefficients β_0, β_1, then the two-qubit coefficients are

$$\alpha_{00} = \alpha_0\beta_0 \qquad \alpha_{01} = \alpha_0\beta_1 \qquad \alpha_{10} = \alpha_1\beta_0 \qquad \alpha_{11} = \alpha_1\beta_1. \tag{1.5}$$

Generally, though, there are also coefficients α_{00}, α_{01}, α_{10}, α_{11} that cannot be split into one-qubit coefficients α_0, α_1, β_0, β_1. If the coefficients decompose as in Equation (1.5), the two individual qubits are called *separable* and the two-qubit state is

$$|\Psi\rangle_{2q} = |\Psi\rangle_\alpha \otimes |\Psi\rangle_\beta \tag{1.6}$$

Otherwise, they are *entangled*, and no such separation is possible. The most well-known examples for entangled two-qubit states are the Bell states, one of which is

$$\left|\Phi^+\right\rangle = \frac{1}{\sqrt{2}}\left(|00\rangle + |11\rangle\right). \tag{1.7}$$

A two-qubit state can also be represented as a vector, in the same way we did for the one-qubit states:

$$|\Psi\rangle_{2q} = \begin{pmatrix} \alpha_{00} \\ \alpha_{01} \\ \alpha_{10} \\ \alpha_{11} \end{pmatrix} \tag{1.8}$$

1.2 Quantum Gates

Quantum states can be modified by unitary *operators* $\hat{O}$:

$$|\Psi\rangle \xrightarrow{\hat{O}} |\Psi\rangle' \quad \Leftrightarrow \quad |\Psi\rangle' = \hat{O}|\Psi\rangle \tag{1.9}$$

When we represent the states as vectors, the operators are complex unitary matrices. The unitarity guarantees that the norm of the states (i.e. the sum of probabilities) stays 1:

$$\sum_i |\alpha_i'|^2 = \sum_i |\alpha_i|^2 = 1 \tag{1.10}$$

In principle, there is an infinite number of operators, that is unitary 2×2 or 4×4 matrices. In practice, there is a manageable set of commonly used operators. In Section 1.4 we will see that a small selection of operators is sufficient to perform any quantum computation.
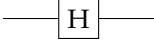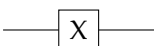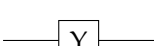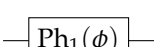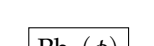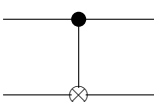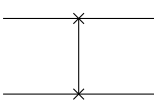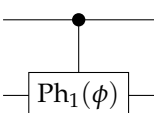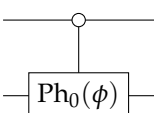
Name	Circuit Symbol	Operator Matrix
Hadamard	$\boxed{\text{H}}$	$\hat{H} = \frac{1}{\sqrt{2}} \begin{pmatrix} 1 & 1 \\ 1 & -1 \end{pmatrix}$
Pauli-X	$\boxed{\text{X}}$	$\hat{X} = \begin{pmatrix} 0 & 1 \\ 1 & 0 \end{pmatrix}$
Pauli-Y	$\boxed{\text{Y}}$	$\hat{Y} = \begin{pmatrix} 0 & -i \\ i & 0 \end{pmatrix}$
Pauli-Z	$\boxed{\text{Z}}$	$\hat{Z} = \begin{pmatrix} 1 & 0 \\ 0 & -1 \end{pmatrix}$
Phasegate (1)	$\boxed{\text{Ph}_1(\phi)}$	$\text{Ph}_1(\phi) = \begin{pmatrix} 1 & 0 \\ 0 & e^{i\phi} \end{pmatrix}$
Phasegate (0)	$\boxed{\text{Ph}_0(\phi)}$	$\text{Ph}_0(\phi) = \begin{pmatrix} e^{i\phi} & 0 \\ 0 & 1 \end{pmatrix}$
Controlled-Not		$CNOT = \begin{pmatrix} 1 & 0 & 0 & 0 \\ 0 & 1 & 0 & 0 \\ 0 & 0 & 0 & 1 \\ 0 & 0 & 1 & 0 \end{pmatrix}$
Swap		$SWAP = \begin{pmatrix} 1 & 0 & 0 & 0 \\ 0 & 0 & 1 & 0 \\ 0 & 1 & 0 & 0 \\ 0 & 0 & 0 & 1 \end{pmatrix}$
Controlled-Phasegate (11)	$\boxed{\text{Ph}_1(\phi)}$	$\text{CPHASE}_{11}(\phi) = \begin{pmatrix} 1 & 0 & 0 & 0 \\ 0 & 1 & 0 & 0 \\ 0 & 0 & 1 & 0 \\ 0 & 0 & 0 & e^{i\phi} \end{pmatrix}$
Controlled-Phasegate (00)	$\boxed{\text{Ph}_0(\phi)}$	$\text{CPHASE}_{00}(\phi) = \begin{pmatrix} e^{i\phi} & 0 & 0 & 0 \\ 0 & 1 & 0 & 0 \\ 0 & 0 & 1 & 0 \\ 0 & 0 & 0 & 1 \end{pmatrix}$

Table 1.1: Common one- and two-qubit operators

A selection of one-qubit operators is shown in the upper part of Table 1.1.

The Hadamard gate transforms each one-qubit eigenstate into a superposition with the other one. The Pauli-X gate flips the population of the two levels $|0\rangle$ and $|1\rangle$: $\alpha_0 \leftrightarrow \alpha_1$. This could be interpreted as a quantum-logical NOT-operation, as the input state $|0\rangle$ is changed to $|1\rangle$ and $|1\rangle$ is changed to $|0\rangle$. The Pauli-Z gate flips $|1\rangle$ to $-|1\rangle$. The Pauli-X, Pauli-Y, Pauli-Z operators are also important in the Bloch sphere picture (Figure 1.1), as they give rise to the *rotation operators*

$$\hat{R}_x(\vartheta) \equiv e^{i\vartheta\hat{X}/2}; \quad \hat{R}_y(\vartheta) \equiv e^{i\vartheta\hat{Y}/2}; \quad \hat{R}_z(\vartheta) \equiv e^{i\vartheta\hat{Z}/2}, \tag{1.11}$$

which rotate the Bloch vector by an angle of ϑ around the x, y, and z axis, respectively. The one-qubit phasegate, in the variations (0) and (1), changes the relative phase of the $|0\rangle$ and $|1\rangle$ eigenstate. Usually, there is no distinction made between Ph_0 and Ph_1, as both are equivalent up to a global phase:

$$e^{-i\phi}\,\mathrm{Ph}_1(\phi) = \mathrm{Ph}_0(-\phi) \tag{1.12}$$

$\mathrm{Ph}_1(\pi/2)$ is sometimes referred to simply as *Phase-*, or $\hat{S}$-gate, whereas $\mathrm{Ph}_1(\pi/4)$ is often called the $\pi/8$-gate. This somewhat confusing convention stems from the fact that we can write

$$\mathrm{Ph}_1(\pi/4) = \begin{pmatrix} 1 & 0 \\ 0 & e^{i\pi/4} \end{pmatrix} = e^{i\pi/8} \begin{pmatrix} e^{-i\pi/8} & 0 \\ 0 & e^{\pi/8} \end{pmatrix}. \tag{1.13}$$

We can also define operators acting on two-qubit states. One possibility is to extend one-qubit operators to the two-qubit Hilbert space and combine them, e.g.

$$\begin{aligned}
(\hat{X} \otimes \mathbb{1}_{1q})(\mathbb{1}_{1q} \otimes \hat{X}) &= \begin{pmatrix} 0 & 0 & 1 & 0 \\ 0 & 0 & 0 & 1 \\ 1 & 0 & 0 & 0 \\ 0 & 1 & 0 & 0 \end{pmatrix} \begin{pmatrix} 0 & 1 & 0 & 0 \\ 1 & 0 & 0 & 0 \\ 0 & 0 & 0 & 1 \\ 0 & 0 & 1 & 0 \end{pmatrix} \\
&= \begin{pmatrix} 0 & 0 & 0 & 1 \\ 0 & 0 & 1 & 0 \\ 0 & 1 & 0 & 0 \\ 1 & 0 & 0 & 0 \end{pmatrix}
\end{aligned} \tag{1.14}$$

However, there are also *true* two-qubit that cannot be decomposed like in the above example. This is in analogy to separable versus entangled two-qubit states. Incidentally, only true two-qubit gates that are not just a combination of single-qubit operations can create entangled states from a non-entangled input. A selection of true two-qubit gates is shown in the lower part of Table 1.1.

The CNOT gate performs a NOT, i.e. a Pauli-X gate, on the second input qubit,[1] but only to the extent that the first input qubit is $|1\rangle$. If the first input qubit is $|0\rangle$, it does not do anything. The SWAP gate switches the two input qubits. Finally, there is the Controlled Phasegate in the (11) and (00) variation. Similar to the CNOT, which performs an $\hat{X}$ on the second (the *target*) qubit if

---

[1] assuming separability

the first (the *control*) qubit is $|1\rangle$, CPHASE$_{11}(\phi)$ performs a single-qubit Ph$_1(\phi)$ on the target qubit if the control qubit is $|1\rangle$. CPHASE$_{00}$ performs a Ph$_0(\phi)$ on the target qubit if the control qubit is $|0\rangle$.

It is very common to draw a series of gates in diagram form, as a *quantum circuit*. In such a quantum circuit, n horizontal lines are drawn from left to right to represent n input and output qubits. The operators are added as the symbols given in the middle column of Table 1.1. The two-qubit controlled operations usually indicate the control qubit with a filled or blank circle (filled if the controlled operation should be active when the control qubit is $|1\rangle$, blank when it should be active if the control qubit is $|0\rangle$), connected to the controlled operation on the target line.

1.3 Controlled Phasegates

The controlled phasegate CPHASE$_{00}$ is at the focus of this thesis. Note that while the two variations CPHASE$_{00}$ and CPHASE$_{11}$ are closely related, they are not equivalent up to a global phase as the one-qubit phasegates in Table 1.1 are.

Both controlled phasegates for $\phi = \pi$ can be combined with one-qubit operations to generate a CNOT. This equivalence is shown in Figure 1.2.

$$(\mathbb{1} \otimes \hat{H}) \begin{pmatrix} 1 & 0 & 0 & 0 \\ 0 & 1 & 0 & 0 \\ 0 & 0 & 1 & 0 \\ 0 & 0 & 0 & -1 \end{pmatrix} (\mathbb{1} \otimes \hat{H}) = \begin{pmatrix} 1 & 0 & 0 & 0 \\ 0 & 1 & 0 & 0 \\ 0 & 0 & 0 & 1 \\ 0 & 0 & 1 & 0 \end{pmatrix}$$

$$= \; (\mathbb{1} \otimes \hat{H})\left((\hat{X} \otimes \mathbb{1})(\mathbb{1} \otimes \hat{X})\right) \begin{pmatrix} -1 & 0 & 0 & 0 \\ 0 & 1 & 0 & 0 \\ 0 & 0 & 1 & 0 \\ 0 & 0 & 0 & 1 \end{pmatrix} \left((\hat{X} \otimes \mathbb{1})(\mathbb{1} \otimes \hat{X})\right)(\mathbb{1} \otimes \hat{H})$$

Figure 1.2: Equivalence of CNOT and controlled-π-phasegate

As a replacement for the CNOT, the controlled-π-phasegate has some benefits. One is that it only affects one of the basis states, as opposed to two for the

CNOT. This suggests that depending on the physical implementation of the qubit, it might be easier to implement a phasegate: For $CPHASE_{00}(\phi)$, we can leave $|01\rangle$, $|10\rangle$ and $|11\rangle$ untouched, and only transform

$$|00\rangle \longrightarrow e^{i\phi} |00\rangle .$$

In comparison, for the CNOT, we would have to transform

$$|10\rangle \longrightarrow |11\rangle$$
$$|11\rangle \longrightarrow |10\rangle .$$

Secondly, a phasegate with a general phase ϕ can be more versatile than a CNOT. For example, it can be directly employed in the implementation of a quantum Fourier transform (see Nielsen and Chuang [1, Chapter 5]). Also, the phasegate has the nice property of being accumulative: we can get $CPHASE(\phi)$ by applying $CPHASE(\phi/n)$ in series n times.

In most of the literature, the controlled phasegate is discussed in the form $CPHASE_{11}$. However, in the implementation scheme that we will discuss in the next chapter, we will only allow manipulation of the $|00\rangle$ eigenstate, not of $|11\rangle$. Hence, we will focus only on the $CPHASE_{00}$ form of the phasegate. As is shown in Figure 1.2, the two forms can be transformed into each other with four one-qubit Hadamard gates.

1.4   Universal Gates

In classical computation, it is well-known that any algorithm can be implemented using just logical NAND functions.[2] In the same way, there is great interest in having a toolbox of qubit operators that when combined can perform any computation. Such a set of operators is called *universal*. It can be shown (see Nielsen and Chuang [1]) that the combination of all one-qubit gates with the two-qubit CNOT is universal. This is quite intuitive: The one-qubit operators can manipulate the individual qubits in any imaginable way, whereas the CNOT serves as a *conditional*, combining the information from different qubits.

In addition to the one-qubit plus CNOT set, it can also be shown that CNOT combined with the one-qubit Hadamard, $CPHASE_1(\pi/2)$, and $\pi/8$-gate are approximately universal, that is any quantum circuit can be approximated to arbitrary precision using just these gates.

As we have seen, the CNOT gate is equivalent to the controlled-phasegate combined with Hadamard and possibly Pauli-X gates. Therefore, we also have a universal set of quantum operators that includes the controlled phasegate as the only two-qubit gate.

In most physical implementations of quantum computing, single-qubit operations are relatively easy to perform, and two-qubit operations are hard. If we manage to successfully implement a CNOT, or controlled phasegate, we have demonstrated that the system can be used for universal quantum computation. This is our motivation for attempting the implementation of a controlled phasegate in a system where the qubits are encoded in the electronic

---

[2]NAND(a,b) is false if a, b, or both are true; and true if a and b are both false.

states of a Calcium atom, as discussed in detail in Chapter 2. Quantum gates can be implemented in the system by applying laser pulses that transfer population between the different levels. The focus of this thesis is to find a laser pulse that implements a controlled phasegate, using numerical simulation of the system and Optimal Control Theory. Chapter 3 will discuss the numerical tools. Chapter 4 will discuss the details of the optimization schemes that are used to solve the problem, before the results will be presented in Chapter 5. Finally, a summary and outlook will be given in Chapter 6.

Chapter 2

Quantum Computation with Calcium Atoms

The discussion of qubits and quantum gates in the previous chapter has been purely abstract, detached from any physical system. A qubit was simply a quantum mechanical two-level system. In reality, we are presented with something much more complicated: We have a large number of neutral atoms, each one with external and internal degrees of freedom. The external degrees of freedom consist of the motion in the three dimensions of space for each individual atom. The internal degrees of freedom are the full electronic structure including spin-orbit coupling, Zeeman, and hyperfine splitting. It is not immediately obvious how such a system can be an implementation of a quantum computer.

DiVincenzo [2] famously formulated five conditions for the successful implementation of a quantum computer. Quoting the original paper:

1. A scalable physical system with well-characterized qubits

2. The ability to initialize the state of the qubits to a simple fiducial state, such as $|000\ldots\rangle$

3. Long relevant decoherence times, much longer than the gate operation time

4. A "universal" set of quantum gates

5. A qubit-specific measurement capability

In order to understand how to define well-characterized qubits in our system, we have to carefully break it down into its parts. Our goal is to find a qubit encoding in the internal states of each atom. We also have to understand the encoding of a two-qubit state and the physical processes that are relevant in order to perform gate operations. At the end of the chapter, we will return to DiVincenzo's criteria, giving an overview over the full quantum computational system.

2.1   Trapping of Calcium Atoms

As a prerequisite, it is quite evident that we will not be able to do successful quantum computation if the Calcium atoms are just wildly flying around in space at high temperatures. In such a situation, even on a short time scale, there would be no way to reliably interact with an individual atom to perform a single qubit gate, or to control the interaction between two specific atoms for a two-qubit gate. It is therefore necessary to limit and control the motional degrees of freedom by cooling and trapping the atoms.

To do this, we can make use of an optical lattice created by multiple standing laser waves. The laser fields can induce a polarizability in neutral atoms (ac-Stark effect and thereby trap them. With three orthogonally crossed waves, a cubic lattice results.

For our purpose, we start with a Bose-Einstein condensate of our atoms and then gradually turn up the lattice. For a sufficiently high lattice potential, Greiner et al. [3] showed that a phase transition from the superfluid phase to the Mott insulator phase occurs. This transition leaves exactly one trapped atom per lattice site. For a review of optical lattices, see Jessen and Deutsch [4] and more recently Bloch [5]. The number of atoms that can be loaded onto an optical lattice can be very large (10^6 as reported by Hamann et al. [6]).

Looking at a plane in the lattice, we have a two-dimensional trap potential

$$V_{\text{trap}} = V_0 \sin^2\left(k_x x\right) + \sin^2\left(k_y y\right). \tag{2.1}$$

We can effectively control the motional degrees of freedom for each atom by choosing the grid wavelength in the x-direction much larger than in the y-direction, so that the movement becomes one-dimensional in the x-direction. Any movement in y or z is frozen out for ultracold temperatures. Thereby, we have significantly reduced the external degrees of freedom for each atom from three to one. In first order, the one-dimensional lattice can be approximated by a harmonic potential at each lattice site. Looking at two neighboring lattice sites, separated by the trap distance d, we can write

$$V_{\text{trap}}(x) \approx \frac{1}{2}\mu\omega^2\left(x + \frac{d}{2}\right)^2 + \frac{1}{2}\mu\omega^2\left(x - \frac{d}{2}\right)^2 \tag{2.2}$$

In order for the atoms to be well-confined to their local trap potential, we require that the ground state trap eigenfunctions of two neighboring lattice sites have minimal overlap. This places a restriction on the trap frequency ω, in dependency of the grid spacing d.

ω[kHz] / d[nm]	5	10	50	75	100	150	200
100	997.5	990.2	781.1	573.5	372.2	108.2	19.18
150	996.3	985.3	69031	434.3	227.0	35.58	2.657
250	993.8	975.6	539.1	249.1	84.49	3.849	**0.051**
500	987.7	951.8	290.7	62.04	7.139	**0.015**	0
1000	975.6	905.9	84.49	3.849	**0.051**	0	0
2000	951.8	820.6	7.139	**0.015**	0	0	0
4000	905.9	673.4	**0.051**	0	0	0	0
100000	84.49	**0.051**	0	0	0	0	0
400000	**0.051**	0	0	0	0	0	0

Table 2.1: Overlap $\langle \Psi_+ | \Psi_- \rangle$ in parts per thousand for Calcium (reduced mass $\mu = 36423.67$ a.u.) In each column, the first entry $< 0.1‰$ is highlighted.

We can calculate the overlap between the left $(+)$ and right $(-)$ ground state wave functions as

$$
\begin{aligned}
\langle \Psi_+ | \Psi_- \rangle &= \left(\frac{m\omega}{\pi\hbar} \right)^{\frac{1}{2}} \int_{-\infty}^{+\infty} \exp\left\{ -\frac{m\omega}{2\hbar} \left[\left(x - \frac{d}{2} \right)^2 \left(x + \frac{d}{2} \right)^2 \right] \right\} \mathrm{d}x \\
&= \left(\frac{m\omega}{\pi\hbar} \right)^{\frac{1}{2}} \int_{-\infty}^{+\infty} \exp\left\{ -\frac{m\omega}{2\hbar} \left[2x^2 + \frac{d^2}{2} \right] \right\} \mathrm{d}x \\
&= e^{-\frac{m\omega d^2}{4\hbar}} \left(\frac{m\omega}{\pi\hbar} \right)^{\frac{1}{2}} \int_{-\infty}^{+\infty} \exp\left\{ -\frac{m\omega}{\hbar} x^2 \right\} \mathrm{d}x \\
&= e^{-\frac{\mu\omega d^2}{2\hbar}}.
\end{aligned}
\tag{2.3}
$$

The overlap for Calcium and a selection of trap parameters ω and d is shown in Table 2.1.

As we will see in the subsequent chapters, the effectiveness of two-qubit operations depends crucially on the lattice distance d, which should be as small as possible, to the limit that the corresponding trap frequency from Table 2.1 is feasible. Under realistic circumstances, feasible trap intensities are in the range 200-330 kHz (cf. Koch et al. [7] and references therein)

Traditionally, the lattice spacing is restricted to about half the laser wavelength, which would mean about 300 nm for a traditional He-Ne-Laser or 120 nm at the absolute minimum for a Ar-UV-laser. To achieve smaller grid-spacing, we can use subwavelength lattices, in which the $\lambda/2$ potentials are sub-divided into several potential wells with the help of multiple additional lasers (discussed specifically in this context by Yi et al. [8]).

Having confined the Calcium atoms to a fixed lattice, we now turn to the internal degrees of freedom in order to find an encoding for the qubit states, before returning to external degrees of freedom for the description of two qubits.

2.2 Internal Degrees of Freedom and Description of a Single Qubit

Our goal is to encode the qubit states $|0\rangle$ and $|1\rangle$ completely in the internal degrees of freedom of a single Calcium atom. There is no coupling between the internal and external degrees of freedom for an isolated qubit. Furthermore, we want to manipulate the qubit using a laser pulse. A selection of the term scheme for Calcium is shown in Figure 2.1.
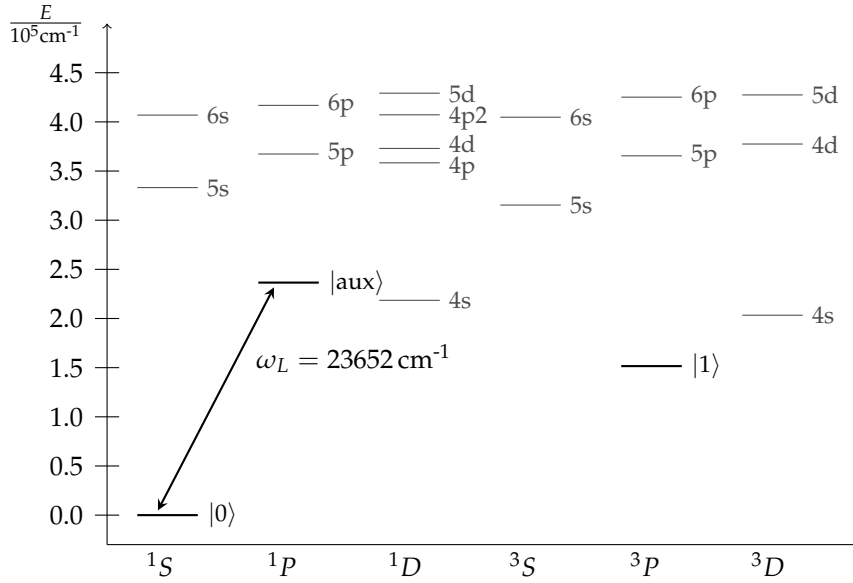
Figure 2.1: Selection of Calcium level scheme, showing the qubit encoding. The energy level information is from the NIST Atomic Spectra Database at `http://physics.nist.gov/PhysRefData/ASD/`

We now choose the following encoding: The $^1S_0$ ground shall represent $|0\rangle$, and the $^3P_1$ state with an energy of 15210 cm^{-1} shall represent $|1\rangle$.

Note that the direct electric dipole transition between $|0\rangle$ and $|1\rangle$ is not allowed (singlet to triplet): The $|1\rangle$ state is metastable with a lifetime on the order of 0.5 ms (Pasternack et al. [9]). This is a sufficient decoherence time for a qubit encoding compared to the time scales of the quantum gates that we strive for, which should be below the nanosecond scale.

In order to manipulate the $|0\rangle$ state independently from $|1\rangle$, which will help in the construction of a controlled phasegate, we also include the $^1P_1$ state as an auxiliary $|\text{aux}\rangle$ in the description of the single qubit. This $|\text{aux}\rangle$ state is at an energy of 23652 cm^{-1} relative to the ground state, and is reachable via an allowed electric dipole transition. We add a laser tuned to $|0\rangle \rightarrow |\text{aux}\rangle$, as shown in Figure 2.1. This laser allows us to do gate manipulations on the $|0\rangle$ state with the fast transition to the $|\text{aux}\rangle$ state. As long as the spectral width of our laser pulse around ω_L stays within reasonable limits, we will not populate any states outside of $|0\rangle$, $|1\rangle$, and $|\text{aux}\rangle$. We assume that the laser is not strong

enough to excite higher order transitions. For large time scales (discussed by Pasternack et al. [9]), the transition between the ground state and the 4s $^1D_2$ state, may become a source of loss scales.

We do not have to include other internal degrees of freedom: both the $|0\rangle$ and the $|\text{aux}\rangle$ states are singlet, which means they have no Zeeman splitting. Also, we use the ^{40}Ca isotope of Calcium, which has a nuclear spin of zero and therefore no hyperfine splitting.

With these arguments, we can conclude that we only have to include the three levels $|0\rangle$, $|1\rangle$, and $|\text{aux}\rangle$ in a description of the relevant internal degrees of freedom for a single qubit.

To fit the definition of the qubit as a two-level system ($|0\rangle$, $|1\rangle$), we require that the $|\text{aux}\rangle$ state is not populated before or after, but only during a gate operation.

The field-free Hamiltonian for the single-qubit description is therefore

$$\hat{H}_{1q}^{(0)} = \begin{pmatrix} E_0 & 0 & 0 \\ 0 & E_1 & 0 \\ 0 & 0 & E_{\text{aux}} \end{pmatrix} \tag{2.4}$$

Adding the laser tuned to the transition between $|0\rangle$ and $|\text{aux}\rangle$, this becomes

$$\hat{H}_{1q} = \begin{pmatrix} E_0 & 0 & \mu\epsilon(t) \\ 0 & E_1 & 0 \\ \mu\epsilon(t) & 0 & E_{\text{aux}} \end{pmatrix} \tag{2.5}$$

where μ is the dipole coupling between the two levels and $\epsilon(t)$ is the laser field. By modifying $\epsilon(t)$ we can control the dynamics of the single qubits. However, we have no direct control over the $|11\rangle$ state, which will always evolve according to its natural field-free time evolution. This means that with the Hamiltonian given by Equation (2.5) we can only implement a subset of all one-qubit operation. However, we could also add a different laser for direct transitions between $|0\rangle$ and $|1\rangle$, using a magnetic dipole transition. For the purpose of implementing a controlled phasegate, this will not be our focus.

Note that in writing Equation (2.5), we have described the laser classically, implying strong fields, and made use of the dipole approximation to describe the interaction between the laser field and the atom's internal degrees of freedom.

2.3 Description of Two Qubits

Having a full description of a single qubit, we can now return to considering two Calcium atoms in neighboring lattice sites. A description of this two-qubit system has to include the one-qubit Hamiltonian for each of the two atoms, the motional degree of freedom, which as we have seen in Section 2.1 can be reduced to one dimension (x_1 for the first qubit, x_2 for the second), and the interaction between the two atoms.

First we rewrite Equation (2.5) in a slightly more abstract form:

$$\hat{H}_{1q} = \sum_i E_i |i\rangle\langle i| + \sum_{i\neq j} \mu_{ij,\infty} |i\rangle\langle j| , \tag{2.6}$$

where $i, j = 0, 1, \text{aux}$. This one-qubit Hamiltonian is an element of SU(3). Then, we write down the complete two-qubit Hamiltonian separated into a non-interaction and an interaction part:

$$\hat{H}_{2q} = \hat{H}_{2q}^{(0)} + \hat{H}_{2q}^{(1)}, \tag{2.7}$$

with the non-interaction Hamiltonian

$$
\begin{aligned}
\hat{H}_{2q}^{(0)}(x_1, x_2) &= \hat{H}_{1q} \otimes \mathbb{1}_{SU(3)} \otimes \mathbb{1}_{x_1} + \mathbb{1}_{x_2} \otimes \mathbb{1}_{SU(3)} \otimes \hat{H}_{1q} \\
&= \sum_{i,j} |i\rangle\langle i| \otimes |j\rangle\langle j| \otimes \\
&\qquad \otimes \left(\hat{T}_{x_1} + \hat{T}_{x_2} + \hat{V}_{\text{trap}}(x_1) + E_i + \hat{V}_{\text{trap}}(x_2) + E_j \right) + \\
&\quad + \sum_{i \neq j, k} |i\rangle\langle j| \otimes |k\rangle\langle k| \otimes \left(\epsilon(t)\hat{\mu}_{ij,\infty} \right) + \\
&\quad + \sum_{i \neq j, k} |k\rangle\langle k| \otimes |i\rangle\langle j| \otimes \left(\epsilon(t)\hat{\mu}_{ij,\infty} \right)
\end{aligned}
\tag{2.8}
$$

Note that in principle, the trap potential can interact differently with different electronic states, so that instead of $\hat{V}_{\text{trap}}$, we should have written $\hat{V}_{\text{trap}}^{ij}$ (cf. Mandel et al. [10, Methods]). However, using the *magic wavelength* technique (see Lundblad et al. [11] and references therein), we can have identical trap potentials for all electronic states included in our Hamiltonian. Using state-dependent trap potentials (e.g. $V_{\text{trap}} \to -V_{\text{trap}}$ for the excited electronic states) did not change our results significantly.

The interaction Hamiltonian reads

$$
\begin{aligned}
\hat{H}_{2q}^{(1)}(x_1, x_2) &= \sum_{i,j} |i\rangle\langle i| \otimes |j\rangle\langle j| \otimes V_{BO}^{(ij)}(|x_2 - x_1|) + \\
&\quad + \sum_{i \neq j, k} |i\rangle\langle j| \otimes |k\rangle\langle k| \otimes \left(\epsilon(t)\hat{\mu}_{ij}(|x_2 - x_1|) \right) + \\
&\quad + \sum_{i \neq j, k} |k\rangle\langle k| \otimes |i\rangle\langle j| \otimes \left(\epsilon(t)\hat{\mu}_{ij}(|x_2 - x_1|) \right).
\end{aligned}
\tag{2.9}
$$

2.3.1 Qubit-Qubit Interaction

In writing down the interaction Hamiltonian for the description of two qubits, we have postulated an interaction potential $V_{BO}(R)$ and an interaction dipole moment $\mu(R)$. These can be understood as Born-Oppenheimer type potentials (see Appendix A). Note that the interaction depends only on the relative distance between the two qubits.

For our simulations, we used interaction potentials and dipoles derived from ab-initio calculations by Bussery-Honvault et al. [12] combined with spectroscopic data from Allard et al. [13]. The first few potential curves are plotted in Figure 2.2, with the asymptotic energies $E_{ij} = E_i + E_j$.[1] What is important is that all potentials surfaces have a long range behavior $1/R^6$, except

---

[1]A plot of the dipoles can be found in the paper by Koch and Moszynski [14]. In the region that we are interested in, the dipole is nearly constant.
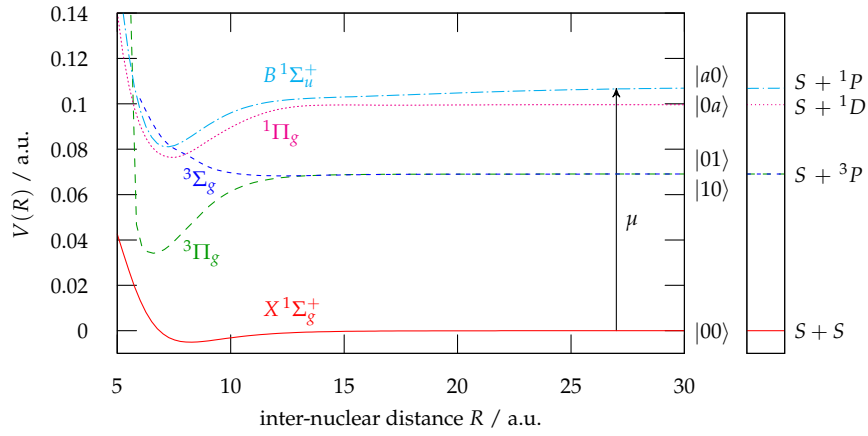
Figure 2.2: Potential surfaces of five lowest R-dependent two-qubit states. The asymptotic values of the potentials correspond to the energies of the logical two-qubit states, shown on the right.

$|0a\rangle = |0\rangle \otimes |\text{aux}\rangle$, $|a0\rangle$, which follow a $1/R^3$ curve (see [12]). At $R = 5$ nm (the region where we will run our optimization) and beyond, the $1/R^6$ potentials are essentially flat, while the $1/R^3$-potentials still has a comparably large gradient.

This means that in the excited $|0a\rangle$, $|a0\rangle$ state, the atoms feel an interaction force that they do not feel in the ground state. It is this physical interaction which we exploit in order to generate a genuine two-qubit interaction leading to entanglement (see Chapter 4).

2.3.2 Harmonic Approximation of the Trap Potential

(a) single particle coordinates

(b) relative coordinate (internuclear distance)
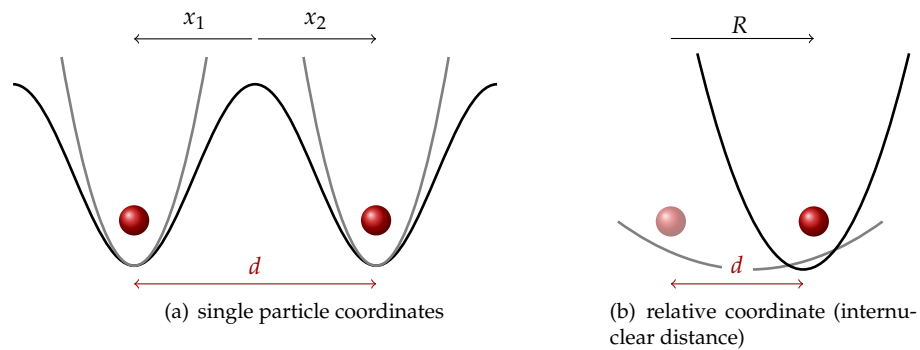
Figure 2.3: Calcium atoms in trap

While the terms in the interaction Hamiltonian of Equation (2.9) are already in relative coordinates $R = x_2 - x_1$, the diagonal elements of the non-interaction Hamiltonian of Equation (2.8) are not.

However, if we go back to the one-dimensional trap potential with two neighboring lattice sites separated by a distance d, as shown in Figure 2.3(a), we can again argue that in a first order approximation, each atom feels a harmonic potential, shown in gray. In this harmonic approximation (and only there), we can also separate the center-of-mass motion from the relative motion.

If x_1 and x_2 denote the single-particle-coordinates of the atom in the left and in the right trap, respectively, then each diagonal element of the Hamiltonian takes the form (neglecting the constant $E_i + E_j$)

$$H_{\text{trap}}(x_1, x_2) = -\frac{\hbar^2}{2m}\left(\nabla_1^2 + \nabla_2^2\right) + $$
$$+ \frac{1}{2}m\omega^2\left(x_1 + \frac{d}{2}\right)^2 + \frac{1}{2}m\omega^2\left(x_2 - \frac{d}{2}\right)^2. \tag{2.10}$$

If we introduce center-of-mass coordinates

$$X = \frac{x_1 + x_2}{2} \tag{2.11}$$
$$M = 2m \tag{2.12}$$

and relative coordinates

$$R = x_2 - x_1 \tag{2.13}$$
$$\mu = m/2, \tag{2.14}$$

we can rewrite the Hamiltonian (see Appendix B.

$$\hat{H}_{\text{trap}} = -\frac{\hbar^2}{2M}\nabla_X^2 + \frac{1}{2}M\omega^2 X^2 - \frac{\hbar^2}{2\mu}\nabla_R^2 + \frac{1}{2}\mu\omega^2(R-d)^2 \tag{2.15}$$

Since the Hamiltonian separates into center-of-mass and relative motion, the wave function can be written as a product $\Psi(x_1, x_2) = \Psi(R)\chi(X)$. We integrate out the center-of-mass motion which leaves us with a Schrödinger equation for the relative motion in the trap:

$$\left(-\frac{\hbar}{2\mu}\nabla^2 + \frac{1}{2}\mu\omega^2(R-d)^2\right)\Psi(R) = E\Psi(R). \tag{2.16}$$

The situation is depicted in Figure 2.3(b). Note that the left Calcium atom now defines the point of origin, while the relative position of the right atom defines the value of the potential. Both atoms are still contained in another harmonic potential via their center of mass, which we have integrated out.

2.3.3 Summary of Two-Qubit Description

Combining the somewhat abstract description of the Hamiltonian at the beginning of Section 2.3 with the discussion of the previous two subsections, we can write down the Hamiltonian for two qubits in a simpler form, using the internuclear distance R (or *vibrational* degree of freedom) as the spatial coordinate. The center-of-mass motion is integrated out. We will also discuss a suitable encoding for the logical (electronic) two-qubit states.

Hamiltonian

The two-qubit Hamiltonian has 9×9 elements, for the nine possible combinations of two single-qubit states. The diagonal elements are

$$H_{i,i} = \hat{T} + \hat{V}_{\text{trap}}(R) + \hat{V}_{BO}^{(i)}(R) + E_i \tag{2.17}$$

The off-diagonal dipole couplings are

$$H_{i,j} = \epsilon(t)\mu_{ijl}(R) \tag{2.18}$$

to the extent that $\mu_{ij} \neq 0$. Together,

$$\hat{H} = \sum_i H_{i,i} \, |i\rangle\langle i| + \sum_{i \neq j} H_{i,j} \, |i\rangle\langle j| \,. \tag{2.19}$$

In all three of these equations, the indexes i, j run over the values 00, 0a, 01, 10, 1a, 11, a0, aa, a1. The letter a is two-qubit shorthand for aux, for example the index 1a indicates the matrix element $|1\rangle\langle 1| \otimes |\text{aux}\rangle\langle\text{aux}|$

If we group the terms $\hat{V}_{BO}^i + E_i$ together, they describe a Born-Oppenheimer surface with the asymptotic value E_i, which is exactly what is shown in Figure 2.2. With this understanding, we label the R-dependent interaction surfaces as $|00\rangle$, $|10\rangle$, etc. according to which electronic two-qubit state they are associated with.

Wave Function

The wave functions of the Hamiltonian given by Equation (2.19) can be decomposed into the surfaces $|00\rangle \ldots |11\rangle$, but also has a motional degree of freedom R. This means that for any surface, there is still an infinite number of possible states; i.e. the vibrational degree of freedom mixes completely with the electronic degree of freedom. To keep the two degrees of freedom separate, we have to encode the two-qubit state in a *specific R-dependent wave function*. For example, we can define the R-dependent $|00\rangle$ qubit eigenstate as

$$|00(R)\rangle = \Psi_{00}^{(0)}(R) \otimes |00\rangle \tag{2.20}$$

where $\Psi_{00}^{(0)}$ is the first eigenstate of Equation (2.17) with an eigenvalue greater then E_0^0, i.e. the first eigenstate that is only bound by the trap potential, akin to the trap ground state.[2] This choice is motivated by the fact the that atoms in the optical lattice automatically go into the trap ground state during the transition to the MOT phase.

This definition of R-dependent two-qubit ground states has an important consequence. Since we will express all gate operations purely on the logical two-qubit states, we must require that we can decouple the motional and the electronic degree of freedom completely before and after each gate operation. For example, we may start with the state $|00(R)\rangle$, which we can reduce to the

---

[2]If $\hat{V}_{BO}$ were constant, $\Psi_{00}^{(0)}$ would be exactly the trap ground state.

logical two-qubit state by integrating out the motional degree of freedom like this:

$$\left\langle \Psi_{00}^{(0)} | 00(R) \right\rangle = \left\langle \Psi_{00}^{(0)} | \Psi_{00}^{(0)} \right\rangle |00\rangle = |00\rangle \tag{2.21}$$

When a laser pulse designed to perform a gate operation is applied to the system, the initial state transforms as

$$|00(R)\rangle \longrightarrow |00(R)\rangle' = \left(\sum_k \alpha'_k \Psi_{00}^k(R) \right) \otimes \left(\sum_{(ij)} \alpha'_{ij} |ij\rangle \right) \tag{2.22}$$

The transformed state again consists of a motional part, written as an expansion into the surface eigenstates $\Psi_{00}^k(R)$, and an internal part, also written as an expansion into the logical eigenstates $|00\rangle$, $|01\rangle$, $|10\rangle$, $|11\rangle$. Only if

$$\left\langle \Psi_{00}^{(0)} | \sum_k \alpha'_k \Psi_{00}^k(R) \right\rangle = 1 \quad \Leftrightarrow \quad \alpha'_k = \delta_{k0}, \tag{2.23}$$

it makes sense to understand the process as a logical gate $|00\rangle \longrightarrow |00\rangle'$. In other words, the system must be in the same vibrational state before and after the gate operation.

$$\Psi_{00}^{(0)}(R) \otimes |00\rangle \overset{!}{\longrightarrow} \Psi_{00}^{(0)}(R) \otimes |00\rangle' \tag{2.24}$$

Failing this requirement is a source of decoherence. We call the left hand side of Equation (2.23) the *vibrational purity*.

Note that it is important that after the gate operation we end up in the *same* eigenstate: if this was not the case, we could not be able to repeat a gate twice with the same effect.

2.4 Asymptotic Description of Two Qubits

In the asymptotic case, where the interaction between the qubits disappears, the two-qubit Hamiltonian can be written simply as the combination of two identical one-qubit Hamiltonians:

$$\hat{H}_{2q} = \hat{H}_{1q} \otimes \mathbb{1} + \mathbb{1} \otimes \hat{H}_{1q}$$

$$= \begin{pmatrix} E_{00} & 0 & \mu\epsilon & & \cdots & & \mu\epsilon & 0 & 0 \\ 0 & E_{01} & 0 & & & & 0 & \mu\epsilon & 0 \\ \mu\epsilon & 0 & E_{0a} & & & & 0 & 0 & \mu\epsilon \\ & & & E_{10} & 0 & \mu\epsilon & & & \\ \vdots & & & 0 & E_{11} & 0 & & \vdots & \\ & & & \mu\epsilon & 0 & E_{1a} & & & \\ \mu\epsilon & 0 & 0 & & & & E_{a0} & 0 & \mu\epsilon \\ 0 & \mu\epsilon & 0 & & & & 0 & E_{a1} & 0 \\ 0 & 0 & \mu\epsilon & & \cdots & & \mu\epsilon & 0 & E_{aa} \end{pmatrix}, \tag{2.25}$$

$|0\rangle \otimes |0\rangle$ becomes $|00\rangle$ with the energy $E_{00} = E_0 + E_0$, and analogously for the other states, which are shown in Figure 2.4 along with their respective energy. There is no R-dependency of the states. This asymptotic case should make the structure of Equation (2.19) yet clearer.

$47304.608\ \text{cm}^{-1}$ ——— $|aa\rangle$

$38862.367\ \text{cm}^{-1}$ ——— $|1a\rangle, |a1\rangle$

$30420.126\ \text{cm}^{-1}$ ——— $|11\rangle$

$23652.304\ \text{cm}^{-1}$ ——— $|0a\rangle, |a0\rangle$ $\omega_L = 23652\ \text{cm}^{-1}$

$15210.063\ \text{cm}^{-1}$ ——— $|01\rangle, |10\rangle$

——— $|00\rangle$
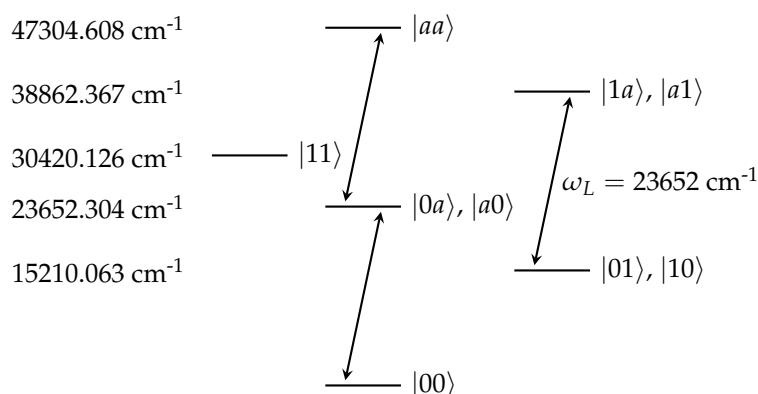
Figure 2.4: Level Scheme of asymptotic two-qubit system, drawn to scale. The energy level information is from the NIST Atomic Spectra Database at `http://physics.nist.gov/PhysRefData/ASD/`

2.5 Quantum Information Processing with Calcium

We will now return to DiVincenzo's five criteria, briefly discussing each. Most of this discussion is valid for any quantum computing model involving neutral atoms in optical lattices.

2.5.1 Scalability

There are several aspects to extending the concepts we have discussed in the previous sections to a large scale. We need a controllable system with suitable parameters of a large number of qubits where we can locally apply one- and two-qubit operations. We need to be able to address local sites. Finally, we need to be able to combine gate results from different sites via the transport of qubits (or qubit information).

We briefly mentioned the use of subwavelength lattices to reach small trap distances. The additional laser fields necessary for this can also supply us with the tools both for addressing and transport, in the form of state-dependent superlattices. These methods are laid out in detail by Yi et al. [8], Daley et al. [15], and Gorshkov et al. [16]. For example, we could use a gradient field to select specific sites and lift the atoms state-dependently to a transport superlattice. By manipulating the individual lattices dynamically, we can implement complex quantum informational procedures. Especially, a dynamic grid is necessary to perform one-qubit operations on neighboring atoms: In order to have *no* interaction in the $|0a\rangle$ state, we need to dynamically move the two atoms apart from each other to the asymptotic case by temporarily expanding the lattice.

A specific addressing problem in the context of our two-qubit gates is that in order to perform a local two-qubit gate we need to operate on two qubits in neighboring lattice sites. One way to guarantee that the model presented in the previous sections holds true is to eliminate every third atom from the lattice, so that there are isolated pairs of two qubits. We might attempt to do such a thing

with the single-site addressability features of the superlattices. Alternatively, we might use the patterned loading techniques proposed by Peil et al. [17] during the initialization phase. If we managed to initialize a lattice with every third atom missing, we could greatly relax the addressability requirement, and instead operate with massive quantum parallelism.

2.5.2 Initialization

The initialization process is extremely easy. As we already discussed, the MOT process guarantees that there is exactly one atom per lattice site. Furthermore, each atom will be in the trap ground state. The ultra-cold environment guarantees very pure quantum states.

The electronic states can in general be freely manipulated, even though in our description of a single qubit, direct electric dipole transitions between $|0\rangle$ and $|1\rangle$ are not allowed. As explained, we could still use a direct magnetic dipole transition to pump between the two levels.

2.5.3 Decoherence

The great benefit of using *neutral* atoms as qubit carriers is that they interact weakly with the environment, providing low decoherence. Of course, this feature also makes the implementation of two-qubit gates more difficult, as neutral atoms also interact weakly with each other.

We have already discussed one source of decoherence: the lifetime of the metastable $|1\rangle$ state which is on the order of about 0.5 ms. Furthermore, we also have to take into account spontaneous emission from the $|aux\rangle$ state. The lifetime for the transition can be found in the NIST Atomic Spectra Database `http://physics.nist.gov/PhysRefData/ASD/` as 4.59 ns. While this is a considerably shorter time span, it only limits our gate time: between gates, the $|aux\rangle$ state should not be populated

There are further sources of decoherence which depend on the accuracy of an experimental implementation: photon scattering in the trap, fluctuations in the laser fields, and imperfections in pulse timing.

We will show in Chapter 5.3 that the entanglement between the internal and the motional degree of freedom (cf. Equation (2.23)) can be a significant problem under certain conditions.

Lastly, we must be careful that the pulses implementing the quantum gates do not lead out of the qubit-subspace, for example due to multiple-photon-excitations.

2.5.4 Universal Quantum Gates

The realization of a universal set of quantum gates will be the focus of the remainder of this thesis. Implementing one-qubit operations is possible with simple optical pumping. We will see an example for the implementation of a one-qubit gate in Section 4.1.1. As we have seen in Section 1.4, if we are able to do arbitrary one-qubit operations, we need CNOT as the only two-qubit gate to

guarantee universality. Since the controlled phasegate that is the focus of this thesis is equivalent to the CNOT, in the sense that we can build a CNOT out of single-qubit operations together with one or more controlled phasegates, we have a universal set of quantum gates to the extend that the implementation of the phasegate is successful.

2.5.5 Measurement

The last step in the implementation of a full quantum computer is the read-out of states. One option is to do a destructive measurement at the end of all gate operations. For this we switch off the trap and perform time-of-flight measurements. See Chapter 4 of the diploma thesis by Ohliger [18] and references therein for a detailed discussion of time-of-flight measurements in optical traps.

A non-destructive alternative is the Quantum Jump technique developed by Nagourney et al. [19], Bergquist et al. [20], and Sauter et al. [21], as well as by Finn et al. [22] for neutral atoms. The technique is based on monitoring the fluorescence of a strong transition which will cease if the atom is in the metastable state that we are measuring for.

Chapter 3

Numerical Tools

3.1 Numerical Representation of the System

3.1.1 Discretization

In the previous description of the Calcium system, The relative spatial coordinate R appearing in the Hamiltonian and in the wave functions has been a continuous variable between 0 and ∞. The same applies to time. However, since we simulate the system in a computer, we have to approximate the continuous description of the system by a discrete and finite one. Specifically, we need to map the Hamiltonian and the wave function as

$$\hat{H} \longrightarrow \hat{H}_N; \qquad \Psi \longrightarrow \Psi_N, \tag{3.1}$$

where N is the dimension of the finite Hilbert space of the numerical description.

Tannor [23, Chapter 11] gives an extensive overview of the various methods and considerations for doing such a numerical description.

In essence, we have to restrict ourself to a subspace of the full Hilbert space by choosing a projector $\hat{P}_N$ so that

$$\hat{H}_N = \hat{P}_N \hat{H} \hat{P}_N; \qquad \Psi_N = \hat{P}_N \Psi, \tag{3.2}$$

based on a set of basis functions ϕ_n:

$$\hat{P}_N = \sum_{n=1}^{N} |\phi_n\rangle\langle\phi_n| \tag{3.3}$$

These basis functions may be a regular set of orthogonal functions (truncated to the first N), in which case we talk about a *spectral* basis; or they may be a set of functions localized on a set of grid points,[1] in which case we talk about a *pseudospectral* basis. In principle, we can find corresponding spectral and

---

[1]Each basis function is localized at a grid point in the sense that it has an amplitude of zero at each grid point except the one it is localized at. It may however have an amplitude greater than zero *between* grid points. Furthermore, it is a δ-type function that becomes a sharp δ peak for $N \to \infty$

pseudospectral bases that are related by a unitary transformation and therefore equivalent. Quite generally, we want the basis functions to exhibit *collocation*, that is the numerical wave function Ψ_N should coincide exactly with the true wave function Ψ at a set of grid points (or *collocation points*) R_i:

$$\Psi_N(R_i) = \hat{P}_N \Psi(R_i) = \Psi(R_i) \tag{3.4}$$

$$\Psi(R) \approx \hat{P}_N \Psi(R) \tag{3.5}$$

Based on collocation, we can rewrite $\hat{P}_N$ in a pseudospectral basis in which the values of $\Psi(R_i)$ serve as expansion coefficients (cf. Section 3.1.2). That is, collocation opens up the possibility of representing the system intuitively by simple *sampling*: taking the actual system values, but at regular grid points. While this might be the first thing that comes to mind in treating any system numerically, it has to be based on a proper footing. For a good collocation scheme, we demand a *discrete* orthogonality relation

$$\sum_{j=1}^{N} \phi_k^*(R_j)\phi_l(R_j)\Delta_j = \delta_{kl}; \qquad m,n = 1 \ldots N \tag{3.6}$$

for the basis functions at the grid points, as opposed to a continuous one for traditional non-collocation spectral bases. Δ_j is a weight depending on the specific choice of the ϕ_n.

3.1.2   The Fourier Grid

For the purpose of our simulation, we choose the Fourier method (Kosloff [24]), in which the spectral basis is a set of band-limited[2] plane waves.

$$\Psi_N(R) = \frac{1}{\sqrt{N}} \sum_{n=1}^{N} a_n e^{ik_n R}; \qquad k = \kappa_n \Delta k \tag{3.7}$$

The index κ_n has the values

$$\kappa_n = \kappa_{\min} \ldots \kappa_{\max} = \begin{cases} -\left\lfloor \frac{N}{2} \right\rfloor \ldots \left\lfloor \frac{N}{2} \right\rfloor & \text{if } N \text{ odd} \\ -\frac{N}{2}+1 \ldots \frac{N}{2} & \text{if } N \text{ even.} \end{cases} \tag{3.8}$$

The Fourier basis works with an equidistant spatial grid

$$R_j = (j-1)\Delta R; \qquad j = 1 \ldots N, \quad \Delta R = \frac{L}{N} \tag{3.9}$$

with the grid size $L = R_{\max}$. The spectral expansion coefficients are

$$a_n = \frac{1}{\sqrt{N}} \sum_{j=1}^{N} \Psi(R_j) e^{-i\kappa_n \Delta k R_j}. \tag{3.10}$$

---

[2]*Band-limited* means that that there is a lower and and upper bound for the frequencies appearing.

We do not in fact *store* the wave function as an array of the *spectral* coefficients a_n. Instead, based on the associated *pseudospectral* basis[3] (see Tannor [23, Section 11.6.3])

$$\theta_j = \sum_{n=1}^{N} \frac{1}{\sqrt{L}} e^{i2\pi\kappa_n R/L} \frac{1}{\sqrt{N}} e^{i2\pi\kappa_n R_j/L} \tag{3.11}$$

for which the $\Psi(R_j)$ are the expansion coefficients, we store it as an array of the *sampled* values $\Psi(R_j)$.

The Fourier method gets its name from the fact that the spectral expansion coefficients are defined by Equation (3.10), which is the discrete Fourier transform of $\Psi(R)$. Defining the grid in coordinate space as in Equation (3.9) implicitly gives us a grid in momentum space as well. The grid spacing Δk for the momentum grid comes out of the orthogonality requirement in Equation (3.6) with $\Delta_j = 1$:

$$\sum_{j=1}^{N} \phi_k^*(R_j)\phi_l(R_j) = \frac{1}{N} \sum_{j=1}^{N} \exp\left[i\,\Delta k(\kappa_k - \kappa_l)R_j\right]$$
$$= \frac{1}{N} \sum_{j=1}^{N} \exp\left[i\frac{\Delta k\,L}{N}(\kappa_k - \kappa_l)(j-1)\right] \tag{3.12}$$

For $k = l$, this is clearly one. Otherwise, we can identify Equation (3.12) as a partial sum of the geometric series:

$$\sum_{\nu=0}^{\tilde{N}} \gamma^\nu = \begin{cases} \tilde{N}+1 & \text{if } \gamma = 1, \\ \frac{1-\gamma^{\tilde{N}+1}}{1-\gamma} & \text{if } \gamma \neq 1, \end{cases} \tag{3.13}$$

with

$$\gamma = \exp\left[i\frac{\Delta k\,L}{N}(\kappa_k - \kappa_l)\right]. \tag{3.14}$$

In our case, $\nu = j - 1$ and $\tilde{N} = N - 1$ Since $\gamma \neq 1$ for $k \neq l$, the orthogonality is fulfilled if

$$1 - \gamma^{\tilde{N}+1} = 0 \quad \Leftrightarrow \quad \gamma^{\tilde{N}+1} = 1. \tag{3.15}$$

We see that

$$\gamma^N = \exp\left[i\,\Delta k\,L(\kappa_k - \kappa_l)\right] = 1 \tag{3.16}$$

is fulfilled for

$$\Delta k = \frac{2\pi}{L}. \tag{3.17}$$

In summary, the Fourier method provides us with a grid in coordinate space and an associated grid in momentum space, illustrated in Figure 3.1.

$$R_j = (j-1)\Delta R \qquad j = 1\ldots N \qquad \Delta R = \frac{L}{N} \tag{3.18}$$

$$k_\kappa = \kappa\Delta k \qquad \kappa = \kappa_{\min}\ldots\kappa_{\max} \qquad \Delta k = \frac{2\pi}{L} \tag{3.19}$$

---

[3]Whereas the spectral basis has its coefficients in *k*-space, the pseudo-spectral basis has its coefficients in coordinate space.
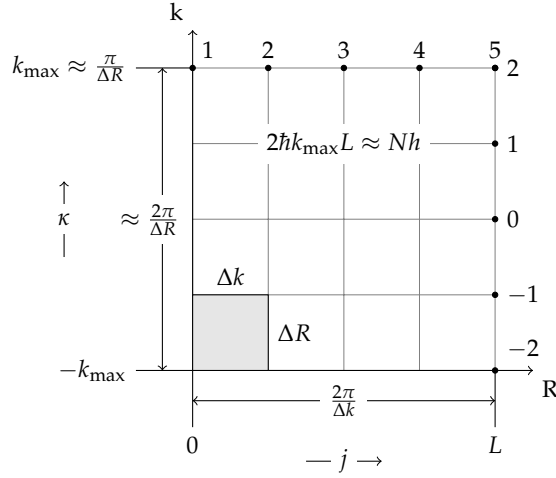
Figure 3.1: Phase space Fourier grid, drawn for the example of $N = 5$. For odd N, we find $k_{\max} = -k_{\min} = \delta_N \frac{\pi}{\Delta R}$, $\delta_N = \left(\left\lfloor \frac{N}{2} \right\rfloor \frac{2}{N} \right) = \frac{N-1}{N}$, and $\delta_N Nh$ for the total phase space volume (x-range $\times$ p-range, $p = \hbar k$) which for large N goes to the limit of Nh, or h per grid point. For even N, we find $k_{\max} = -k_{\min} + \Delta k = \frac{\pi}{\Delta R}$, and $Nh + 2\pi$ for the total phase space volume. Again, this goes to the limit of h per grid point for large N.

$$\kappa_{\min} = \begin{cases} -\left\lfloor \frac{N}{2} \right\rfloor & \text{for } N \text{ odd} \\ -\frac{N}{2} + 1 & \text{for } N \text{ even} \end{cases} \qquad \kappa_{\max} = \begin{cases} \left\lfloor \frac{N}{2} \right\rfloor & \text{for } N \text{ odd} \\ \frac{N}{2} & \text{for } N \text{ even} \end{cases} \tag{3.20}$$

$$k_{\min} = \begin{cases} -\frac{N-1}{N} \frac{\pi}{\Delta R} & \text{for } N \text{ odd} \\ -\frac{\pi}{\Delta R} + \Delta k & \text{for } N \text{ even} \end{cases} \qquad k_{\max} = \begin{cases} \frac{N-1}{N} \frac{\pi}{\Delta R} & \text{for } N \text{ odd} \\ \frac{\pi}{\Delta R} & \text{for } N \text{ even} \end{cases} \tag{3.21}$$

The Fourier grid is optimal in terms of the Shannon Sampling Theorem [25, Theorem 1], which guarantees that if all wavenumbers not in the range $k_{\min} \ldots k_{\max}$ can be neglected, the spatial grid of N points with a sampling width of ΔR describes the system with arbitrary precision.

3.1.3   Application of the Hamiltonian

In the Fourier method, it is now rather easy to apply the Hamiltonian $\hat{H}_N$ to a given wave function Ψ_N. We consider the actual Hamiltonian in the Calcium two-qubit system, given by Equation (2.19), at a fixed time t_0. The wave function in the system can be written as (cf. Equation (2.20))

$$|\Psi\rangle = \sum_i \alpha_i \, |i(R)\rangle \tag{3.22}$$

with i running over all nine $00, 0a, \ldots 11$.

The application of the Hamiltonian in Equation (2.19) to the wave function in Equation (3.22) becomes

$$\hat{H} \, |\Psi\rangle = \sum_i \alpha_i \hat{H}_i \, |i(R)\rangle + \sum_{i,j} \alpha_j \hat{H}_{i,j} \, |i(R)\rangle \tag{3.23}$$

Each term in the above sum only affects one of the surface-wave-functions $|i(R)\rangle$, so we can treat the surfaces as completely independent with the trivial exception of the dipole couplings between two surfaces: here, the population-amplitude a_{kl} of the coupled surface enters as a simple scaling parameter. We apply the full Hamiltonian to our full wave function by going through each surface, and applying a surface-Hamiltonian of

$$\hat{H}_{\text{sf}}^{(i)} = \hat{T} + \hat{V}_{\text{trap}}^{(i)}(R) + \hat{V}_{BO}^{(i)}(R) + E_i + \alpha_{kl}\epsilon_{t_0}\hat{\mu}_{i,j}(R), \quad (3.24)$$

written out with the assumption that each surface is only coupled to at most one other surface.

Now, if we think only on one surface and look at Equation (3.24), we notice that all operators except the kinetic $\hat{T}$ are diagonal in coordinate space: We represent the potentials and dipoles numerically simply by sampling them at the grid points R_j of our Fourier grid. For each operator

$$\hat{V} \in \{\hat{V}_{\text{trap}}^i(R),\ \hat{V}_{BO}^i(R),\ \alpha_{kl}\epsilon_{t_0}\hat{\mu}_{i,j}(R)\},$$

its action on the wave function at each point R_k is given by

$$\left|\tilde{i}(R_k)\right\rangle = V(R_k)\left|i(R_k)\right\rangle. \quad (3.25)$$

Unlike the potentials and dipoles, the kinetic operator is *not* diagonal in coordinate space. It is however diagonal in momentum space. Therefore, we can apply a Fourier Transform ($\hat{F}$) to the wave function in coordinate space, then the kinetic operator, and lastly transform the wave function back to coordinate space:

$$\hat{T}\left|ij(R)\right\rangle = \hat{F}^{-1}\hat{T}_\kappa\hat{F}\left|ij(R)\right\rangle \quad (3.26)$$

with

$$\hat{T}_\kappa = \text{diag}_\kappa\left(\frac{\hbar^2(\kappa\Delta k)^2}{2\mu}\right) \quad (3.27)$$

An alternative approach would be to write out the kinetic operator explicitly in coordinate space with help of the pseudospectral basis. However, the *dynamic method* we just described is both straightforward from a numeric perspective, and highly efficient due to the existence of Fast-Fourier-Transform (FFT) implementations scaling as $N\log N$ with the number grid points.

3.2 Initialization and Eigensystem

As explained in Section 2.3.3, we initialize the system to the (quasi-) trap ground state on the $|00\rangle$ surface. To this end, we can diagonalize the surface-Hamiltonian in Equation (3.24) for $\epsilon \equiv 0$ using standard routines for matrix diagonalization.

Note that while the physical system has infinitely many vibrational eigenstates, we can only recover the first N if we represent our system on a grid with N grid points. From another point of view, higher eigenstates have an increasingly higher number of oscillations, which translates to the need for a larger band-limitation $k_{\text{max}}\ldots k_{\text{min}}$ on the Fourier grid. We need to set N large

enough so that all eigenfunctions that we expect to be populated during our simulation are accurately represented.

It makes sense to retain the full set of the field-free eigenfunctions and eigenvalues as a surface-projector, so that at any time we can analyze the state of the system by checking which vibrational eigenstates eigenstates are populated. Especially, at the end of a gate-pulse, only the initial eigenstate should be populated.

The diagonalization of the field-free surface-Hamiltonian only needs to be done once at the very beginning.

3.3 Mapped Grid Representation

3.3.1 The Efficient Use of Phase Space Volume

Remembering the surface-potentials in the Calcium system (see Figure 2.2), we see that there are two very distinct regions. In the very short range < 20 a.u. $\approx$ 1 nm, the potential surface forms a distinct well, while in the asymptotic range > 200 a.u. ≈ 10 nm it is nearly flat. Considering that we are potentially interested in distances of up to 6000 a.u., there is a vast imbalance between the two parts.

Unfortunately, it is the dynamic short-range part of the potential that defines the need for a phase space volume on the Fourier grid. In a semi-classical description, the momentum of the Calcium atom with energy E is (see Nest and Meyer [26])

$$p(R) = \sqrt{2\mu(E - V(R))} \tag{3.28}$$

which is largest at the minimum of the potential surface. Figure 3.2 shows an example for a Morse potential. Using Equation (3.21), we see that we need a local sampling width of at least

$$\Delta R(R) = \frac{\hbar\pi}{p(R)}. \tag{3.29}$$

In fact, sampling theory teaches us that we need a grid twice as dense to avoid aliasing effects (*Nyquist frequency*). Furthermore, if we loosen the semi-classical picture of Equation (3.28) and account for quantum mechanical momentum uncertainty, we also need a smaller ΔR. We add a factor β ranging between 0 and 1 to express this.

$$\Delta R(R) = \beta \frac{\hbar\pi}{p(R)} \tag{3.30}$$

Since the Fourier method implies a constant sampling width, we need to take the minimum value of $\Delta R(R)$ as the global sampling width, spanning a phase space on the large asymptotic part of the grid that is completely unused. This is indicated in Figure 3.2(b). In comparison, Figure 3.1 illustrates the Fourier method being designed to describe a rectangular phase space. The solution to this problem, as described by Fattal et al. [27], is to use *mapping* of the spatial grid.

(a) Morse Potential   (b) Used Phase Space
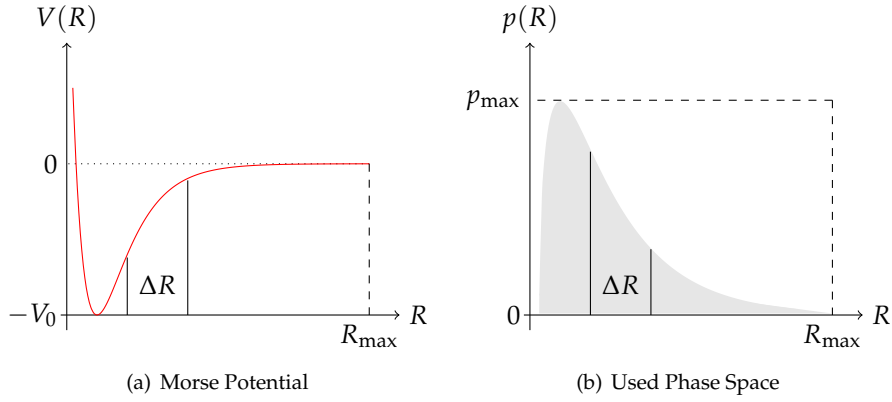
Figure 3.2: Morse potential of the shape $V(R) = V_0(1 - e^{\alpha(R_0-R)})^2 - V_0$ and associated momentum $p(R) = \sqrt{2\mu(E - V(R))}$ for $E = 0$. The shaded area under the momentum curve indicates the used phase space volume. The Fourier grid accurately represents the entire rectangle $p_{max} \times R_{max}$ (and mirrored down) indicated by dashed lines in (b).

The idea of the mapping procedure is to change the grid spacing, so that there is a large number of grid points in a region with large momentum, and fewer grid points on the long tail of the potential with small momentum. The grid spacing ΔR becomes dynamic. We map the points on the R axis to a new grid

$$R(x_j) \longrightarrow x_j = x_0 \dots (x_0 + N\Delta x), \tag{3.31}$$

so that if we plot the momentum space for x, it fills the rectangular shape in Figure 3.2(b) as much as possible. Note that the mapped coordinates x_j are equidistant again, so the conditions of the Fourier grid are still matched.

There are two methods for calculating the mapping of Equation (3.31), which we will discuss in the following.

3.3.2 Differential Mapping

The differential mapping method described by Kokoouline et al. [28] is a straightforward application of Equation (3.30). We start at the left side of our grid with $R_0 = R_{min}$, and calculate a local

$$\Delta R(R) = \beta \frac{\pi}{\sqrt{2\mu(E_{max} - V(R))}} \tag{3.32}$$

in atomic units ($\hbar = 1$). This ΔR is then added to R_{min} to calculate R_1, and we repeat until we have constructed N grid points:

$$R_i = R_{i-1} + \Delta R(R_{i-1}) \quad \text{for } i = 2 \dots N \tag{3.33}$$

E_{max} together with β are tweakable parameters of the mapping procedure. As explained in the previous section β controls the general density of grid points,

whereas E_{max} is (originally) the total energy we want to be able to describe. It has an effect on the density of points on the asymptotic tail, preventing ΔR to go over a certain limit in this region. In combination, the two parameters can compensate for each other, so that they lose some of their original meaning. In practice we can regard them as numerical knobs for affecting the mapped grid.

In most cases, we define a maximum grid extension R_{max} for our system. With the differential mapping, we start at R_{min} and then make N steps with a calculated ΔR based on the shape of the potential. This means that in the end we might end up at a value for R_N that is smaller or larger than R_{max}. We have to set E_{max} and β by trial and error so that $R_N \approx R_{max}$.

In most cases, and also in the Calcium system, there is more than one potential surface. However, we need to define a single spatial grid that allows to describe the dynamics on any of these surfaces accurately. To this end, we define an *envelope potential* can be any lower bound to all the potential surfaces of the system (shifted to the same asymptote). In addition, we make the envelope potential monotonic, which avoids problems with the sampling at the inner turning point of the Born-Oppenheimer-potentials. The envelope potential takes the place of V in Equation (3.32).

The mapped working grid is simply $x = 1 \ldots N$, with an equidistant grid spacing $\Delta x = 1$. All expressions are implicitly expressed on this working grid, e.g. the wave function Ψ as $\Psi(x_i) = \Psi(R_i)$.

A consequence of doing such a coordinate transformation is that we have to include the Jacobian

$$J(x) = \frac{\mathrm{d}R}{\mathrm{d}x} \tag{3.34}$$

in any integrals over the spatial coordinate such as

$$\int_{-\infty}^{+\infty} \Psi^*(R)\Psi(R)\,\mathrm{d}R = \int_{-\infty}^{+\infty} \Psi^*(x)\Psi(x)J(x)\,\mathrm{d}x \tag{3.35}$$

to account for the distortion between the original and mapped space.[4] If we compensate for this by renormalizing the wavefunction as

$$\tilde{\Psi}(x) = \frac{\Psi(x)}{\sqrt{J(x)}} \tag{3.36}$$

we also have to modify the kinetic operator. Kokoouline et al. [28] calculate that the kinetic operator has to be rewritten as

$$\tilde{T} = -\frac{1}{4\mu}\left(\frac{1}{J(x)^2}\nabla_x^2 + \nabla_x^2\frac{1}{J(x)^2} - \frac{7}{2}\frac{J'(x)^2}{J(x)^4} + \frac{J''(x)}{J(x)^3}\right) \tag{3.37}$$

As Willner et al. [29] show, the numeric differentiation of in Equation (3.34) and the further differentiation of $J(x)$ in Equation (3.37) together with other not fully understood factors can lead to numerical instabilities, which result in

---

[4]The Jacobian is calculated by numerical differentiation, which gives this mapping method its name.

additional and unphysical eigenvalues and eigenfunctions in the diagonalization of the Hamiltonian, so-called *ghosts*. The appearance of such ghosts can be reduced if instead of the Fourier basis the closely related sine/cosine basis is used. Instead of FFT, Fast-Cosine-Transform algorithm have to be used to apply the kinetic operator. These are still comparable in efficiency to the FFT. In our runs, the propagation in the sine/cosine basis tended to be about 30-40 percent slower. Nonetheless, whenever differential mapping was used, it went together with the sine/cosine basis.

3.3.3   Integral Mapping

An alternative mapping procedure that is more robust against ghost states while still using the more efficient Fourier basis is the *integral mapping* proposed by Kallush and Kosloff [30]. This method turns Equation (3.32) on its head and constructs the mapped grid in the following way: We start at the right side of the grid with R_{max}. To find the next smaller mapped grid point, we numerically solve the equation

$$\beta = \sqrt{\frac{2\mu}{\pi^2}} \int_{R_j}^{R_{j+1}} \sqrt{E_{max} - V(R)}\, dR \tag{3.38}$$

for R_j with $R_{j+1} = R_{max}$ initially (cf. Equation (3.32)). This is repeated until we reach R_{min}. Since the FFT routines that we use are most efficient if the number of grid points N only has the prime factors 2, 3, and 5, we continue the mapping until we have a suitable N. The integral mapping method results in an equidistant working grid with $\Delta x = \beta$, as opposed to $\Delta x = 1$ for the differential mapping.

Note that whereas in the differential mapping we had to tweak β and E_{max} to make sure the mapped grid reaches the desired R_{max}, this is no problem for the integral mapping method. Instead, we now have to make sure that the number of grid points N is close to our desired value. However, if we have found values of β and E_{max} that work for one mapping method, they will generally also work for the other.

With the integral mapping method, the Jacobian does not have to be derived from numerical differentiation, but instead can be calculated as

$$J(x) = \frac{\pi}{\sqrt{2\mu\, |E_{max} - V(x)|}}. \tag{3.39}$$

This is the major reason the integral mapping proves to be more robust against ghosts than the differential mapping. They can however still occur if β is too small.

Setting the mapping parameters E_{max} and β is done by changing them systematically through trial and error until

1. no ghost states appear in the spectrum.

2. R_{max} and N are close to the desired values.

Table 3.1 shows a comparison between differential and integral mapping.

	differential mapping	integral mapping
recommended basis	sine/cosine	exponential (Fourier)
grid size N	$2^n - 1$	$2^n \cdot 3^m \cdot 5^l$ (after mapping)
$J(x)$	$\frac{dR}{dx}$	$\pi / \sqrt{2\mu \left| E_{max} - V(x) \right|}$
Δx	1	β

Table 3.1: Comparison of differential and integral mapping. The grid size is due to the specific implementation of the sine/cosine and Fourier transform, respectively.

3.4 Time Propagation

Once we have a numerical description of the wave function and the Hamiltonian, the second step is the ability to simulate the time evolution of the system. Specifically, we need a numerical method to calculate

$$\left| \Psi(R,t) \right\rangle = \hat{U} \left| \Psi(R, t = 0) \right\rangle; \qquad \hat{U}(t, t + \Delta t) = e^{-\frac{i}{\hbar} \hat{H}(t) \Delta t}. \tag{3.40}$$

There are two widely-used approaches to handle this for a general time-dependent Hamiltonian.

The first approach is to separate $\hat{H}$ into $\hat{H} = \hat{T} + \hat{V}$ over small time intervals Δt and to approximate

$$e^{-\frac{i}{\hbar}(\hat{T} + \hat{V})\Delta t} \approx e^{-\frac{i}{\hbar} \hat{T} \Delta t} e^{-\frac{i}{\hbar} \hat{V} \Delta t}, \tag{3.41}$$

which leads to a method known as the *split propagator* (Feit et al. [31]). The split propagator can only be used for very small time intervals Δt.

The second approach is to approximate $\hat{U}$ with a polynomial expansion

$$e^{-\frac{i}{\hbar} \hat{H} \Delta t} \approx \sum_{n=0}^{N} a_n P_n(-i\hat{H}/\hbar), \tag{3.42}$$

where the P_n are a set of polynomials in $\hat{H}$. There are several possible choices of polynomials. We will use Chebychev polynomials, as proposed by Tal-Ezer and Kosloff [32] (see Kosloff [24] for a review).

3.4.1 The Chebychev Propagator

The Chebychev polynomials are defined as

$$P_n(x) = \cos\left(n \arccos(x)\right); \quad -1 \leq x \leq 1. \tag{3.43}$$

We use them in their complex form

$$\Phi_n(z) = i^n P_n(-iz); \quad -i \leq z \leq i. \tag{3.44}$$

Since the polynomials are only defined in the range $-i$ to i, we have to renormalize the Hamiltonian so that its eigenvalues are in the range -1 to 1. To this

end, we define

$$\hat{H}_{\text{norm}} \equiv \frac{\hat{H} - (\Delta E/2 + V_{\text{min}})\,\mathbb{1}}{\Delta E/2} = \frac{2}{\Delta E}\left(\hat{H} - \hat{C}\right). \tag{3.45}$$

ΔE is the *spectral radius* of the Hamiltonian, that is the range of eigenvalues. $\hat{C}$ is an abbreviation for $(\Delta E/2 + V_{\text{min}})\,\mathbb{1}$. With this definition, the time evolution operator can be approximated (see Kosloff [24]) as

$$e^{-\frac{i}{\hbar}\hat{H}\Delta t} \approx e^{-i(\alpha + V_{min}t)}\sum_{n=0}^{N} a_n(\alpha)\Phi_n(-i\hat{H}_{\text{norm}}); \qquad \alpha \equiv \frac{\Delta E}{2}\Delta t. \tag{3.46}$$

It turns out that the expansion coefficients are given by the Bessel functions J_n:

$$a_n(\alpha) = (2 - \delta_{n0})J_n(\alpha) \tag{3.47}$$

The actual Chebychev polynomials are calculated with the recursion relation

$$\phi_0(-i\hat{H}_{\text{norm}}) = \mathbb{1} \tag{3.48}$$

$$\phi_1(-i\hat{H}_{\text{norm}}) = -i\hat{H}_{\text{norm}} \tag{3.49}$$

$$\phi_n(-i\hat{H}_{\text{norm}}) = -2i\hat{H}_{\text{norm}}\,\phi_{n-1}(-i\hat{H}_{\text{norm}}) + \phi_{n-2}(-i\hat{H}_{\text{norm}}) \tag{3.50}$$

We see that in each recursion step, we have to apply the Hamiltonian once, which we do as explained in Section 3.1.3.

Note that the Hamiltonian is assumed to be constant over the time propagation. If this is fulfilled, t can be arbitrarily large. In our system, however, the Hamiltonian includes the time-dependent laser pulse $\epsilon(t)$. We therefore propagate in small time steps ($t \rightarrow \Delta t$), which should be considerably shorter than the frequency of the laser pulse, such that we can approximate the laser to be constant within one time step. To the extent that this is not fulfilled, we accumulate an error that appears as a loss of the norm of Ψ.

The asymptotic form of the Bessel functions for $n \rightarrow \infty$ is (see Abramowitz and Stegun [33, p. 365])

$$J_n(\alpha) \sim \frac{1}{\sqrt{2\pi\alpha}}\left(\frac{e\alpha}{2n}\right)^n. \tag{3.51}$$

We see that for $n \gtrsim \alpha$ the Bessel functions and therefore the Chebychev coefficients decrease exponentially. We can choose N such that the contribution from higher Chebychev coefficients is smaller than the machine precision. From experience, a safe initial choice for the number of Chebychev coefficients is

$$\tilde{N} = 4\lfloor \alpha \rfloor \geq 40. \tag{3.52}$$

We always start out with a minimum of 40 coefficients, accounting for the fact that Equation (3.51) breaks down for small N. However, if we can reach the desired precision with less coefficients than 40, we will throw out the rest.

To summarize the propagation with the Chebychev method, we go through the following algorithm in order to propagate a wave function from time 0 to T:

1. Calculate (or estimate) the spectral radius ΔE and $\alpha = \frac{\Delta E}{2} \Delta t$.

2. Calculate the array of $\tilde{n} \geq 40$ chebychev coefficients as $a_0 = j_0(\alpha)$, $a_n = 2J_n(\alpha)$. Store the first $N < \tilde{N}$ coefficients so that a_N is smaller than the machine precision.

3. For each time step, until T is reached:

   (a) Accumulate the wave function $\Psi(t + \Delta t)$ by iterating over $\sum_{n=0}^{N} a_n \phi_n$ using the recursion relation of Equation (3.50). For each term in the sum, the normalized Hamiltonian of Equation (3.45) has to be applied once.

   (b) Calculate and apply the renormalization phase $\exp\left[-i\alpha - iV_{\min}\Delta t\right]$ to $\Psi(t + \Delta t)$

3.4.2   Estimation of the Spectral Radius

The proper way to calculate the spectral radius would be to diagonalize the full Hamiltonian for the minimum and maximum pulse values. This however is numerically too expensive to do in every propagation. Instead, we estimate the spectral radius from the range of energies occurring in the Hamiltonian:

$$
\begin{aligned}
\Delta E = \frac{p_{\max}^2}{2\mu} + \\
+ \left(\max_{R,i}(V_{\text{trap}}^{(i)}(R) + V_{BO}^{(i)}(R)) - \min_{R,i}(V_{\text{trap}}^{(i)}(R) + V_{BO}^{(i)}(R)) \right) + \\
+ \left(\max_{R,ij} \mu_{ij}(R) \max_t |\epsilon(t)| - \min_{R,ij} \mu_{ij}(R) \min_t |\epsilon(t)| \right)
\end{aligned}
\tag{3.53}
$$

Another possibly more accurate possibility is the use of imaginary time propagation proposed by Kosloff and Tal-Ezer [34] to find just the lowest and highest eigenvalue of the Hamiltonian.

3.4.3   Time Grid, Pulse, and Spectral Resolution

In the description of the Chebychev propagator we have introduced a time grid going from 0 to T in steps of Δt. Any state is positioned at a point on this time grid, and moves forwards or backwards[5] through Chebychev propagation. The Hamiltonian used for a propagation step is time dependent through the laser pulse $\epsilon(t)$. However, we define the pulse to be *between* time grid points. The first point of the pulse is a $t_{\text{start}} = \Delta t/2$, the last one at $t_{\text{stop}} = T - \Delta t/2$. In other words, a time grid for the states with N_t time points is associated with a pulse time grid that is shifted by $\Delta t/2$ and has $N_p = N_t - 1$ points. To propagate a state $\Psi(t = t_i)$ to $\Psi(t + \Delta t = t_{i+1})$ (or in the opposite direction), we always use the value of the pulse between the two time points, at $t + \Delta t/2$. This makes forward and backward propagation unambiguous.

---

[5]Backward propagation can be done by simply setting $\Delta t \longrightarrow -\Delta t$

A central characteristic of the laser pulse is its spectrum, which we can calculate through a Fourier transform. This works in complete analogy to the spatial Fourier grid in Section 3.1.2.

With $\Delta T_p \equiv t_{\text{stop}} - t_{\text{start}}$, the frequency grid resulting from the Fourier transform can express frequencies between $-\omega_{\text{max}}$ and $+\omega_{\text{max}}$, with

$$\omega_{\text{max}} = \frac{\pi}{\Delta t} = \frac{(N_p - 1)\pi}{\Delta T_p} \tag{3.54}$$

in atomic units (cf. Equation (3.21)). The frequency spacing, or *spectral resolution*, is

$$\Delta\omega = \frac{2\omega_{\text{max}}}{N_p - 1} = \frac{2\pi}{\Delta T_p} \tag{3.55}$$

(cf. Equation (3.19)). Note the relationship of Equation (3.55) to the quantum-mechanical time-energy uncertainty relation.

3.5 Optimal Control Theory

So far we have developed a numerical (i.e. discrete) description of the system, and discussed Chebychev propagation for simulating the time evolution for a given laser pulse. We still need a tool allowing us to tackle our goal of implementing a two-qubit controlled phasegate, that is to find a laser pulse so that the time evolution operator $\hat{U}(\epsilon(\tilde{t}))$ (cf. Equation (3.40)) applied to any initial state $|\Psi_i\rangle = |\Psi(t=0)\rangle$ results in the state $\hat{O}|\Psi_i\rangle$ at time T, where $\hat{O}$ is the CPHASE transformation. The time index $\tilde{t}$ refers to the pulse time grid, which is shifted by $\Delta t/2$ compared to the time grid for the states (see previous section).

Note that for a given pulse we can already test whether it implements the controlled phasegate: we simply use it to propagate the four basis states $|00(R)\rangle$, $|01(R)\rangle$, $|10(R)\rangle$, and $|11(R)\rangle$. If all of them end up in the correct final state, we know that due to the basis property *any* initial state will be transformed correctly.

For finding a pulse that implements the controlled phasegate, we employ Optimal Control Theory (OCT), specifically the Krotov method, originally developed for the control of quantum systems by Sklarz and Tannor [35] and refined by Palao et al. [36].

We define a *process* $w = w[t, \{\Psi_k\}, \epsilon(\tilde{t})]$ consisting of a set of N states Ψ_k ($k = 1 \ldots N$) and a laser pulse $\epsilon(\tilde{t})$. Each state evolves over time with a time evolution operator $\hat{U}_k(\epsilon(\tilde{t}))$, using the *same* pulse $\epsilon(\tilde{t})$, starting from an initial state Ψ_{ki}.

On our search for a phasegate-pulse, we start out with an arbitrary process

$$w^{(0)} = \left[t, \{\Psi_k^{(0)}\}, \epsilon^{(0)}(\tilde{t})\right], \tag{3.56}$$

where $\epsilon^{(0)}(\tilde{t})$ is the *guess pulse*. We then optimize that initial process with the goal of reaching the *target*

$$w^{(\text{opt})} = \left[t, \{\Psi_k^{(\text{opt})}\}, \epsilon^{(\text{opt})}(\tilde{t})\right], \tag{3.57}$$

The optimization is done by minimizing a target functional

$$J(w) = -F\left(\{\Psi_k(T)\}\right) + \int_0^T g(\epsilon)\,\mathrm{d}t \qquad (3.58)$$

The first term defines a *fidelity* that only depends on the process states at the final time T, that is the result of propagating the initial states Ψ_{ki} with the pulse $\epsilon(\tilde{t})$. The second term takes into account all the intermediate time steps.

In our case, the N states included in the process could be the four two-qubit basis states, for example. As an expression for the fidelity we use

$$F \propto \Re\left[\mathrm{tr}\left(\hat{O}^\dagger \hat{U}\right)\right], \qquad (3.59)$$

which written out in the basis states $|n\rangle$, e.g.

$$|n\rangle = |00(R)\rangle, |01(R)\rangle, |10(R)\rangle, |11(R)\rangle \qquad (3.60)$$

and normalized to the range $[0,1]$ becomes

$$F = \frac{1}{N}\Re\sum_{k=1}^N \left\langle n_k \left| \hat{O}^\dagger \hat{U} \right| n_k \right\rangle .. \qquad (3.61)$$

The second constraint in Equation (3.58) is defined with

$$g(\epsilon) = \frac{\alpha}{S(\tilde{t})}\left[\epsilon(\tilde{t}) - \epsilon^{(0)}(\tilde{t})\right]^2 \qquad (3.62)$$

OCT allows to to find an optimized process

$$w^{(1)} = \left[t, \{\Psi_k^{(1)}\}, \epsilon^{(1)}(\tilde{t})\right], \qquad (3.63)$$

starting from the guess process in Equation (3.56) so that $J(w^{(1)}) \leq J(w^{(0)})$. This procedure can be repeated iteratively, with the optimized pulse $\epsilon^{(1)}$ becoming the guess pulse $\epsilon^{(0)}$ in the new iteration. Ultimately, this will converge to $w^{(1)} \to w^{(\mathrm{opt})}$.

The term $\int g(\epsilon)\,\mathrm{d}t$ in J with g defined as in Equation (3.62) limits the intensity change between iterations. The parameter $\alpha > 0$ is an arbitrary scaling parameter. $S(\tilde{t})$ is a shape function, which enforces an envelope over the optimized pulse. We can use this to to enforce a pulse amplitude of zero at $t = 0$ and T and a smooth switch-on and switch-off.

When convergence is reached, the fidelity F becomes one, and $\int g\,\mathrm{d}t$ becomes zero. The minimum value of J is therefore $J_{\mathrm{opt}} = -1$.

In the Krotov formulation of OCT, the optimized process $w^{(1)}$ is derived by introducing an auxiliary functional L whose optimization is equivalent to the optimization of J.

$$L(w) = G(\{\Psi_k(T)\}) - \Phi(t=0, \{\Psi_{ki}\}) - \int_0^T R(t, \{\Psi_k\})\,\mathrm{d}t \qquad (3.64)$$

$$G(\{\Psi_k\}) = F(\{\Psi_k(T)\}) + \Phi(T, \{\Psi_k(T)\} \qquad (3.65)$$

$$R(t, \{\Psi_k\}, \epsilon) = -g(\epsilon) + \frac{\mathrm{d}\Phi}{\mathrm{d}t}(t, \{\Psi_k\}) \qquad (3.66)$$

The central feature is the introduction of the new term $\Phi(t, \{\Psi_k\})$, which we can use as an extra free parameter to aid finding an optimized $\epsilon^{(1)}$. The idea (paraphrasing Palao et al. [36]) is the following:

- Φ is constructed so that the functional $L(w^{(0)})$ is a maximum with respect to any possible $\{\Psi_k\}$. This gives complete freedom to change to field ϵ.

- A new field $\epsilon^{(1)}$ is derived with the condition of maximizing R, decreasing the value of L compared to $w^{(0)}$. The states Ψ_k in $w^{(1)}$ must be kept consistent with the evolution under $\epsilon^{(1)}$.

This recipe does not presuppose a specific expression for F and $g(\epsilon)$ yet. Applied to our choices, one finds after a lengthy calculation [36][6] that the optimized $\epsilon^{(1)}$ has to be calculated as $\epsilon^{(1)}(\tilde{t}) = \epsilon^{(0)}(\tilde{t}) + \Delta\epsilon(\tilde{t})$ with

$$
\begin{aligned}
\Delta\epsilon(\tilde{t}) &= \Delta\epsilon\left(t + \frac{\Delta t}{2}\right) \\
&= \frac{S(\tilde{t})}{\alpha}\Im\left[\sum_{k=1}^{N}\frac{1}{2}\left\langle \Psi_{ik}\left|\hat{O}^{\dagger}\hat{U}^{\dagger}(T \to t, \epsilon^{(0)})\hat{\mu}\hat{U}(0 \to t, \epsilon^{(1)})\right|\Psi_{ik}\right\rangle\right]
\end{aligned} \tag{3.67}
$$

To better understand the structure of Equation (3.67), we define the target state associated with the initial state Ψ_{ik} as

$$
|\Psi_{tk}\rangle \equiv \hat{O}|\Psi_{ik}\rangle. \tag{3.68}
$$

The operator $\hat{U}(T \to t, \epsilon^{(0)})$ represents a backward propagation from T to t with the old pulse. We abbreviate

$$
\left|\Psi_{bw,k}\right\rangle(t) \equiv \hat{U}(T \to t, \epsilon^{(0)})|\Psi_{tk}\rangle. \tag{3.69}
$$

On the right, the operator $\hat{U}(0 \to t, \epsilon^{(1)})$ represents a forward propagation from 0 to t with the new (optimized) pulse. We abbreviate

$$
\left|\Psi_{fw,k}\right\rangle(t) \equiv \hat{U}(T \to t, \epsilon^{(0)})|\Psi_{tk}\rangle. \tag{3.70}
$$

With these abbreviations, we can rewrite Equation (3.67) as

$$
\Delta\epsilon\left(t + \frac{\Delta t}{2}\right) = \frac{S(t + \frac{\Delta t}{2})}{\alpha}\Im\left[\sum_{k=1}^{N}\frac{1}{2}\left\langle \Psi_{bw,k}(t)\left|\hat{\mu}\right|\Psi_{fw,k}(t)\right\rangle\right]. \tag{3.71}
$$

Remember that the wavefunctions $\Psi_{bw,k}$ and $\Psi_{fw,k}$ include multiple surfaces (indexed by i and j, respectively) over which we have to sum in the evaluation of the braket expression:

$$
\left\langle \Psi_{bw,k}(t)\left|\hat{\mu}\right|\Psi_{fw,k}(t)\right\rangle = \sum_{ij}\left\langle \Psi_{bw,k,i}(t)\left|\hat{\mu}_{ij}\right|\Psi_{fw,k,j}(t)\right\rangle \tag{3.72}
$$

With this understanding, Equation (3.67) defines a straightforward algorithm which we use to optimize an initial guess pulse, shown in Figure 3.3.

---

[6]The derivation presented by Palao et al. [36] splits the wave functions and the Hamiltonian into the real and imaginary part. A summary of the Krotov method for complex wave functions $\{\Psi_k\}$, corresponding to the notation we have used, is given by Koch et al. [37].
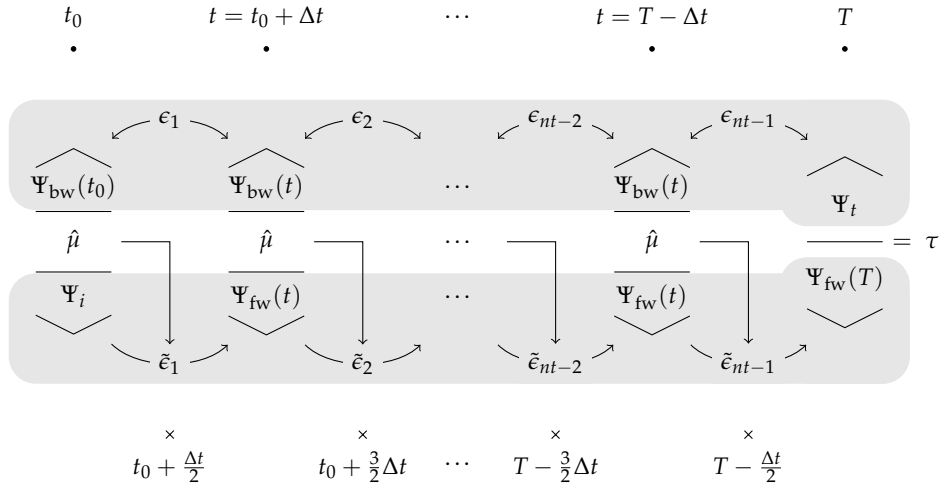
Figure 3.3: OCT Algorithm

- Start with a known initial state $|\Psi_i(t_0 = 0)\rangle$, the target state $|\Psi_t(T)\rangle = \hat{O}|\Psi_i(0)\rangle$, and the initial guess pulse $\epsilon^{(0)}$ containing the values $\epsilon_1 \ldots \epsilon_{nt-1}$. The figure depicts the case where the process w only contains one state ($N = 1$), hence no index k.

- Use the old pulse to propagate $|\Psi_t(T)\rangle$ through the entire time grid, storing all the backwards-propagated states $|\Psi_{bw}(t)\rangle$.

- Calculate the update $\Delta\epsilon(t_0 + \frac{\Delta t}{2})$ with Equation (3.71) and $\left|\Psi_{fw}(t_0)\right\rangle = |\Psi_i\rangle$ and update the first value of the pulse $\epsilon_1 \longrightarrow \tilde{\epsilon}_1$.

- Use $\tilde{\epsilon}_1$ to propagate the initial state $|\Psi_i\rangle$ forward one time step.

- Continue updating the pulse, until the end of the time grid is reached.

At this point, every element of the pulse will have been updated, so that we have moved from $\epsilon^{(0)}$ to $\epsilon^{(1)}$ consisting of the elements $\tilde{\epsilon}_1 \ldots \tilde{\epsilon}_{nt-1}$

We can calculate the complex overlap

$$\tau = \left\langle \Psi_t(T) | \Psi_{fw}(T) \right\rangle \tag{3.73}$$

and from that the new fidelity

$$F = \Re[\tau] \tag{3.74}$$

Note that storing all the backward-propagated wavefunctions may be extremely memory-intensive. If we don't have enough memory to do this, we only keep the the last state $|\Psi_{bw}(t_0)\rangle$. We can recover the other backwards-propagated states as we need them (e.g. the Ψ_{bw} with index $i + 1$) by propagating forward again with the old pulse value *after* we have calculated the updated value $\tilde{\epsilon}_i$ but *before* we overwrite the old value ϵ_i with it.

Chapter 4

Phasegate Optimization Schemes

When trying to find a laser pulse that implements a controlled two-qubit phase gate on the Calcium system from Chapter 2, we will employ optimization with respect to a choice of different *targets*. By *target* we mean an optimal process, as defined by Equation (3.57). Optimizing a target yields a laser pulse realizing the desired transformation for any given input state.

This chapter discusses different possible types of optimization schemes. These schemes differ in the type of Hamiltonian they are based on and in the choice of states that are included in in the target process. We will look at optimizations both of single and two-qubit gates (cf. Section 2.2 and 2.3, respectively). For two-qubit gates, we also have the choice whether to work in the asymptotic case or whether to include the R-dependent interaction.

From the lessons of these three optimization schemes, we will develop tools to judge the effectiveness of our optimization results for the controlled phasegate beyond the fidelity of Equation (3.61).

Once we understand the different types of targets, we will exploit redundancies to formulate two efficient optimization schemes for the CPHASE on Calcium, which will be the basis for the results presented in Chapter 5.

4.1 Optimization Targets

4.1.1 The Single-Qubit Phasegate

Before considering the two-qubit gate, we should first look at a single-qubit operation. One reason is that for universal quantum computing, we need to be able to do arbitrary one-qubit operations alongside a two-qubit CNOT, as we've seen in Section 1.4; the other reason for looking at the one-qubit system first is that from a formal point of view, optimizing a one-qubit gate is just a slightly simpler variation of a two-qubit CPHASE optimization.

As a specific example, we can look at a single-qubit phasegate (cf. Section 1.2):

$$\hat{O} = e^{i\phi_T} \begin{pmatrix} e^{i\phi} & 0 \\ 0 & 1 \end{pmatrix}. \tag{4.1}$$

The Hamiltonian describing the relevant dynamics for a single qubit consists of the three levels $E_0 = 0$, $E_{\text{aux}} = 23652.304$ cm^{-1}, $E_1 = 15210.063$ cm^{-1} (cf. Figure 2.1). The E_0 level is coupled to the E_{aux} level by a laser pulse, the E_1 level simply follows its natural time evolution.

We want perform a phasegate on any state in the logical basis $|0\rangle$, $|1\rangle$:

$$|\Psi\rangle = \alpha_0 |0\rangle + \alpha_1 |1\rangle \quad \xrightarrow{\hat{O}} \quad e^{i(\phi+\phi_T)}\alpha_0 |0\rangle + e^{i\phi_T}\alpha_1 |1\rangle = \hat{O}|\Psi\rangle \tag{4.2}$$

with a possible global phase ϕ_T. For the two basis states, we have

$$|0\rangle \xrightarrow{\hat{O}} e^{i(\phi+\phi_T)} |0\rangle \tag{4.3}$$

$$|1\rangle \xrightarrow{\hat{O}} e^{i\phi_T} |1\rangle \tag{4.4}$$

We attempt to implement the transformation $\hat{O}$ with an optimized pulse that actually performs the time evolution $\hat{U}$:

$$\alpha_0(0) |0\rangle + \alpha_1(0) |1\rangle \quad \xrightarrow{\hat{U}} \quad \alpha_0(T) |0\rangle + \alpha_1(T) |1\rangle \tag{4.5}$$

Only for the optimal pulse we have $\hat{O} \equiv \hat{U}$.

Remember that we use

$$F = \frac{1}{N}\Re\left[\sum_{k=1}^{N}\left\langle n_k \left| \hat{O}^\dagger \hat{U} \right| n_k \right\rangle\right] \tag{4.6}$$

for the fidelity (Equation (3.61)), with $\hat{O}$ being the target transformation and $\hat{U}$ being the actual time evolution realized by our (optimized) pulse. The $|n\rangle$ are the eigenstates of the system, or more generally the set of states to to be optimized simultaneously.

Specifically, in this example:

$$\begin{aligned} F &= \frac{1}{2}\Re\left[\left\langle 0 \left| e^{i(\phi+\phi_T)}\alpha_0(T) \right| 0 \right\rangle + \left\langle 1 \left| e^{i\phi_T}\alpha_1(T) \right| 1 \right\rangle\right] \\ &= \frac{1}{2}\Re\left[e^{-i(\phi+\phi_T)}\alpha_0(T)\right] + \frac{1}{2}\Re\left[e^{-i\phi_T}\alpha_1(T)\right] \end{aligned} \tag{4.7}$$

If we actually try to optimize a π-phasegate for a global phase $\phi_T = 0$, i.e.

$$|0\rangle \longrightarrow -|0\rangle \quad \text{and} \quad |1\rangle \longrightarrow |1\rangle,$$

we get a pulse that drives the dynamics of the system as shown in Figure 4.1.

The optimized pulse only has a fidelity of $F = 0.139201$. However, this is not surprising: Since the $|1\rangle$ state is not coupled to any other level, the state must evolve according to

$$\alpha_1(t) = e^{i\phi_1(t)} = e^{-i\frac{E_1}{\hbar}t}, \tag{4.8}$$

Figure 4.1: Time evolution of the states $|0\rangle$ and $|1\rangle$ under the optimized pulse for a π phasegate with global phase $\phi_0 = 0$. The state at $t = 0$ is indicated by a black dot, the state at $t = T$ by a black square.

independently of the pulse! We can verify that for $T = 1.23\,\mathrm{ps}$, the final phase of the $|1\rangle$ state is indeed $\phi_1 = 0.7566\pi$, which is exactly what can be seen in Figure 4.1.

This means that for a global phase of $\phi_T = 0$, it is not possible to find a pulse implementing the desired transformation. In fact, given that $|1\rangle$ always has the same time evolution, the best possible fidelity is

$$F = \frac{1}{2}\Re[1] + \frac{1}{2}\Re\left[e^{i\phi_T}\right] = \frac{1}{2} - \frac{0.7215528227}{2} = 0.139201, \qquad (4.9)$$

which is exactly what we get.

However, if we optimize with $\phi_T = \phi_1$, i.e.

$$|0\rangle \longrightarrow e^{i(\phi_1 + \pi)}|0\rangle \quad \text{and} \quad |1\rangle \longrightarrow e^{i\phi_1}|1\rangle,$$

we find an optimized pulse that implements the phasegate with a fidelity of nearly 1. The dynamics of that system under the optimized pulse are shown in Figure 4.2

This illustrates that we have to include the global phase originating from the natural time evolution of the $|1\rangle$ state explicitly in our optimization target. This phase depends on the gate time T. Note that physically, any global phase is irrelevant. The necessity to include it in our formulations stems from our choice of the fidelity.

Formally, the optimization of the one-qubit phase gate that we have just discussed is very similar to the optimization of the full two-qubit controlled phasegate. We can see that the necessity of a global phase applies to the two-qubit gate as well. In the two-qubit Hamiltonian, the $|11\rangle$ state is not coupled to any of the other levels, and undergoes the same evolution as the $|1\rangle$ state of
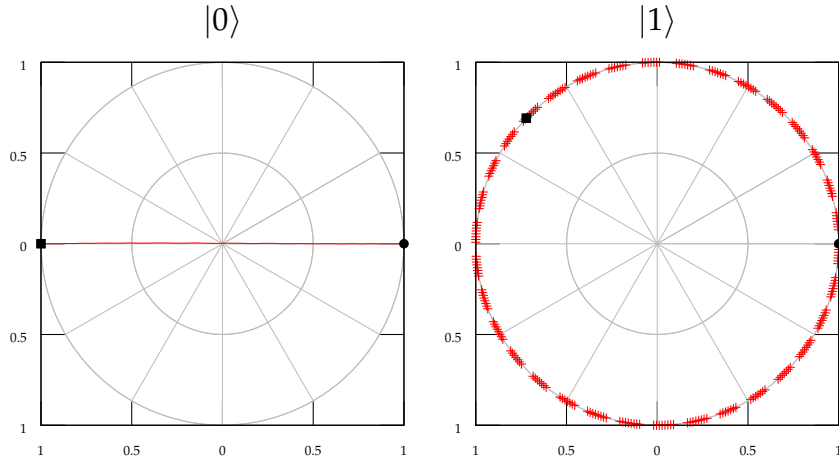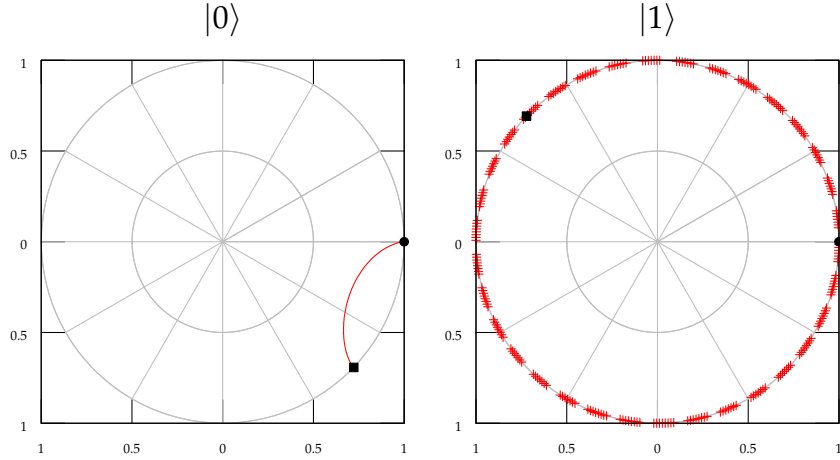
Figure 4.2: Time evolution of the states $|0\rangle$ and $|1\rangle$ under the optimized pulse for a π phasegate with global phase $\phi_0 = 0.7566\pi$. The state at $t = 0$ is indicated by a black dot, the state at $t = T$ by a black square.

the one-qubit system, at twice the speed: $\phi_{11}(T) = 2\phi_1(T)$. We must include $\phi_{11}(T)$ as a global phase in the optimization.

4.1.2 Attempt at a Controlled Phasegate for Non-Interacting Qubits

In the Hamiltonian for non-interacting qubits (cf. Section 2.4), the energy levels and their coupling are as depicted in Figure 2.4.

Since the $|11\rangle$ state is the only one that cannot be controlled by the pulse, its natural time evolution gives us the system's necessary global phase of $\phi_T = \phi_{11}(T) = 1.513\pi$ at $T = 1.23$ ps.

In analogy to the one-qubit gate, we optimize with ϕ_T as a global phase:

$$|00\rangle \xrightarrow{\hat{O}} e^{i(\phi+\phi_T)} |00\rangle \tag{4.10}$$

$$|01\rangle \xrightarrow{\hat{O}} e^{i\phi_T} |01\rangle \tag{4.11}$$

$$|10\rangle \xrightarrow{\hat{O}} e^{i\phi_T} |10\rangle \tag{4.12}$$

$$|11\rangle \xrightarrow{\hat{O}} e^{i\phi_T} |11\rangle \tag{4.13}$$

If we try to optimize a two-qubit π-phasegate, we find that the optimization converges on a fidelity significantly smaller than 1. It turns out we cannot implement a two-qubit controlled phasegate on this non-interacting system consisting just of the tensor product between two identical single Calcium atoms. We need the physical R-dependent interaction between the two qubits to ob-

tain a two-qubit phasegate. The reason for this, as we will see in Section 4.2, is that we need interaction in order to achieve *entanglement*.

4.1.3   The Full Two-Qubit Controlled Phasegate

The non-interacting two-qubit description of Section 2.4 was the asymptotic limiting case of the full two-qubit description of Section 2.3. To optimize the full description, we also have to include the R-dependent interaction. We can extend the states in our target to include an R-dependency easily. To do this we switch to R-dependent basis states like the one defined in Equation (2.20). We then use exactly the same transformation targets as in Equations (4.10)–(4.13), except with $|00(R)\rangle$, $|10(R)\rangle$, $|01(R)\rangle$, $|11(R)\rangle$. Written out explicitly,

$$\Psi_{00}^{(0)}(R) \otimes |00\rangle \xrightarrow{\hat{O}} e^{i(\phi+\phi_T)}\, \Psi_{00}^{(0)}(R) \otimes |00\rangle \tag{4.14}$$

$$\Psi_{01}^{(0)}(R) \otimes |01\rangle \xrightarrow{\hat{O}} e^{i\phi_T}\, \Psi_{01}^{(0)}(R) \otimes |01\rangle \tag{4.15}$$

$$\Psi_{10}^{(0)}(R) \otimes |10\rangle \xrightarrow{\hat{O}} e^{i\phi_T}\, \Psi_{10}^{(0)}(R) \otimes |10\rangle \tag{4.16}$$

$$\Psi_{11}^{(0)}(R) \otimes |11\rangle \xrightarrow{\hat{O}} e^{i\phi_T}\, \Psi_{11}^{(0)}(R) \otimes |11\rangle \tag{4.17}$$

Note again that we require that we can integrate out the motional degree of freedom before and after the gate operation; on each surface, the final state $\Psi_{ij}(R)$ must be identical to the initial eigenstate $\Psi_{ij}^{(0)}(R)$.

In principle, this defines the optimization that we use for the controlled phasegate of the Calcium system for which the results are discussed in Chapter 5. However, the optimization can be made more efficient. We will first develop a deeper understanding of the possibilities of optimizing genuine two-qubit gates based on the idea of Cartan decomposition. Based on this understanding, we will combine the optimization of the single- and two-qubit-Hamiltonian for improved efficiency.

4.2   True Two-Qubit Operations

4.2.1   Decomposition of a Two-Qubit Gate

As we have seen in the model without R-dependency, optimizing for a two-qubit phasegate might result in a transformation that can be entirely decomposed into one-qubit gates. A defining characteristic of a true two-qubit operation is that it can create entanglement.

As shown by Zhang et al. [38], for any two-qubit gate in SU(4), there is a Cartan Decomposition

$$\begin{aligned}
\hat{U}_{2q} &= \hat{U}_1\, \hat{A}_{2q}\, \hat{U}_2 \\
&= \hat{U}_1\, \exp\!\left[\frac{i}{2}\left(c_1\hat{\sigma}_x^1\hat{\sigma}_x^2 + c_2\hat{\sigma}_y^1\hat{\sigma}_y^2 + c_3\hat{\sigma}_z^1\hat{\sigma}_z^2\right)\right]\hat{U}_2
\end{aligned} \tag{4.18}$$

where $\hat{U}_1$ and $\hat{U}_2$ are local (one-qubit) operations and $\hat{A}_{2q}$ is the true two-qubit part of $\hat{U}_{2q}$.

The coefficients c_1, c_2, and c_3 can be determined by solving the equations

$$\Re[G_1] = \cos^2 c_1 \cos^2 c_2 \cos^2 c_3 - \sin^2 c_1 \sin^2 c_2 \sin^2 c_3 \tag{4.19}$$

$$\Im[G_1] = \frac{1}{4} \sin 2c_1 \sin 2c_2 \sin 2c_3 \tag{4.20}$$

$$G_2 = 4\cos^2 c_1 \cos^2 c_2 \cos^2 c_3 - 4\sin^2 c_1 \sin^2 c_2 \sin^2 c_3 -$$
$$- \cos 2c_1 \cos 2c_2 \cos 2c_3 \tag{4.21}$$

where the left hand sides are given by the local invariants

$$G_1 = \frac{\text{tr}^2\left[m(\hat{U}_{2q})\right]}{16 \det \hat{U}_{2q}} \tag{4.22}$$

$$G_2 = \frac{\text{tr}^2\left[m(\hat{U}_{2q})\right] - \text{tr}\left[m^2(\hat{U}_{2q})\right]}{4 \det \hat{U}_{2q}} \tag{4.23}$$

with

$$m(\hat{U}) = (\hat{Q}^\dagger \hat{U} \hat{Q})^{\text{T}} \hat{Q}^\dagger \hat{U} \hat{Q} \tag{4.24}$$

and $\hat{Q}$ being the transformation matrix to the Magic basis

$$\hat{Q} = \frac{1}{\sqrt{2}} \begin{pmatrix} 1 & 0 & 0 & i \\ 0 & i & 1 & 0 \\ 0 & i & -1 & 0 \\ 1 & 0 & 0 & -i \end{pmatrix} \tag{4.25}$$

4.2.2   Entangling Power

We can use the concurrence measure, defined as

$$C(|\Psi\rangle) = \left|\langle\Psi|\hat{\sigma}_y \otimes \hat{\sigma}_y|\Psi^*\rangle\right|, \tag{4.26}$$

to find the degree of entanglement of a two-qubit state.

It is easy to calculate that for an arbitrary product state, we have

$$C\left[(\alpha_0|0\rangle + \alpha_1|1\rangle) \otimes (\beta_0|0\rangle + \beta_1|1\rangle)\right] = 0 \tag{4.27}$$

On the other hand, for a state that we know to be maximally entangled, the result is

$$C\left[\frac{1}{\sqrt{2}}(|00\rangle + |11\rangle)\right] = 1 \tag{4.28}$$

This, however, only gives us the entanglement of a *state*; what we would like is to have some characterization of a *gate*. We can define the entangling power (or concurrence) of a gate as the maximum concurrence of a state resulting from applying the gate to a suitable unentangled state. Unfortunately, we do not know in advance what this maximally entangled output state may be, or which unentangled input state may lead to it.

This problem was addressed by Kraus and Cirac [39]. It can be shown that the two-qubit gate $\hat{A}_{2q}$ is diagonal in the Magic basis:

$$\hat{Q}^\dagger \hat{A}_{2q} \hat{Q} = \text{diag}\left\{ e^{i\lambda_1}, e^{i\lambda_2}, e^{i\lambda_3}, e^{i\lambda_4} \right\}, \quad \text{with} \tag{4.29}$$

$$\lambda_1 = \frac{c_1 - c_2 + c_3}{2} \tag{4.30}$$

$$\lambda_2 = \frac{c_1 + c_2 - c_3}{2} \tag{4.31}$$

$$\lambda_3 = \frac{-c_1 - c_2 - c_3}{2} \tag{4.32}$$

$$\lambda_4 = \frac{-c_1 + c_2 + c_3}{2} \tag{4.33}$$

Given just the four phases $\lambda_1 \ldots \lambda_4$, the largest reachable concurrence for the original gate $\hat{U}_{2q}$ is [39]

$$C(\hat{U}_{2q}) = \max_{k,l} |\sin(\lambda_k - \lambda_l)| \tag{4.34}$$

4.2.3 Non-Entangling Gates

Finding the coefficients c_1, c_2, c_3 from Equations (4.19)–(4.21) can be non-trivial for an arbitrary gate. On the other hand, it is straight-forward to calculate the local invariants G_1 and G_2 from Equations (4.22) and (4.23).

These two quantities are the same for all gates with the same entanglement power, creating an equivalence class. Any two gates in such an equivalence class differ only by local (one-qubit) operations.

We can use this to determine whether a given gate has any non-local component at all: The unity transformation is certainly purely local, which means that all local transformations share the same G_1, G_2 with it. We can calculate that

$$G_1(\mathbb{1}) = 1 \tag{4.35}$$

$$G_2(\mathbb{1}) = 3 \tag{4.36}$$

If for a given gate we find values for G_1 and G_2 that differ from 1 and 3, respectively, we can conclude that the gate has at least some non-local component.

4.2.4 Entangling Gates

On the other end of the spectrum, we can look at the CNOT gate. As we can easily calculate,

$$G_1(\text{CNOT}) = 0 \tag{4.37}$$

$$G_2(\text{CNOT}) = 1 \tag{4.38}$$

If we solve for c_1, c_2, c_3 in Equations (4.19)–(4.21), we end up with a large number of solutions. Following Zhang et al. [38], the c_1, c_2, c_3 parameters can

be interpreted geometrically to position the gate in the space of non-local two-qubit operations. To limit ourselves to the relevant section of this space, the Weyl chamber a^+, we filter our solutions to those fulfilling

$$
\begin{aligned}
c_1 &\geq c_2 \geq c_3 \\
0 &\leq c_1 < \pi \\
0 &\leq c_2 < \pi/2 \\
0 &\leq c_3 < \pi/2
\end{aligned}
\tag{4.39}
$$

This leaves us with only one solution: $c_1 = \pi/2$, $c_2 = c_3 = 0$.

We can immediately calculate the entangling power:

$$
C(\text{CNOT}) = 1
\tag{4.40}
$$

As we expect, the CNOT gate is a perfect entangler. Note that if we look at the π phasegate, we find the exact same values for G_1 and G_2, which verifies that CNOT and π phasegate are equivalent except for local operations, and that both are perfect entanglers.

We can also find the unentangled state that is maximally entangled by the CNOT gate, by solving

$$
C\left[\text{CNOT} \cdot (\alpha_0 \left|0\right\rangle + \alpha_1 \left|1\right\rangle) \otimes (\beta_0 \left|0\right\rangle + \beta_1 \left|1\right\rangle)\right] \overset{!}{=} 1
\tag{4.41}
$$

for α_0, α_1, β_0, and β_1. We find as one possible solution $\alpha_0 = \alpha_1 = 1/\sqrt{2}$, $\beta_0 = 1$, $\beta_1 = 0$. Clearly, this unentangled input state is transformed into a maximally entangled Bell state by the CNOT operation.

If we run through the same procedure for the $\pi/2$ phasegate, we find

$$
G_1\left(\text{CPHASE}\left(\frac{\pi}{2}\right)\right) = \frac{1}{2}
\tag{4.42}
$$

$$
G_2\left(\text{CPHASE}\left(\frac{\pi}{2}\right)\right) = 2
\tag{4.43}
$$

Solving for the Weyl coordinates c_1, c_2, c_3, we find $c_1 = \pi/4$ or $3\pi/4$, $c_2 = c_3 = 0$. The resulting entanglement power is

$$
C\left(\text{CPHASE}\left(\frac{\pi}{2}\right)\right) = 0.7071
\tag{4.44}
$$

More generally, there is a wide class of two-qubit operations for which

$$
G_1\left(\hat{U}_\gamma\right) = \cos^2 \gamma
\tag{4.45}
$$

$$
G_2\left(\hat{U}_\gamma\right) = 1 + 2\cos^2 \gamma
\tag{4.46}
$$

This class includes all controlled two-qubit operations (cf. Zhang et al. [38]). The solution for the Weyl coordinates is $c_1 = \gamma$, $c_2 = c_3 = 0$, as we can guess just by looking at Equations (4.19)–(4.21). The entanglement power of this gate is

$$
C\left(\hat{U}_\gamma\right) = |\sin \gamma|
\tag{4.47}
$$

4.2.5   Application to Phasegate Optimizations

From experience, it is relatively easy for an optimized pulse to return the population the initial logical surface, although not as easy to do this without coupling permanently to the vibrational spectrum. Let us assume for a moment that we also return to the initial vibration eigenstate to a large percentage, so that we can reasonably describe the transformation performed by the optimized pulse to give a phase change for each eigenstate:

$$\hat{U}_{\text{CPHASE}} = \begin{pmatrix} e^{i\phi_{00}} & 0 & 0 & 0 \\ 0 & e^{i\phi_{01}} & 0 & 0 \\ 0 & 0 & e^{i\phi_{10}} & 0 \\ 0 & 0 & 0 & e^{i\phi_{11}} \end{pmatrix} \tag{4.48}$$

We can calculate the local invariants as

$$G_1\left(\hat{U}_{\text{CPHASE}}\right) = \cos^2\left[\frac{1}{2}(\phi_{00} - \phi_{01} - \phi_{10} + \phi_{11})\right] \tag{4.49}$$

$$G_2\left(\hat{U}_{\text{CPHASE}}\right) = 2 + \cos\left[\phi_{00} - \phi_{01} - \phi_{10} + \phi_{11}\right] \tag{4.50}$$

We can define

$$\chi \equiv \phi_{00} - \phi_{01} - \phi_{10} + \phi_{11} \tag{4.51}$$

and rewrite Equations (4.49) and (4.50) as

$$G_1 = \cos^2\frac{\chi}{2} \tag{4.52}$$

$$G_2 = 2 + \cos\phi \tag{4.53}$$

$$= 1 + 2\cos^2\frac{\chi}{2} \tag{4.54}$$

The invariants have exactly the form given in Equations (4.45) and (4.46), with $\gamma = \chi/2$. This means we immediately know the entangling power of our gate:

$$C\left(\hat{U}_{\text{CPHASE}}\right) = \left|\sin\frac{\chi}{2}\right| \tag{4.55}$$

It is remarkable that this is the same entangling power as we would find for a true χ phasegate ($\phi_{00} = \chi$, $\phi_{01} = \phi_{10} = \phi_{11} = 0$). This means that a gate described by the four phases $\phi_{00}, \phi_{01}, \phi_{10}, \phi_{11}$ is locally equivalent to CPHASE(χ), with χ as defined in Equation (4.51). In other words, Equation (4.51) tells us what true two-qubit phase we have achieved in our optimization.

4.2.6   Interaction and Entanglement

Now that we understand how to distinguish between the optimized phases $\phi_{00}, \phi_{01}, \phi_{10}, \phi_{11}$, and the true two-qubit phase χ, we can analyze the results of the optimization attempt without interaction in Section 4.1.2. The dynamics for an optimized pulse are shown in Figure 4.3. Obviously, neither the target for $|00\rangle$ nor $|01\rangle$ is met. There is no reason the target for $|00\rangle$ could not be reached

Figure 4.3: Time evolution of the two-qubit states under the optimized pulse for a π phasegate with global phase $\phi_{00} = 1.513\pi$. The state at $t = 0$ is indicated by a black dot, the state at $t = T$ by a black square. The arrow in each picture indicates the target state. The development of the $|01\rangle$ state is identical to the development of the $|10\rangle$ state, the former is plotted with lines, the latter not. See Section 5.2 for further explanation

in principle: If we optimize with

$$|00\rangle \xrightarrow{\hat{O}} e^{i(\phi + \phi_T)} |00\rangle \tag{4.56}$$

$$|11\rangle \xrightarrow{\hat{O}} e^{i\phi_T} |11\rangle \quad \text{(fulfilled a priori)} \tag{4.57}$$

as the only condition, we find a pulse that generates the time evolution shown in Figure 4.4.

Figure 4.4: Time evolution of the two-qubit states under a pulse for a $\pi/2$ phasegate with global phase $\phi_{00} = 1.513\pi$, including *only* $|00\rangle$ and $|11\rangle$ in the target, but not $|10\rangle$, $|01\rangle$ which conflict with the fulfillment of the $|00\rangle$ target. Compare to Figure 4.3.

Looking at the evolution of the $|01\rangle$ and $|10\rangle$ states in Figure 4.4 gives us an indication what is going on: The states end exactly half way between $\phi_{11} = \phi_T$ and $\phi_{00} = \phi_T + \phi$, indicating that the relative phase between $|00\rangle$ and $|11\rangle$ is only due to single qubit operations.

Trying to optimize for a true two-qubit phase as described by Equations (4.10)–(4.13) proves to be impossible: The optimization merely balances the incompatible targets for $|00\rangle$ and $|01\rangle$, fulfilling both only partly. We can verify that the resulting state can be constructed from single-qubit operations:

$$\hat{U} = e^{i\,0.846\pi} \left[\begin{pmatrix} 1 & 0 \\ 0 & e^{i\,0.334\pi} \end{pmatrix} \otimes \mathbb{1} \cdot \mathbb{1} \otimes \begin{pmatrix} 1 & 0 \\ 0 & e^{i\,0.334\pi} \end{pmatrix} \right] \tag{4.58}$$

The same applies to any other two-qubit phasegate we might try. For example, Figure 4.5 shows the evolution under a pulse optimized for a $\phi = \pi/2$ phasegate. It shows the same fundamental behavior as in Figure 4.3; we could derive the result from a formula analogous to Equation (4.58)
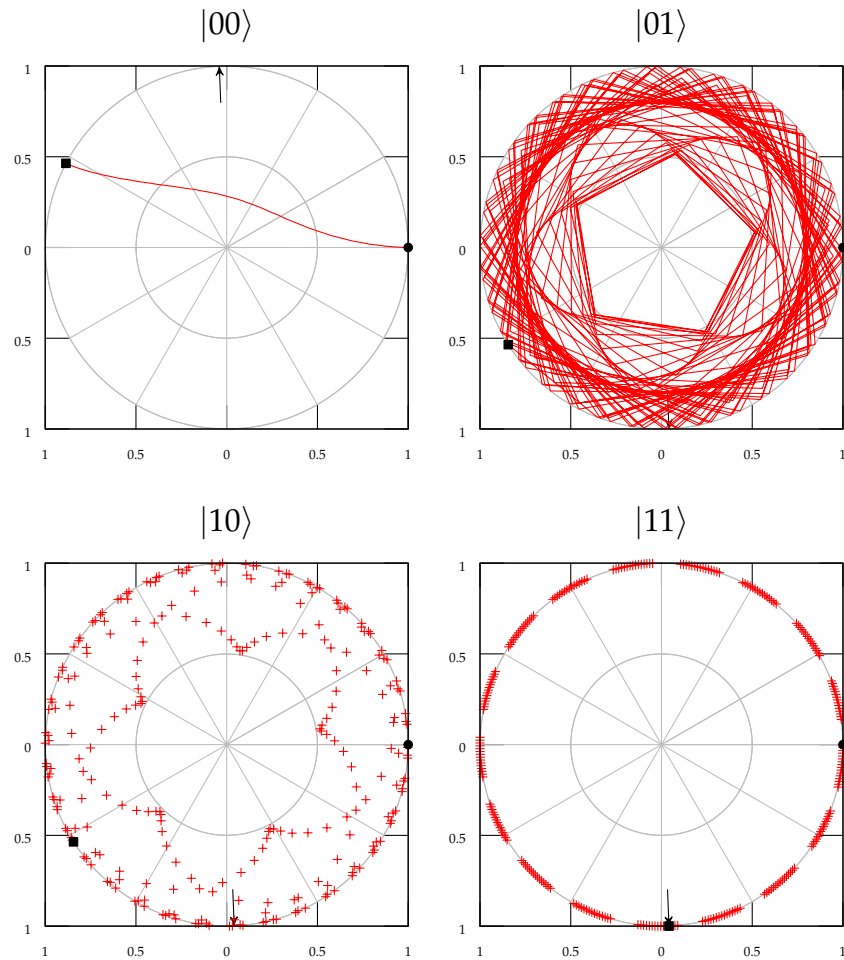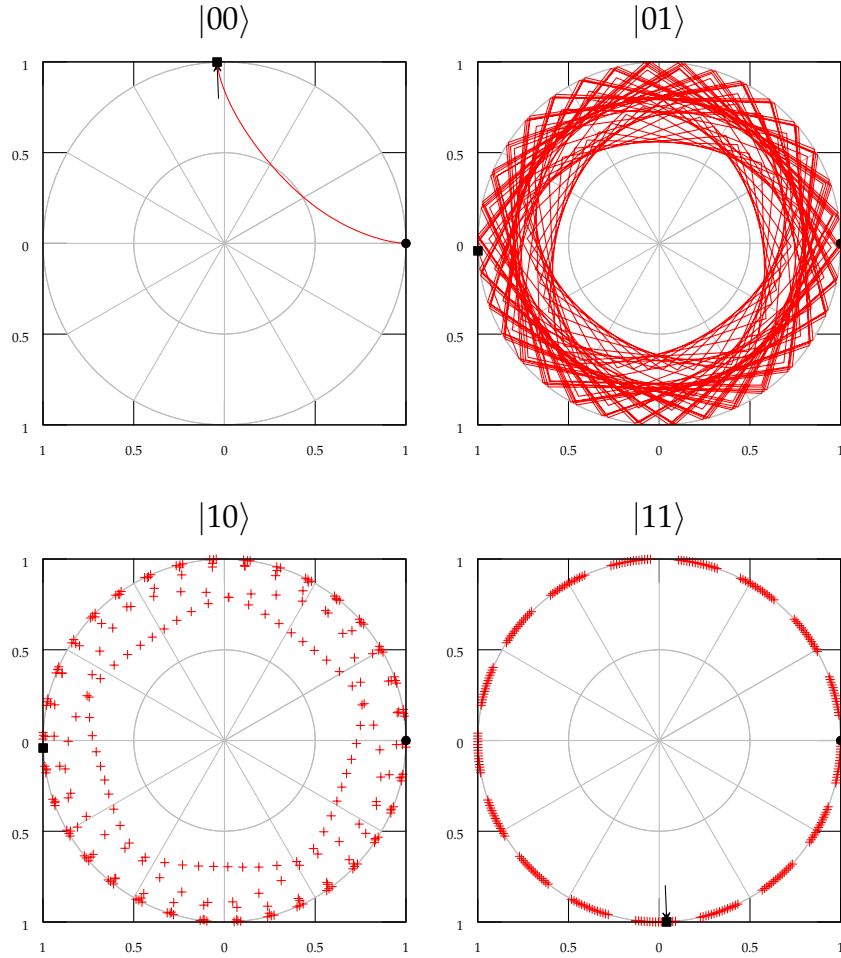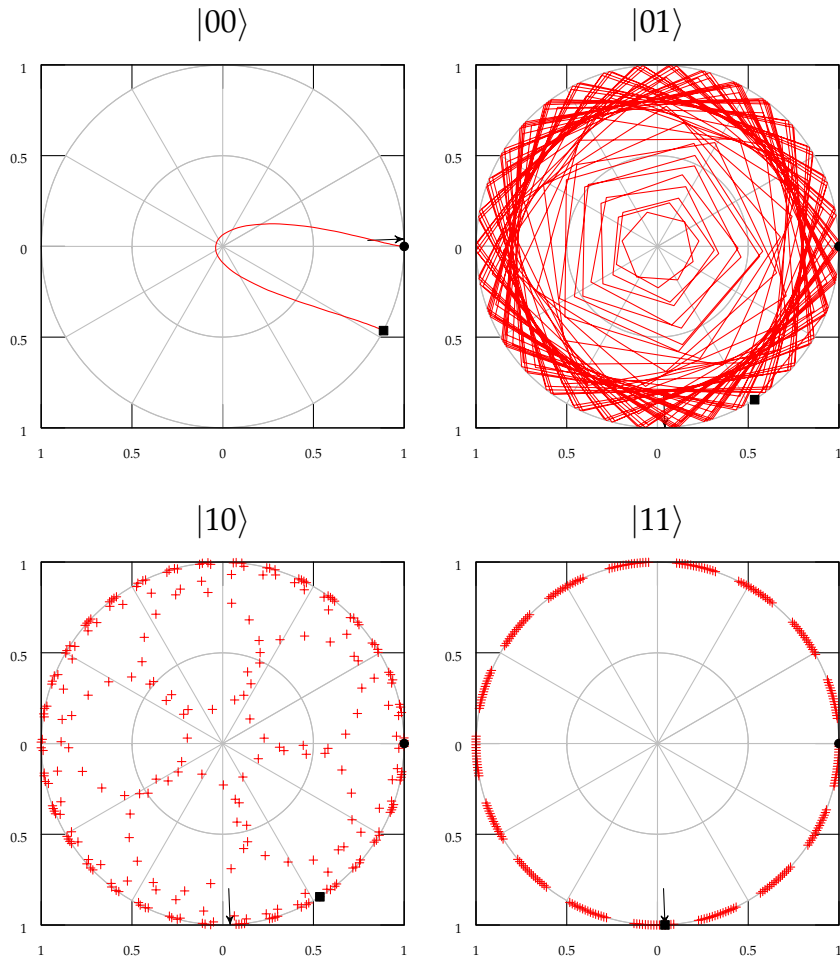

Figure 4.5: Time evolution of the two-qubit states under the optimized pulse for a $\pi/2$ phasegate with global phase $\phi_{00} = 1.513\pi$, in analogy to Figure 4.3.

4.3 Combining Pulses

A lesson of the discussion of Cartan decomposition is that we may have to combine our optimized pulse with additional one-qubit pulses. In principle, we could even use optimal control to find suitable one-qubit pulses. With the current system description, this is not possible, however, as we have not included any way to interact with the $|1\rangle$ state. From a physical point of view, we should also remember that we may have to make dynamic changes to the trapping potential to operate on the same pair of Calcium atoms with one- and two-qubit operations.

On a related thought, we could also try to combine the controlled phasegate with natural time evolution, suggesting the possibility of a slightly different optimization scheme that would leave us with a phasegate of zero global phase: Instead of optimizing for a phasegate with one global phase ϕ_T, we might try:

$$|00\rangle \xrightarrow{\hat{O}} e^{i\phi} |00\rangle \tag{4.59}$$

$$|01\rangle \xrightarrow{\hat{O}} e^{i\phi_{01}} |01\rangle \tag{4.60}$$

$$|10\rangle \xrightarrow{\hat{O}} e^{i\phi_{10}} |10\rangle \tag{4.61}$$

$$|11\rangle \xrightarrow{\hat{O}} e^{i\phi_{11}} |11\rangle \tag{4.62}$$

The phases for the $|01\rangle$, $|10\rangle$, and $|11\rangle$ are the phases from the natural time evolution of these states. If we completed such a gate, we would only have to wait with a pulse of zero amplitude until the phases ϕ_{01}, ϕ_{10}, and ϕ_{11}, reach zero again (due to further time evolution). Since the energy of the $|00\rangle$ state is zero, $|00\rangle$ will not further change its phase, so that we eventually end up with a phasegate with a global phase of zero.

Figure 4.6 shows the result of optimizing such a gate with the non-interaction Hamiltonian. As we would expect, we see no different behavior here: The result is still only due to single-qubit operations. However, the convergence of the optimization is much slower: It is very hard to have a pulse-induced phase for the $|00\rangle$ state while having absolutely zero pulsed-induced phase on the other states. The previous approach of having a pulse-induced phase on all states except $|11\rangle$, gives the optimization more room, and is preferable to attempting a phasegate with $\phi_T = 0$.

4.4 A Reduced Optimization Scheme

Optimizing the full physical two-qubit system is numerically expensive, due to the spatial grid we have to include on each surface, and also due to the number of surfaces. Even if we exclude the $|11(R)\rangle$ state, which does not couple to any other surface, we are still left with a system of eight surfaces. This means for each OCT iteration, we have to propagate eight wave functions over the full spatial and temporal grid at least twice. Of course, we can handle each surface in parallel, but this implies a need for 8-core processors. Likewise, the amount
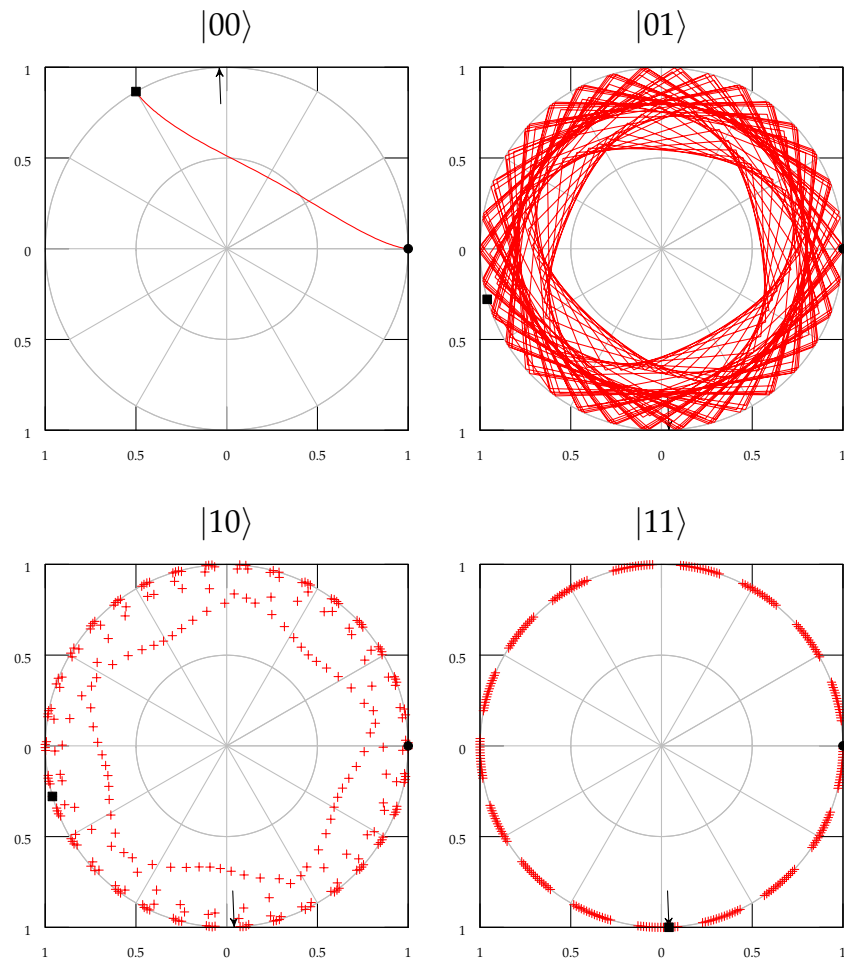
Figure 4.6: Time evolution of the two-qubit states under the optimized pulse for a π phasegate relative to natural evolution of the $|01\rangle$, $|10\rangle$, and $|11\rangle$ states, in analogy to Figure 4.3.
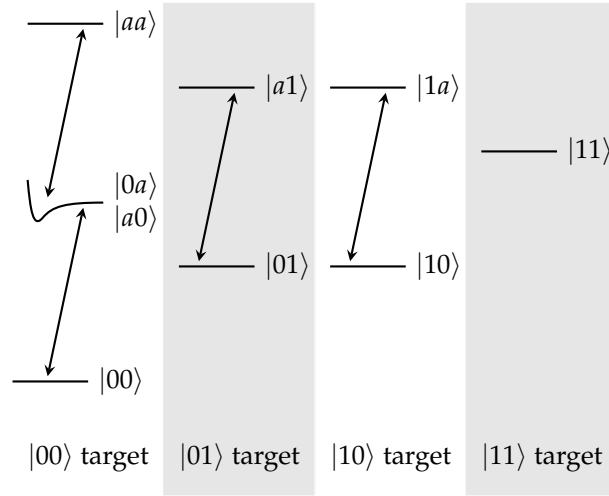
Figure 4.7: Subsystems of the two-qubit system. The transitions affecting the transformation of individual eigenstates fall into distinct partitions.

of memory needed is linear with the number of surfaces. Clearly, we should be interested in trying to avoid taking all surfaces into account.

When we look at the scheme of surfaces in the two-qubit system, we can see that it naturally decomposes into four sub-systems, going alongside the four logical eigenstates (Figure 4.7). As mentioned before, we can completely disregard the $|11\rangle$ system: independently of the pulse, the $|11\rangle$ state will always evolve just with a phase factor of

$$\phi_{11} = \frac{E_{11}}{\hbar}t \tag{4.63}$$

Also, it is obvious that the $|01\rangle$ sub-system is completely identical to the $|10\rangle$ sub-system. If we know the evolution of one, we also know the evolution of the other. Hence, we only have to include one of the two into our optimization. At this point, we have reduced the number of surfaces to six.

Can we do even better? For example, is there a way to predict the evolution of the $|01\rangle$ and $|10\rangle$ states without actually propagating them?

Remember that if we had not included an R-dependent interaction into the two-qubit system compared to the one-qubit system, there would be no true two-qubit phase induced. As we have seen in Section 4.2.6, the dynamics induced by a pulse are completely determined by the phases that the same pulse induces in the one-qubit system:

$$\phi_{00} = 2\phi_0 \tag{4.64}$$
$$\phi_{01} = \phi_{10} = \phi_0 + \phi_1 \tag{4.65}$$
$$\phi_{11} = 2\phi_1 \tag{4.66}$$

Note that in order to make this comparison accurate, we need to adjust the single-qubit energy levels to correspond to the trap ground state energies of

the two-qubit system. To do this, we add half of

$$E_{11}^{\text{vib}} = 0.006667\text{cm}^{-1}.$$

to our single-qubit states. The effect of this on the single-qubit phases is small, but noticeable.

Equation (4.66) is also fulfilled in our full two-qubit description, but clearly Equations (4.64) and (4.65) may not both be fulfilled. After all, our goal is to give the $|00\rangle$ state a phase relative to the other eigenstates.

$$\phi_{00} - \phi_{01} - \phi_{10} + \phi_{11} \overset{!}{\neq} 0 \tag{4.67}$$

We might guess, however, that Equation (4.65) is still fulfilled in our actual two-qubit system, and that our effective two-qubit phase is only due to the violation of Equation (4.64): While we have given all our states an R-dependency, only $|a0\rangle$ and $|a0\rangle$ are not completely flat at the distances we are working at, as indicated in Figure 4.7, due to their $1/R^3$ tail. The states $|01\rangle$ and $|a1\rangle$ in contrast are taken as constant. This is a hint to anticipate that we reach our effective two-qubit phase only from the transformations in the $|00\rangle$ system.

If we assume that compared to Equations (4.64)–(4.66) our full two-qubit phases (including the R-dependent interaction) relate to the one-qubit phases as

$$\phi_{00} \neq 2\phi_0 \tag{4.68}$$
$$\phi_{01} = \phi_{10} = \phi_0 + \phi_1 \tag{4.69}$$
$$\phi_{11} = 2\phi_1, \tag{4.70}$$

we could optimize for a two-qubit ϕ-phasegate with an additional global phase ϕ_T through the targets

$$|00\rangle \overset{!}{\longrightarrow} e^{i(\phi+\phi_T)} |00\rangle \tag{4.71}$$

$$|0\rangle \overset{!}{\longrightarrow} e^{i\phi_T/2} |0\rangle . \tag{4.72}$$

In other words, we only optimize the $|00\rangle$ target in the two-qubit system, consisting of the four surfaces $|00\rangle$, $|0a\rangle$, $|a0\rangle$, and $|aa\rangle$, reducing the computation cost dramatically. The additional optimization in the one-qubit system, which guarantees that we actually reach a two-qubit phase, is numerically easy, as there is no spatial grid for the one-qubit system.

Note that from the results of this mixed optimization we can recover the full characteristics of the two-qubit gate, i.e. the phases the pulse we have obtained generates for all four two-qubit eigenstates. The optimization gives us ϕ_{00} and ϕ_0, directly. Furthermore we know that independently of the pulse, we have

$$\phi_1 = \phi_T/2 \tag{4.73}$$
$$\phi_{11} = \phi_T. \tag{4.74}$$

The phases of the remaining two eigenstates are:

$$\phi_{10} = \phi_{01} = \phi_0 + \phi_1 = \phi_0 + \phi_T/2 \tag{4.75}$$

	full optimization scheme	reduced optimization scheme
system phases	$\phi_{00}, \phi_{01}, \phi_{10}, (\phi_{11})$	$\phi_{00}, \phi_0, (\phi_1)$
optimization targets	$\begin{aligned}|00\rangle &\longrightarrow e^{i(\phi+\phi_T)}|00\rangle \\ |01\rangle &\longrightarrow e^{i\phi_T}|01\rangle \\ |10\rangle &\longrightarrow e^{i\phi_T}|10\rangle\end{aligned}$	$\begin{aligned}|00\rangle &\longrightarrow e^{i(\phi+\phi_T)}|00\rangle \\ |0\rangle &\longrightarrow e^{i\phi_T/2}|0\rangle\end{aligned}$
gate phases	$\begin{aligned}&\phi_{00} \\ \phi_{10} &= \phi_{01} \\ &\phi_{11}\end{aligned}$	$\begin{aligned}&= \phi_{00} \\ &= \phi_0 + \phi_1 \\ &= 2\phi_1\end{aligned}$
true two-qubit phase	$\chi = \phi_{00} - \phi_{01} - \phi_{10} + \phi_{11}$	$\chi = \phi_{00} - 2\phi_0$

Table 4.1: Comparison between full and reduced optimization scheme.

From the four phases ϕ_{00}, ϕ_{01}, ϕ_{10}, ϕ_{11} we can calculate our true two-qubit phase and entangling power.

Of course, this recipe only works if we can demonstrate that our assumptions, Equations (4.68)–(4.70), are fulfilled.

From the optimization of a π-phasegate with a 1 ps pulse, we have obtained a pulse that produces the following phases:

$$\phi_{00} = 0.21009\,\pi$$
$$\phi_{01} = \phi_{10} = 1.78070\,\pi$$
$$\phi_{11} = 1.51265\,\pi$$

If we put this pulse into the one-qubit system, we find

$$\phi_0 = 1.02438\,\pi$$
$$\phi_1 = 0.75632\,\pi$$

for the single-qubit phases. We can calculate

$$2\phi_0 = 0.04875\,\pi$$
$$\phi_0 + \phi_1 = 1.78070\,\pi$$
$$2\phi_1 = 1.51265\,\pi,$$

which matches our expectation exactly. Our assumptions of Equations (4.68)–(4.70) hold. This means we have found a reduced scheme whose optimization is equivalent to the full optimization scheme. The two schemes are compared in Table 4.1. The results which we will discuss in the following chapter are based on both of these.

The fact that the optimization of the full system and the reduced system is equivalent does not imply that we end up with the same optimized pulse, or the same degree of convergence after the same number of optimization steps,

all other parameters equal. In fact, optimizing two equivalent systems for 40 iterations gives us the optimized pulses shown in Figure 4.8. Both pulses are quite distinct, even though they show a roughly similar structure, and it seems possible that both pulses would converge on an identical solution. The fidelities tend to be comparable.

(a) full system   (b) reduced system
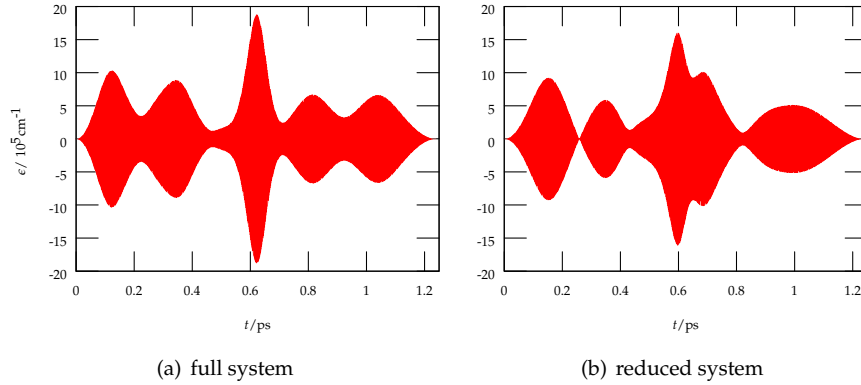
Figure 4.8: Pulses obtained from optimization of equivalent full and reduced systems, after 40 iterations.
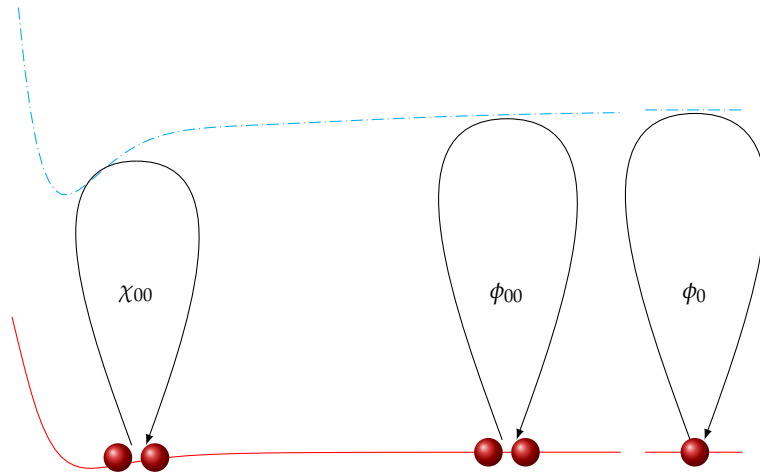
Figure 4.9: Interaction Phase, Optimization Phase, and One-Qubit Phase

In the reduced optimization scheme, the three phases ϕ_0, ϕ_{00} can be interpreted intuitively as depicted in Figure 4.9: The actual two-qubit phase resulting from the optimization ϕ_{00} consists of the true two-qubit phase, or *interaction phase χ*, and the doubled one-qubit contribution ϕ. The latter one is determined by the asymptotic potentials, the former one by the extent that we are still away from the asymptote and feel an interaction in the excited state.

Chapter 5

Optimization Results for the Controlled Phasegate

Understanding the calcium system, its numerical description, and the methods for optimizing a two-qubit controlled phasegate, we turn to the actual optimization and its results. We will first summarize the available parameters and motivate choices for their values, then outline some general observations on the results and finally discuss the results of various approaches in detail.

A tabular summary of all the results presented here can be found in Appendix C. All runs are identified by unique ID numbers that are used both throughout this chapter and in the appendix table.

5.1 Parameters and Optimization Strategies

There are two types of parameters that we can tune in our calculations. First there are the *physical* parameters:

- trap frequency ω and trap distance d

- gate time T

- target phase ϕ

- guess pulse

- OCT pulse shape $S(t)$

Second, there are *numerical* parameters, which only influence the accuracy, numerical efficiency, and convergence.

- spatial grid parameters: $R_{\min}$, $R_{\max}$, N_R

- grid mapping parameters β, $E_{\max}$

- Δt for the temporal grid

- OCT Scaling parameter α.

We choose a fixed trap frequency ω and trap distance d, which implies fixed numerical parameters R_{min}, R_{max}, β, E_{max}. Δt also stays fixed within a small set of values and is determined by the accuracy of the Chebychev propagator for the Calcium system. We vary T, ϕ, and the guess pulse. We also tweak α to control the speed of convergence.

We will now motivate the choices for the fixed parameters, and the strategies for modifying the remaining ones.

5.1.1   Trap Frequency and Trap Distance

What we have seen in the previous chapter is that achieving a two-qubit phase depends crucially on the interaction between the two qubits in the excited state. This interaction is stronger the closer the two Calcium atoms are to each other. As explained in Chapter 2, it is possible to use subwavelength lattices that could generate a grid spacing of $1/4 - 1/8$ of a laser wavelength, so that a value of around $d = 50$ nm would be near the lower end of a realistic range of values for d.

Unfortunately, even at this distance the interaction is too weak to work as a starting point for a phasegate optimization. So, we go to a distance one order of magnitude smaller, and attempt to work at $d = 5$ nm ≈ 100 a.u. As we will see, even at this value, finding an optimal pulse is far from trivial. To understand the limits and possibilities of the optimization process, it makes more sense to explore it systematically at 5 nm before giving any more thought to larger values of d that might be experimentally more feasible.

To have an overlap $< 10^{-4}$ of the trap ground state wavefunctions from neighboring lattice sites, a choice of d so small has to be compensated by choosing an extremely large trap frequency. In Table 2.1 we calculated which frequencies go together with which trap distances so that we can still consider the two Calcium atoms to be independent in the trap ground state. For $d = 5$ nm, we have to choose $\omega = 400$ MHz.

5.1.2   Choice of Guess Pulse

In theory, the choice of a specific guess pulse does not matter for OCT, in the sense that the method will always converge towards an optimal pulse. However, it might do so infinitely slowly so that we are well-advised to start with a motivated choice. There is no obvious way to guess a pulse that in some sense already gets us close to our goal of generating a two-qubit phase, but there are nonetheless some considerations for choosing a guess pulse:

- Our guess pulse should have a frequency tuned to the transition between $|00\rangle$ and $|0a\rangle$ so that it is guaranteed to drive relevant dynamics.

- We do not want to start with a pulse that is more complex than necessary, but rather with a simple Gaussian shape.

- The basic idea behind the phasegate process is that we transfer population from the $|00\rangle$ ground state to the $|0a\rangle$ excited state, where we gather a two-qubit phase due to the interaction there, and then return to the

ground state again. At the end of any gate, there should be no population remaining on a surface that is not part of the qubit encoding. This is in essence a simple Rabi cycle, so that we should start with a 2π-pulse (see below)

From these three ideas, we conclude that as a guess pulse we should use a Gauss-shaped 2π-pulse with a central frequency ω_L tuned to the transition between $|00\rangle$ and $|0a\rangle$.

$$\epsilon(t) = \epsilon_0 \, e^{-\frac{(t-T/2)^2}{2\sigma^2}} \cos(\omega_L t) \tag{5.1}$$

We choose $\sigma = T/8$ in order to fit the pulse in the time interval $[0, T]$, ensuring that the intensity is near zero at $t = 0, T$.

We can calculate the pulse intensity ϵ_0 so that the pulse performs a full Rabi Cycle. With zero detuning of ω_L from the transition frequency between $|00\rangle$ and $|0a\rangle$, the population $a(t)$ oscillates according to[1]

$$a(t) = \left| \cos\left(\int_0^t \frac{1}{2} \Omega(t') \, \mathrm{d}t' \right) \right|^2, \tag{5.2}$$

with the Rabi frequency Ω given as the product of the electric dipole moment and the Gaussian shape of the pulse.

$$\Omega(t) = \mu s(t); \qquad s(t) = \epsilon_0 \, e^{-\frac{(t-T/2)^2}{2\sigma^2}} \tag{5.3}$$

If we solve for the argument of the cosine in Equation (5.2) to yield 2π, we can find the pulse amplitude ϵ_0 for a given time T that performs a full cycle on the population.

$$\epsilon_0 = \frac{\sqrt{2\pi}}{\mu\sigma} = \frac{8\sqrt{2\pi}}{\mu T} \tag{5.4}$$

For a value of $T = 1.23$ ps, for example, and the dipole moment for Calcium $\mu = 4.118$ a.u. [14], we get a pulse amplitude of $\epsilon_0 = 9.53 \times 10^{-5}$ a.u..

The population dynamics that this guess pulse induces in the two-qubit system is shown in Figure 5.1.

As an alternative to a guess pulse with the central frequency ω_L tuned to the full transition $|00\rangle \rightarrow |0a\rangle$, we can also also make use of *three-photon* transitions, and start with guess pulses tuned to one-third the frequency of the $|00\rangle$-$|0a\rangle$ transition. This is illustrated on the right of Figure 5.2. Since the pulse has a certain width, the spectrum also contains frequencies slightly smaller and slightly larger than the central frequency. Different frequencies can combine to add up to the full transition, which means that there are multiple pathways to go from $|00\rangle$ to $|0a\rangle$. This can help in the optimization, as it might be possible to exploit interference between these different pathways. Since three photons must coincide to generate an excitation, three-photon pulses will need to have an increased intensity.

---

[1]See Tannor [23, Chapter 15.1] for a derivation of Rabi cycling.

(a) $|00\rangle$, $|0a\rangle$, $|aa\rangle$ (b) $|01\rangle$, $|a1\rangle$
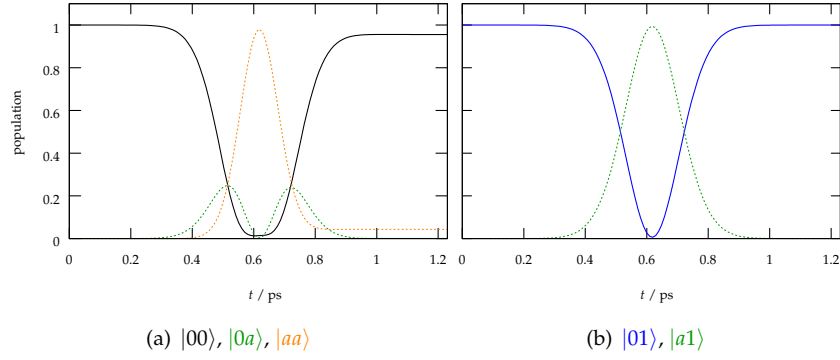
Figure 5.1: Population dynamics in the two-qubit system for the 1 ps guess pulse in run 3220. The dynamics for $|00\rangle$ are extremely similar to the dynamics for $|01\rangle$ (but not identical, due to the presence of the $|aa\rangle$ state). We find that this strong similarity is an indication of a zero two-qubit phase. The one-qubit $|0\rangle$ state, not shown here, behaves identically to the two-qubit $|01\rangle$.
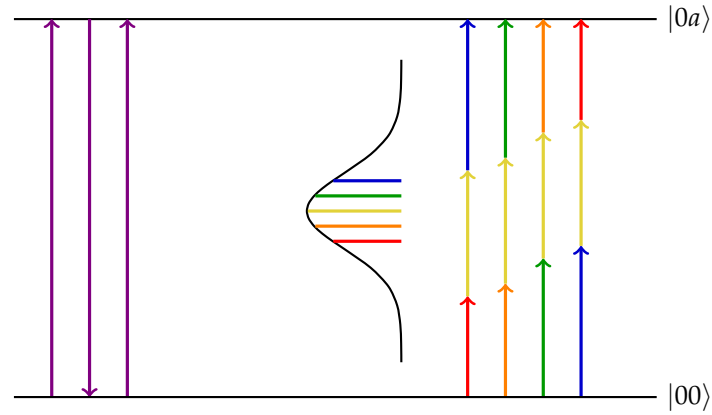
Figure 5.2: Three-Photon transitions. On the left, a photon of frequency $3\omega_0$ ($\omega_0 = \omega(|00\rangle \rightarrow |0a\rangle)$) creates three excitations at once. On the right, three photons from a frequency distribution centered around $\omega = \omega_0/3$ combine. Since there are multiple possible combinations of frequencies reaching from $|00\rangle$ to $|0a\rangle$, optimization can exploit the interference between these different pathways.

5.1.3   Gate Times

We know that a two-qubit phase depends on the interaction between the atoms in the excited state. This means that the pulse should be able to distinguish between the interaction-energy $V_{0a}(R)$ and the asymptotic energy E_{0a} of the non-interacting atoms.

The initial wave function, chosen as the trap ground state, has its population centered around the trap distance d. When the population is pumped to the $|a0\rangle$ surface, it will also be centered around d initially. We therefore take the energy difference between $V_{0a}(R = d)$ and the asymptotic E_{0a} as the energy scale to be resolved by the pulse, which translates to a time scale of $1/(E_{0a} - V_{0a}(d))$. For $d = 5$ nm, we find a value of 1.23 ps, which we take as the minimum starting point for T.

We then systematically try to increase pulse durations, up to 50.0 ps, a point at which the numerical effort involved in the optimization starts to become slightly unwieldy.

The lack of satisfactory results for this range of pulse durations prompted us to look for another physically motivated time scale. We observed that the optimized pulses with the original durations did not return the population to the original vibrational eigenstate on the $|00\rangle$ surface (see Section 5.3).

If we look at the vibrational eigenvalues of the $|00\rangle$ surface, shown in Figure 5.3 and compare the distance between the eigenvalues with the spectral resolution of the time grid given by Equation (3.55), we see that the original pulse durations are not sufficient to resolve between neighboring eigenvalues. Taking the average of the distance between the trap ground state and the next lower and next higher eigenvalue (black lines in Figure 5.3), we find $\Delta E \approx 2 \times 10^{-7}$ a.u. . To resolve this energy difference, we need a pulse duration on the order of 800 ps.

Starting at $T = 800$ ps as an upper limit, we systematically try smaller pulse durations down to $T = 150$ ps in order to see to which extent we need to be able to resolve the vibrational spectrum. Optimization in this regime is far more numerically expensive than the original short-to-medium pulses.

As a third strategy, we ignore all arguments about resolvability, and try extremely short pulses with durations between 0.1 ps and 1.23 ps in order to see whether we can get at least a small two-qubit phase, which then could be accumulated by repeating these short pulses many times.

5.1.4   Optimization Targets

As an alternative to a full π-phasegate, we can also optimize for phasegate with $\phi = \frac{\pi}{n}$, with some integer n. After all, we know that by applying n of such gates in series (with possible one-qubit operations in between), we also would end up with a π-phasegate. However, the error of the individual gates accumulates, so that for pulses of durations longer than 1 ps, we only attempt optimizations for partial phasegates with $n = 2, 3$. Only for the extremely short guess pulses, where can only hope for very small two-qubit phases, we try $n = 4$ and $n = 10$.
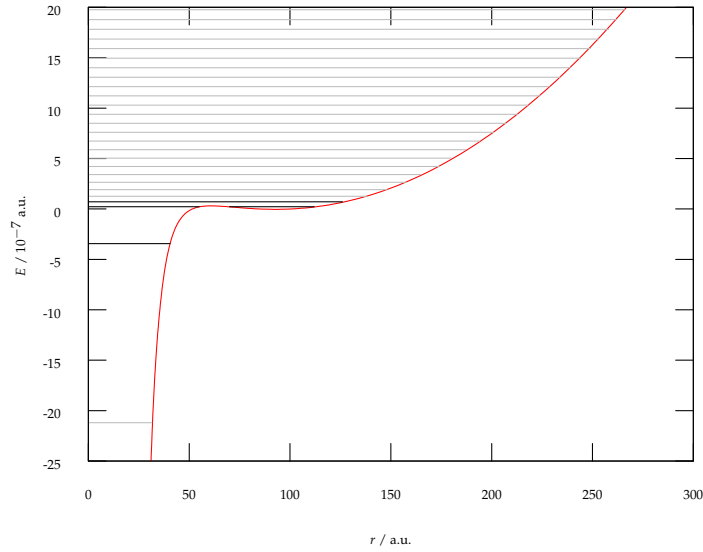
Figure 5.3: Zoom on the vibrational spectrum of the $|00\rangle$ surface. The eigenvalue of the trap ground state as well as the next lowest and next highest eigenvalue are shown in black, other eigenvalues in gray.

We use a full optimization scheme, which includes the two-qubit eigenstates $|00\rangle$, $|01\rangle$ and $|10\rangle$ in the target process, interchangeably with a reduced optimization scheme, which only includes $|00\rangle$ of the two-qubit system, and in addition $|0\rangle$ of the one-qubit system. Both of these schemes are summarized in Table 4.1. The $|11\rangle$ state is not included in the target, as we know its time evolution a-priori.

We have to include the global phase ϕ_T in the target for a specific pulse duration T. The phase is obtained from propagating just the $|11\rangle$ state from 0 to T without any pulse.

5.1.5 Numerical Parameters

For choosing the numerical parameters for the grids, the only considerations are the adequate representation of the system, and that we do not want to waste too many numerical resources by having larger grids than necessary. The concepts that are important for choosing the numerical parameters are explained in Chapter 3.

Specifically for a trap distance of 5 nm, we can motivate the choice of $R_{\min}$ and $R_{\max}$ as well as the number of grid points. $R_{\min}$ is not trap-dependent and should be chosen to accurately represent the inner repulsive slope of the potential. A value of 5 a.u. is sufficient for this. $R_{\max}$ is determined by the number of trap eigenstates that we want to allow to be populated. The harmonic trap potential can only contain eigenstates with eigenvalues smaller than the limit $V_{\text{trap}}(R_{\max})$. Any higher eigenstate would simply "fall out of the trap". In our numerical description, the edges of the grid act as infinite potential wells, and

any eigenstate with an energy higher then $V_{\text{trap}}(R_{\text{max}})$ is not determined by the harmonic trap, but by this well potential.

We choose R_{max} so that the there are 50 trap eigenstates bound by the harmonic potential. This implies that as soon as more trap eigenstates than that are populated, the simulation becomes inaccurate. However, it is very reasonable to put a limit on the number of harmonic eigenstates that we include: Remember that the trap potential is sine-shaped in reality, and that we only approximated it as a harmonic potential. Higher eigenfunctions of the harmonic approximation will not correspond to the eigenfunctions in the sine-potential.

For including 50 eigenstates in the harmonic trap, we can calculate $R_{\text{max}} \approx$ 300 a.u. (15 nm) by solving

$$\frac{1}{2}\mu\omega^2(R_{\text{max}} - d)^2 \overset{!}{=} \hbar\omega\left(n + \frac{1}{2}\right) \tag{5.5}$$

for $n = 50$.

The number of grid points N_R was chosen generously, at 511 or 512 points depending on the mapping. Together with the mapping parameters of $\beta = 0.5$ and $E_{\text{max}} = 1 \times 10^{-8}$, this prevented ghosts from appearing in the spectrum.

The spacing of the time grid is determined by the stability of the Chebychev propagator, visible through the conservation of the norm. For $\Delta t \approx 1 - 2$ a.u., the propagation was fully stable. For very long pulse times > 50 ps, such a fine spacing was not numerically feasible for OCT, so that the propagation was done with $\Delta t = 4$ a.u.. Even for this value, the norm was conserved within the machine precision, and we could show the accuracy post-OCT by propagating the optimized pulses on a finer time grid for analysis.

The shape function for OCT was chosen as as $\sin^2$-function.

$$S(t) = \sin^2\left(\frac{\pi t}{T}\right). \tag{5.6}$$

This means that the changes in the optimized pulse will conform to $S(t)$, guaranteeing a smooth switch-on and witch-off

The scaling parameter α, which regulates how much change OCT is allowed to make to the guess pulse, was found by trial and error to give the fastest convergence for a value of 5000. For values smaller than that, the pulse would change more than was accounted for in the approximation of the spectral radius for the Chebychev propagator.[2] For larger values, the convergence was too slow.

As a general strategy, we can tune α between OCT iterations to allow for greater or smaller changes to the guess pulse.

5.1.6 Summary of Parameter Values and Strategies

To summarize, we do all our runs with the following fixed parameters:

---

[2]Since OCT can change the pulse intensity by a considerable factor, the spectral radius has to be overestimated. We accomplished this by multiplying the pulse with a factor of 5, and estimated the spectral radius based on the resulting Hamiltonian. This allows the optimization to change the maximum intensity of the pulse up to 5 times. If the change is stronger than the, we can compensate by increasing α.

- $R_{\min} = 5.0$ a.u., $R_{\max} = 300.0$ a.u.

- trap parameters $\omega = 400$ MHz, $d = 5$ nm

- $N_R = 511$ for differential mapping, $N_R = 512$ for integral mapping

- $\beta = 0.5$, $E_{\max} = 1 \times 10^{-8}$

- $\sin^2$-shape and $\alpha = 5000$ (initially)

Our optimization strategy is to try guess pulses for different times T:

1. Short/Medium $T = 1.23$ ps, 2.0 ps, 5.0 ps, 8.0 ps, 12.3 ps, 15.0 ps, 30.0 ps, and 50.0 ps

2. Long $T = 800$ ps, 430 ps, 290 ps, 150 ps

3. Extremely short $T = 0.1$ ps, 0.17 ps, 0.5 ps, 1.23 ps

Second, we try three-photon pulses with varying intensity for $T = 1.23$ ps and $T = 12.3$ ps and compare the results to the single-photon pulses. Third, we optimize at $T = 1.23$ ps for partial target phases $\phi = \pi/2, \pi/3$. For the extremely short pulse durations ≤ 1.23ps, we use both one- and three-photon guess pulses, and optimization targets with $\phi = \pi/10$ and $\phi = \pi/4$.

5.2 General Observations

5.2.1 Fidelity, Concurrence, and Vibrational Purity

There are three central quantities that characterize the quality of our optimization result. One is the fidelity as defined in Equation (3.61), applied to either the full or the reduced optimization target (Section 4.4). The second one is the two-qubit phase χ, defined by Equation (4.51), or equivalently the concurrence given by Equation (4.55). Lastly, there is the vibrational purity defined in Equation (2.23)[3], expressing how much population we retain in the gate operation. The fidelity combines the latter two, in the sense that it can only be 1 if both the concurrence and the vibrational purity are 1. It is also the fidelity that drives OCT and which is guaranteed to rise monotonically.[4] Figure 5.2.1 shows an example for the evolution of the fidelity, the concurrence, and the vibrational purity with the number of OCT iterations.

The plot illustrates a number of concepts. First, it shows that the change in fidelity becomes increasingly smaller with the number of iterations. Even after just one iteration, we already have a rather high fidelity. The fidelity increases significantly over the next few iterations, but soon levels off.

---

[3]We have only explicitly defined the vibrational purity for the $|00\rangle$ potential. We can of course do that same for $|01\rangle$, $|10\rangle$, and $|11\rangle$ as well. For $|01\rangle$ and $|10\rangle$ we found the vibrational purity to always be 1, for $|11\rangle$ we even know a-priori that it is 1, since there is no population transfer. Therefore, we only really consider the $|00\rangle$-vibrational purity.

[4]Technically, it is J that is guaranteed to be monotonic, not F, but in practice we always found the fidelity to dominate over the term $\int g(\epsilon)\, \mathrm{d}t$, so that a monotonic behavior of the fidelity is the rule. This can also be influenced by the scaling parameter α

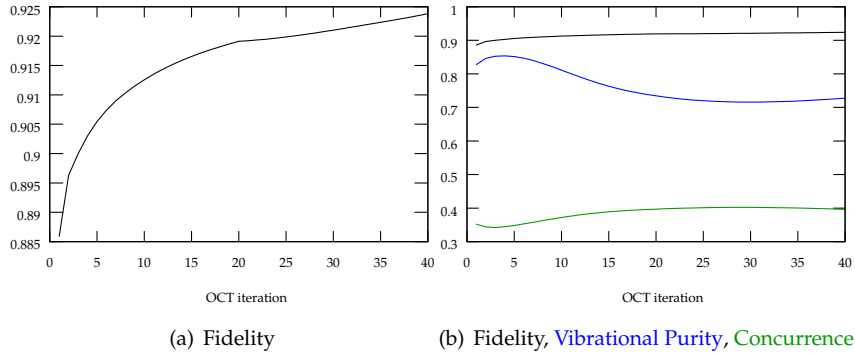(a) Fidelity   (b) Fidelity, Vibrational Purity, Concurrence

Figure 5.4: OCT convergence behavior, from run 3426

We also see that while the fidelity increases monotonically, the concurrence
and the vibrational purity do not. Additionally, the seemingly high fidelity
disguises the fact that we miss our target very significantly, as is much more
evident by looking at the concurrence and the vibrational purity. It seems that
without doing much in terms of true two-qubit operation we already have a
base fidelity significantly higher than what we might have expected. The in-
teresting part of the optimization happens between this base and the maximum
value of 1. In Figure 5.4(b) we get a good impression of how slowly the fidelity
really converges against one. Together, these observations suggest that the fi-
delity is a rather weak indicator of the properties that we really care about, i.e.
creating a true two-qubit gate.

Note the distinct change in the fidelity curve in Figure 5.4(a) at the 20th iter-
ation. At this point the OCT scaling parameter α was reduced from its original
value 5000 down to 500. We see that this speeds up the convergence slightly. As
a general rule, it was beneficial to reduce α whenever the convergence started
to slow down. However, we also found that there was a numerical instability
when α became too small ($\lesssim 60$ in most of our optimizations), leading to an
explosion of the pulse amplitude by many orders of magnitude.

5.2.2   Comparison of Guess Pulse and Optimized Pulse

If we compare the optimized pulses to the original guess pulse, we generally
see that OCT changes the pulse substantially at a qualitative level, as shown in
Figure 5.5. The guess pulse is a simple Rabi pulse, as discussed in the previous
section, whereas the optimized pulse is far more complex. This illustrates that
the specific shape of guess pulse is of lesser importance. However, we also see
that the optimized pulse has an intensity in the same order of magnitude as
the guess pulse. This is generally the case in all optimizations. We made some
attempts to improve the fidelity by boosting the intensity of a pre-optimized
pulse. Taking such a boosted pulse as the guess pulse for further OCT itera-
tions, we generally found optimized pulses in the new intensity range, but not

(a) Guess Pulse   (b) Optimized Pulse
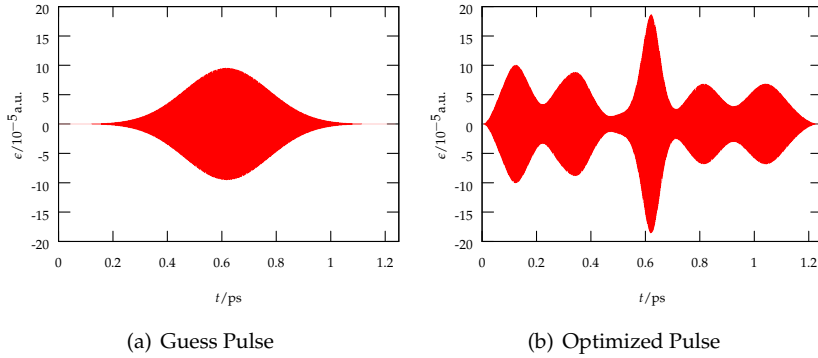
Figure 5.5: Comparison of guess pulse and optimized pulse in run 3220

with any increased fidelity. Changes to the intensity do not seem to have a large effect on the optimization.

(a) $|00\rangle$, $|01\rangle$ (b) $|0\rangle$, $|01\rangle$
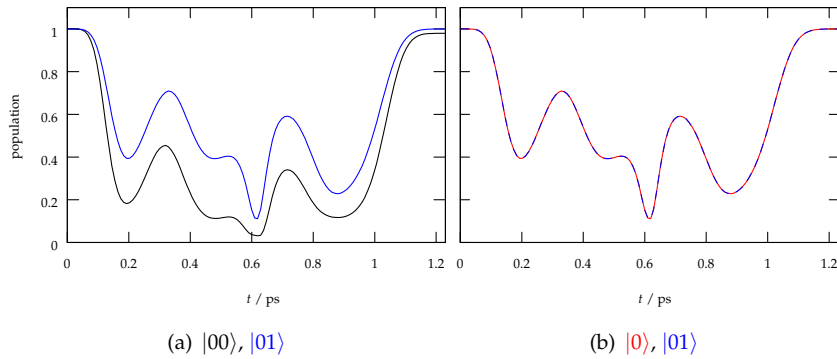
Figure 5.6: Comparison of Population Dynamics under the optimized pulse from run 3220 ($T = 1.23$ ps, $\phi = \pi$) for different eigenstates in the two-qubit and one-qubit system. The $|0\rangle$ eigenstate of the one-qubit system undergoes exactly the same dynamics as the $|01\rangle$ eigenstate in the two-qubit system

If we look at the population dynamics induced by the optimized pulse of Figure 5.5, shown in Figure 5.2.2, we can firstly verify again that they are significantly more complex than the Rabi cycle that the guess pulse induces. Also we can add to our discussion of Section 4.4 about the correspondences between the one-qubit and two-qubit dynamics by comparing the population dynamics that the optimized pulse induces when applied to the two-qubit system initialized to $|00\rangle$ or initialized to $|01\rangle$, and to the one-qubit system initialized to $|0\rangle$. We immediately see that the population dynamics for the single qubit is completely identical to the evolution of the two-qubit $|01\rangle$ state. This is not really surprising if we recall Figure 4.7: The $|10\rangle$ and $|1a\rangle$ states are an isolated two-level system completely analogous to the one-qubit $|0\rangle$ and $|aux\rangle$. There

is of course a motional degree of freedom included in the two-qubit states, but since the interaction potentials are completely flat, we cannot expect any intrinsic two-qubit behavior in this sub-system. This is a reinforcement for our conclusions of Section 4.4 that is it the $1/R^3$ interaction potential defined for the $|0a\rangle$ and $|a0\rangle$ surfaces that bring forth the two-qubit phase.

Even more important than the comparison between the population dynamics is the comparison between the one- and two-qubit phase dynamics under the optimized pulse, shown in Figure 5.2.2.

(a) $|00\rangle$ (b) $|01\rangle$ (c) $|0\rangle$
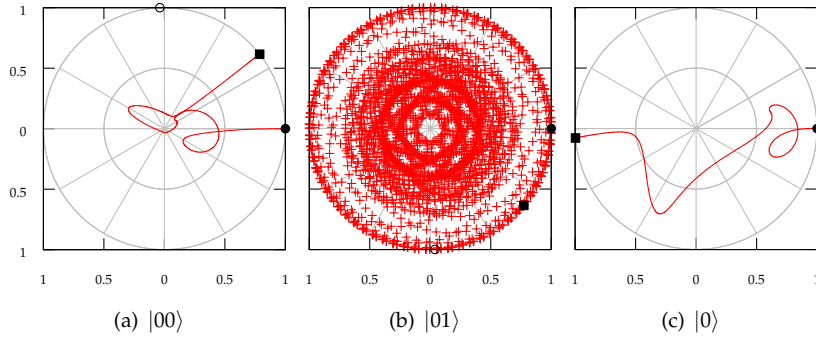
Figure 5.7: Phase dynamics under the optimized pulse for $T = 1.23$ ps, $\phi = \pi$ (run 3220) in the one- and two-qubit system. The blank dot indicate the optimization target phase. The filled dot indicates that starting phase, the filled square the final phase.

For the one-qubit system, what is shown in this plot is directly the complex amplitude a_0 of the $|0\rangle$ eigenstate. In the two-qubit system, there is no single such quantity, as we have a complex amplitude for each point in R. We can however define something analogous: as an *average* phase relative to the original surface wave function,

$$\varphi = \arg\left(\left\langle \Psi_{00}^{(0)}(R)|\Psi_{00}(R)\right\rangle\right) \tag{5.7}$$

We then plot the complex number $|a_{00}|^2 e^{i\varphi}$, where $|a_{00}|^2$ is the population on the $|00\rangle$ surface. For the $|01\rangle$ surface, the definition is analogously.

To verify that the two-qubit phase dynamics are different from the one-qubit dynamics, we observe that doubling the $|0\rangle$ dynamics does *not* yield the $|00\rangle$ dynamics. On the other hand, it looks plausible that the $|01\rangle$ dynamics consist of the $|0\rangle$ dynamics combined with the $|1\rangle$ dynamics, which just goes around the outer circle at constant speed, as shown in Figure 4.1.

5.2.3 Zero Amplitude Guess Pulse

To see the results of the optimization for a pulse of zero amplitude, we took an optimized 1.23 ps three-photon-pulse, extended T to 15 ps without further change, so that the pulse amplitude was zero between 1.23 and 15 ps, and con-

tinued optimization. The resulting optimized pulse is shown in Figure 5.8(a), the spectrum of that pulse in Figure 5.8(b).

(a) pulse   (b) spectrum
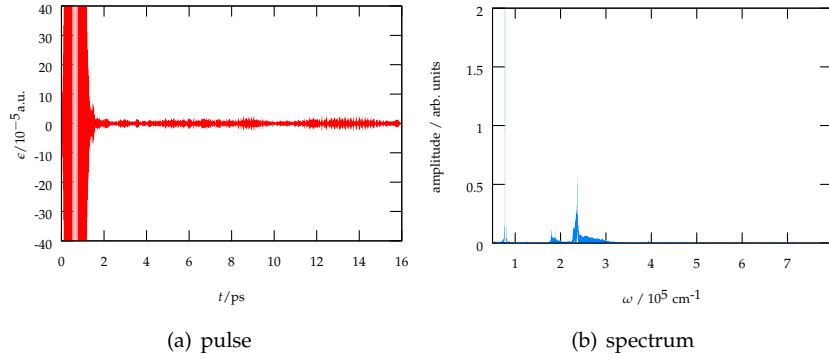
Figure 5.8: Pulse and spectrum of 1.23 ps three-photon pulse from run 3503 extended to 15 ps and optimized in run 888

We see that the optimization adds a low intensity pulse (compare the maximum pulse amplitude with Figure 5.5). The structure of the optimized pulse is extremely complex. A look at the spectrum Figure 5.8(b) shows that indeed the central transition frequency was found (the peak at $\omega_0/3$ is is from the 3-photon part of the pulse at $t < 1.23$ ps and should be disregarded). However, there is also an extremely wide range of frequencies around the central peak, which might generate excitations for levels not included in our description of the physical system. This illustrates the value of having a guess pulse sharply centered around the desired frequency, which also result in much sharper optimized spectra (cf.Figure 5.15)

Interestingly, in terms of the two-qubit phase χ and the vibrational purity, the optimized pulse combines some of the aspects of a 1.23 ps pulse with those of a 15 ps pulse: The reached two-qubit phase was as high as a direct optimization at 15 ps (run 4764), on the other hand the vibrational purity was almost twice as high.

5.3   Gate Times

We now turn to the results for gate times ranging from 1.23 ps to 50 ps. The results for the shortest pulse were used as an example for the dynamics in the previous section. For longer times, the pulses become increasingly more complex. Figure 5.9(a) shows the optimized pulse for 15 ps, which produced the highest two-qubit phase for short-to-medium duration pulses. The complexity is mirrored in the population dynamics in Figure 5.9(b).

The optimization results for the different optimization times are summarized in Table 5.1. We see that with increasing optimization time, we also increase the two-qubit phase, up to a point of 15 ps. On the other hand, the vibrational purity drops dramatically! Since the two-qubit phase is ill-defined

(a) Optimized pulse

(b) Population for $|00\rangle$, $|01\rangle$
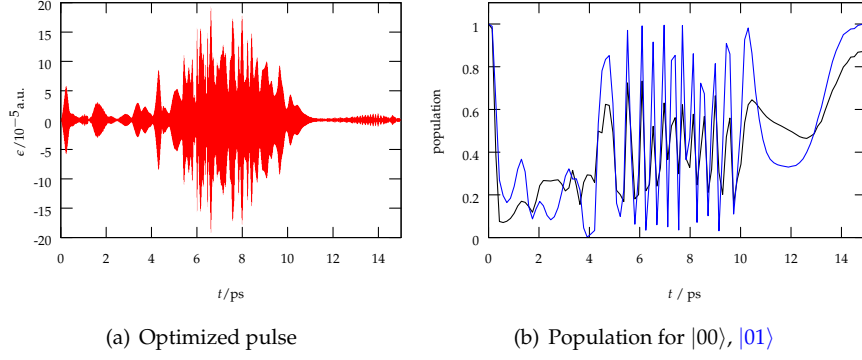
Figure 5.9: Optimized pulse and population dynamics for $T = 15$ ps, $\phi = \pi$ (run 4764)

Run	T/ps	iters	F	χ/π		C	$|00\rangle$ pur.	
3220	1.23	41	0.622	0.162		0.251	0.844	
3185	2.00	15	0.639	0.190		0.294	0.807	
3250	5.00	15	0.719	0.354		0.527	0.589	
3251	8.00	15	0.787	0.560		0.780	0.367	
3466	12.3	50	0.779	0.662		0.862	0.229	
4764	15.0	200	0.773*	0.783		0.943	0.343	
3189	30.0	4	0.630	0.174		0.270	0.014	
2846	50.0	10	0.653	0.266		0.405	0.000	

Table 5.1: Optimization results for different pulse times. The asterisk indicates a fidelity obtained through optimization in the reduced system
.

for small vibrational purities (cf. Section 4.2.5), this also explains the values of χ for $T = 30, 50$ ps. To understand what is happening, we plot the projection on the eigenstates of surface $|00\rangle$ over time for $T = 1.23$ ps and $T = 15$ ps. This is shown in Figure 5.10. We see that there is a considerable spread out in the population over the eigenstates around the trap ground state (eigenstate 41). This problem becomes much worse with longer pulse times. Remember that the phasegate is only successful if we end in the same vibrational state we started in.
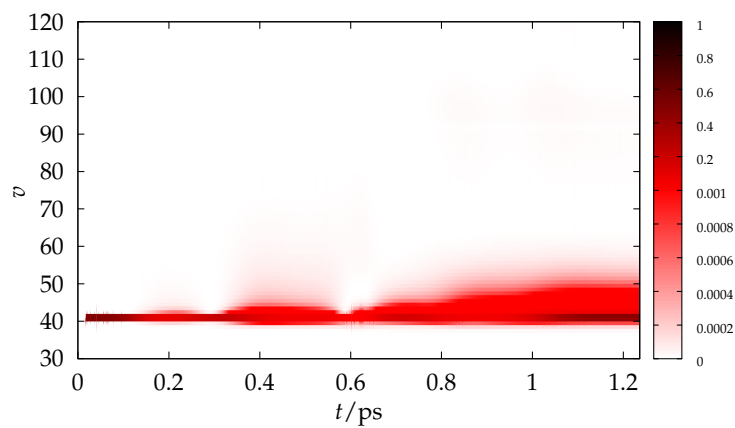
(a) 1.23 ps (run 3220), $|00\rangle$ purity 0.844
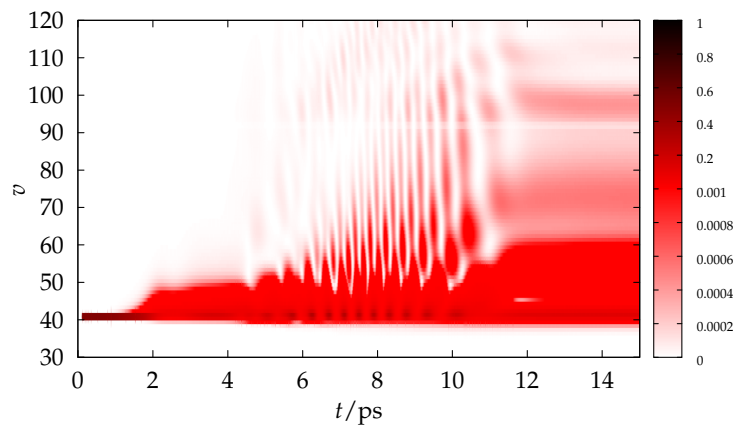
(b) 15 ps (run 3464), $|00\rangle$ purity 0.141

Figure 5.10: Projection onto the eigenstates of the $|00\rangle$ surface. The trap ground state is eigenstate number 41. The target requires that only this eigenstate is populated at the end of the pulse. Note the fault in (b) around level 90, which shows the limit of levels still bound by the harmonic trap.

5.4 Long Pulses

We continue with the results for extremely long pulse durations, starting with $T = 800$ ps which Optimizing for for such large T pushes the boundaries of what is numerically feasible. Even with parallelization, a single OCT iteration for $T = 800$ ps takes about a day.

The results are encouraging, if one accepts gate times significantly longer than we originally envisioned, and are summarized in Table 5.2 together with the earlier results for short-medium length pulses.

T/ps	iters	F	χ/π	C	$|00\rangle$ pur.
1.23	41	0.622	0.162	0.251	0.844
2.00	15	0.639	0.190	0.294	0.807
5.00	15	0.719	0.354	0.527	0.589
8.00	15	0.787	0.560	0.780	0.367
12.36	50	0.779	0.662	0.862	0.229
15.00	200	0.773	0.783	0.943	0.343
30.00	4	0.630	0.174	0.270	0.014
50.00	10	0.653	0.266	0.405	0.000
150.00	20	0.898	0.982	1.000	0.639
290.00	70	0.984	1.004	1.000	0.936
430.00	40	0.998	0.998	1.000	0.991
800.00	30	0.999	0.998	1.000	0.997

Table 5.2: Optimization results for different pulse times (cf. Table 5.1).

For $T = 800$ ps, we reach a very high fidelity and a two-qubit phase close to π. Also, the vibrational purity has an acceptable value. Note that the results shown are after a very small number of iterations; continued optimization would still improve the optimization.

Even for shorter times, we get acceptable results. We see a continuation of the the increase in fidelity and two-qubit phase for increasing times which we already observed for the shorter pulses. However, the vibrational purities also return to a high level. For $T = 290$ ps, we have a loss of 6%, which is acceptable when considering that T is significantly smaller than the full 800 ps and with a larger number of iterations, greater convergence is still possible.

The optimized pulse is shown in Figure 5.11(a) along with the population dynamics in Figure 5.11(b). We see that the optimized pulse is generally oriented towards the original guess pulse, with complex local modifications. This is a different behavior than for short pulse durations (cf. Figure 5.5). This trend continues for increasing pulse durations, the optimized pulse for 800 ps is at first sight almost indistinguishable from the guess pulse.

The remarkable difference between the population dynamics for $|00\rangle$ and $|01\rangle$ shown in Figure 5.11(b) a good indicator for the large two-qubit phase that is reached. We see this directly in he phase dynamics, shown in Figure 5.12. While the phase dynamics are completely chaotic, which is not surprising given the long pulse duration, we immediately see that the target phase

(a) Optimized pulse

(b) Population for $|00\rangle$, $|01\rangle$
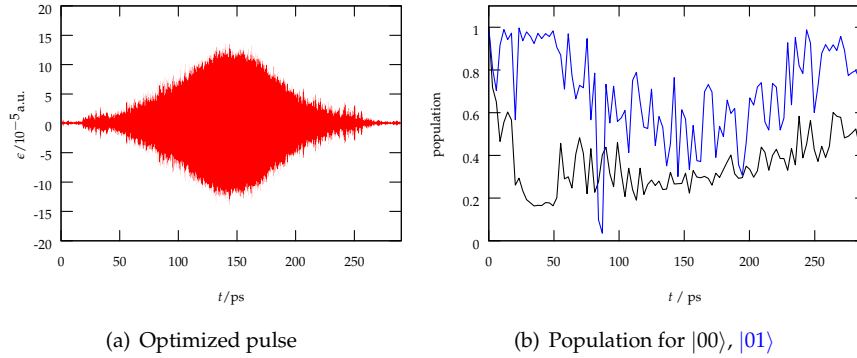
Figure 5.11: Optimized Pulse and Population Dynamics for $T = 290$ ps, $\phi = \pi$ (run 9464)

for the $|00\rangle$ state is nearly fully reach (to the extent that the circle indicating the target phase is not visible due to the overlaying square indicating the reach phase). The target phase for $|0\rangle$ is nearly reached, but not completely. Remember again that we have to double the $|0\rangle$ phase when comparing it with the phase for $|00\rangle$, for the shown dynamics we clearly see that the two phases end up nearly opposite of each other.

(a) $|00\rangle$

(b) $|01\rangle$

(c) $|0\rangle$
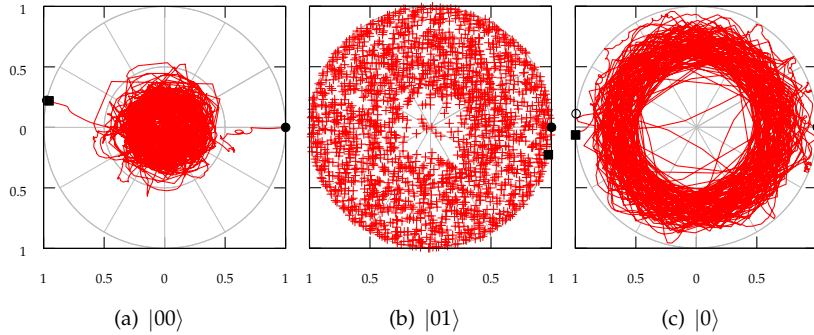
Figure 5.12: Phase Dynamics under optimized pulse for 290 ps, $\phi = \pi$ (run 9464)

5.5 Partial π-Gates

As we have seen, it is extremely hard to find a pulse implementing a π-phasegate. Therefore, arguing that smaller two-qubit phases should be easier to achieve, we run the optimization with a target phase of $\pi/3$ and $\pi/2$. For 1.23 ps, the resulting dynamics are shown in in Figures 5.13 - 5.14.

The fidelities that were reached were significantly higher for the partial-π-phasegates than for the full π-phasegate: 0.96 and 0.89 for the $\pi/3$-gate and

(a) Optimized pulse

(b) Population for $|00\rangle$, $|01\rangle$
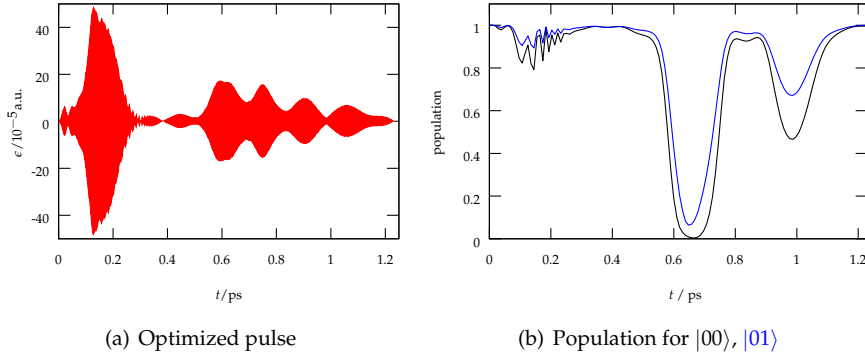
Figure 5.13: Optimized pulse and population dynamics for $T = 1.23$ ps, $\phi = \pi/2$ (run 2854)

the $\pi/2$-gate, respectively, versus 0.62 for the π-gate. However, the phases that were actually achieved were much smaller: 0.06π and 0.07π, versus 0.16. This shows again that even seemingly high fidelities are not necessarily a good indicator of success in terms of true two-qubit operations. Note how the similarity between the $|00\rangle$ and $|01\rangle$ evolution of the population in Figure 5.13(b) is an indicator of the small two-qubit phase that we achieve. Contrast this with Figure 5.11(b).

Comparing Figures 5.13, 5.5(b) and 5.6(a) we can also see that the optimized pulses differ quite significantly from the result for $\phi = \pi$, in their intensity and in the dynamics they drive. We generally find that optimization for different target phases but otherwise identical parameters can yield very different pulses. This observation partially explains that using the optimized pulse from the π-gate as a guess pulse for the fractional π-gates does not yield significantly better results than starting from scratch. The second consideration is that we defined the two-qubit phase in terms of local equivalence, which is not taken into account in the optimization at all. Saying that a pulse generates a true two-qubit phase of χ means that it is possible to combine it with some single-qubit operations so that the optimized pulse together with the single-qubit operations produces a χ phasegate. This does not mean that using the optimized pulse as a guess pulse for a χ-phasegate directly would also generate a high fidelity in our optimization scheme: we are missing the one-qubit operations that produce the equivalence!

The phase dynamics in Figure 5.14 are given for illustration, you may compare them with Figure 5.2.2

5.6 Three-Photon Pulses

When we look at the spectrum of some of the optimized pulses, e.g. the one shown in Figure 5.15, we find a secondary peak at triple the transition frequency.

(a) $|00\rangle$ (b) $|01\rangle$ (c) $|0\rangle$
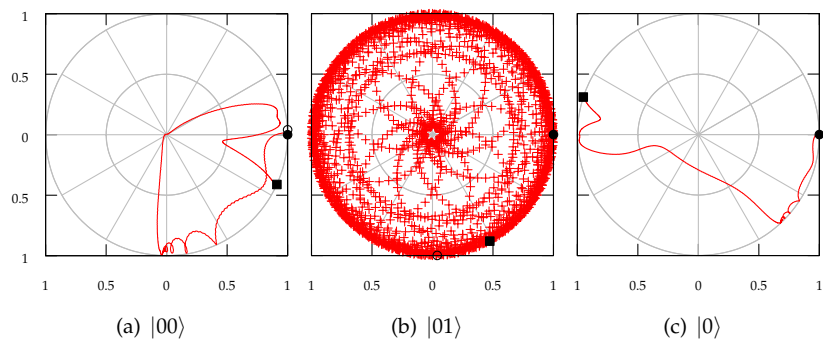
Figure 5.14: Phase Dynamics under optimized pulse for $T = 1.23$ ps, $\phi = \pi/2$
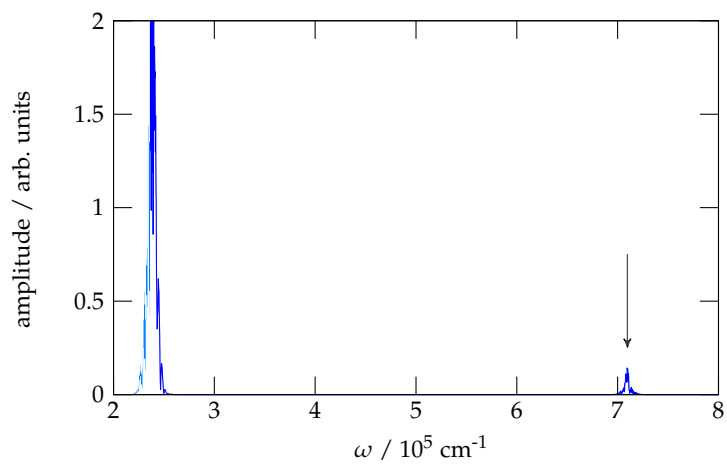(run 2854)

Figure 5.15: Optimized Spectrum for $T = 1.23$ ps, $\phi = \pi/3$ (run 2853), showing
multi-photon excitation.

We can understand this by picturing that a single photon of this high frequency can transfer population over three transitions simultaneously, for example $|00\rangle \rightarrow |0a\rangle \rightarrow |00\rangle$, as illustrated on the left of Figure 5.2. However, there is also a potential problem with this, since the photon might also pump population to higher states, which we did not include in the simulation, or even ionize the Calcium atoms.

On the other hand, we might be able to make use of the reverse process: Instead of starting with a guess pulse tuned to the transition $|00\rangle - |0a\rangle$ we start with one third of that frequency and make use of triple-photon transitions, where three coinciding photons drive one transition. Both the triple-excitation and the three-photon-process are illustrated in Figure 5.2.

Using a multi-photon guess pulse has two potential benefits: we avoid the high frequencies, and also we allow potential interference between different spectral components. The guess pulse will always have a certain spectral width and include frequencies slightly lower and slightly higher than the central frequencies. Three photons with different wavelengths might add up to a single transition, as shown in Figure 5.2.

However, we need to significantly increase the intensity of the laser pulse in order to have a significant probability of three photons coming together for a single transition. Indeed, as shown in Table 5.3, we only get significant dynamics if we increase the intensity by a factor of 100-1000 compared to the single-photon case.

Run	Intensity	T/ps	iters	F	χ/π	$|00\rangle$ purity
9817	(1photon)	1.23	50	0.624	0.165	0.836
3501	$\times 10$	1.23	50	0.500	0.000	1.000
3502	$\times 100$	1.23	50	0.618	0.151	0.885
3503	$\times 1000$	1.23	50	0.602	0.131	0.888
3466	(1photon)	12.3	50	0.779	0.662	0.228
2990	$\times 1$	12.3	10	0.430	0.002	1.000
3173	$\times 100$	12.3	10	0.662	0.238	0.694
4596	$\times 1000$	12.3	75	0.752	0.643	0.272

Table 5.3: Optimization results for three-photon pulses of varying intensity
.

Unfortunately, even once the intensity is sufficiently high, we do not see any significant improvements over the one-photon optimization. While we observed a slightly higher vibrational purity, this was compensated by a smaller two-qubit phase.

The optimized pulse and population dynamics are shown in Figure 5.16. Note the scale of the energy axis in Figure 5.16(a), which is three orders of magnitude higher than the corresponding one-photon pulse (Figure 5.5). The changes due to optimization are practically invisible compared to the energy scale of the pulse. The dynamics shown in Figure 5.16(b) are as complex as a high intensity pulse would suggest.
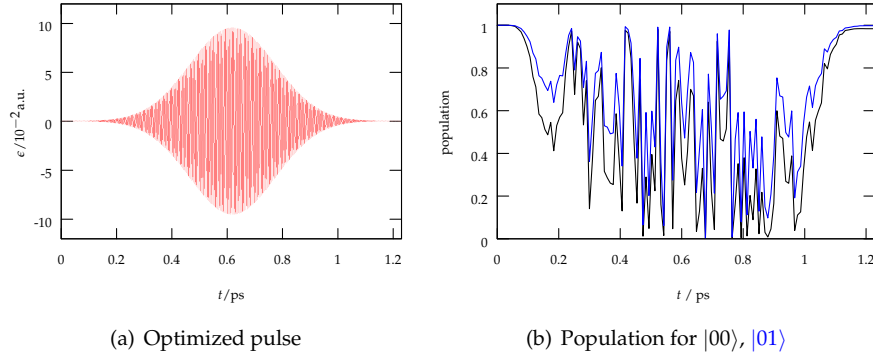
(a) Optimized pulse

(b) Population for $|00\rangle$, $|01\rangle$

Figure 5.16: Optimized pulse and population dynamics for $T = 1.23$ ps, three-photon pulse optimized for $\phi = \pi$ (run 3503)

5.7 Short Pulses, Small Phases

Moving to the other extreme of using ultra-short pulses, we found very much what we expected: We only reach very small two-qubit phases, at a relatively high vibrational purity. The results are summarized in Table 5.4.

Run	pht.	T [ps]	ϕ	iters	F	χ/π	C	$|00\rangle$ pur.
4380	3	0.10	$\pi/10$	50	0.995	0.008	0.012	0.997
4375	3	0.10	$\pi/4$	50	0.970	0.007	0.012	0.997
4374	1	0.10	$\pi/10$	50	0.996	0.008	0.013	0.998
4381	1	0.10	$\pi/4$	50	0.947	0.006	0.010	0.999
9270	3	0.17	$\pi/10$	20000	0.996	0.016	0.026	0.997
9103	3	0.50	$\pi/10$	10000	0.995	0.036	0.057	0.989
4383	3	0.50	$\pi/4$	50	0.974	0.041	0.065	0.980
4376	1	0.50	$\pi/10$	50	0.993	0.032	0.050	0.983
4377	1	0.50	$\pi/4$	50	0.973	0.034	0.054	0.983
4585	3	1.23	$\pi/4$	300	0.973	0.088	0.139	0.944
4593	3	1.23	$\pi/10$	300	0.986	0.087	0.136	0.946
4378	1	1.23	$\pi/10$	50	0.991	0.050	0.079	0.969
4379	1	1.23	$\pi/4$	50	0.971	0.052	0.082	0.963

Table 5.4: Optimization results for short pulses and small target phases. All fidelities were obtained through optimization in the reduced system. Three-photon guess pulses had their intensity increased by a factor of 1000.

Again, three-photon guess pulses did not give a significant improvement over singe-photon pulses.

For illustration, the optimized pulse and pulse dynamics for one of the single-photon pulses is shown in Figures 5.17.

In theory, we can accumulate a phase by putting a large number of such gates in series. For example, just looking at the two-qubit phases, we could

(a) Optimized pulse

(b) Population for $|00\rangle$, $|01\rangle$
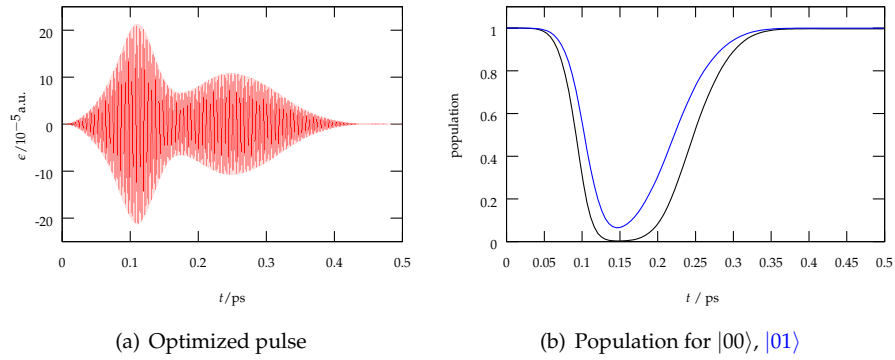
Figure 5.17: Optimized pulse and population dynamics for $T = 0.5$ ps, $\phi = \pi/4$ (run 4377)

(a) $|00\rangle$

(b) $|01\rangle$

(c) $|0\rangle$
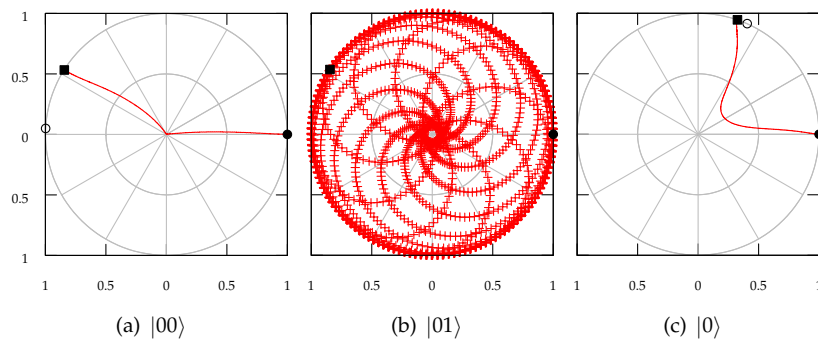
Figure 5.18: Phase Dynamics under optimized three-photon pulse for $T = 0.5$ ps, $\phi = \pi/4$ (run 4377)

repeat the 0.2 ps pulse 61 times to collect a two-qubit phase of near 1, with an expected vibrational purity of $0.99666^61 = 0.82$ The 0.5 ps (run 9103) pulse would only have to be repeated 28 times, yielding an expected vibrational purity of $0.98885^28 = 0.73$

Unfortunately, we cannot exploit this in our optimization scheme directly: the phase deviations $\phi \neq \chi$ accumulate as well, and we would need additional one-qubit operations in between the two-qubit pulses. Indeed, optimizing simply the series of short pulse does not yield good results: For both examples, we get a fidelity of 0.71 with a two-qubit phase of 0.71π and 0.68π respectively, and a vibrational purity of only 0.23 and 0.25.

Chapter 6

Summary and Outlook

To summarize the results of the optimization of the controlled phasegate in the Calcium system, we have seen that our optimization approach has been successful in generating gates of a true two-qubit character as measured by the entangling power and the effective two-qubit phase of the optimized phasegate. However, it has also proved very difficult to reach a full CPHASE(π) target with high fidelity. We find that a satisfactory two-qubit phase ($\approx 0.998\pi$) results only for long pulse durations, on the order of 800 ps, which are near the limit of numerical feasibility. This is the time scale necessary to resolve the vibrational eigenstates of the system around the harmonic trap ground state. For pulse durations between 1 ps and 300 ps, the loss of vibrational purity is a major problem: The population spreads out over the vibrational spectrum; the condition that the system should be in the trap ground state before and after applying the gate pulse is not met. This is a direct consequence of the spectral resolution being too small to distinguish between adjacent vibrational levels. For pulse durations < 1 ps, vibrational purities greater 0.999 could be reached, at the expense of generating an insufficient two-qubit phase $< 0.04\pi$. We did not find the use of high-intensity three-photon guess pulses to result in major improvements. In principle, gates generating small two-qubit phases can be repeated in series, but only if one-qubit operations are inserted: The two-qubit phase χ that results from the optimization is only defined as a local equivalence, i.e. it needs to be combined with one-qubit operations to result in an actual CPHASE(χ). Also, we were only able to find these results for trap distances one order of magnitude smaller than what is currently experimentally feasible. Moving to realistic trap distances and trap frequencies, the interaction due to the excited $1/R^3$ potential would be too small to generate a two-qubit gate. Furthermore, with decreasing trap frequency, the spacing of the trap eigenvalues becomes smaller, which means that we need a time T significantly longer than 800 ps to resolve adjacent vibrational levels.

Nonetheless, there is room for further investigation, both in improving the current approach, and in applying our results to related systems.

6.1   Improvements to the Current Optimization Scheme

In order to explore pulse durations of 400-800 ps and longer, and to increase the number of OCT iterations until full convergence, we can still improve the performance of our simulation. Increasing the use of parallelization, and using highly optimized libraries for FFT/FCT, we would likely be able to reduce the walltime[1] of our optimization runs by a factor of 4-10. Bringing down the walltime from weeks to days would already greatly improve the feasibility of optimizing pulses of long durations.

In addition, we could place further constraints on our pulses that would greatly reduce the difficulties of pulses of long duration. Remember that the spectral resolution

$$\Delta\omega = \frac{2\pi}{T} \tag{6.1}$$

depends only on the pulse duration T (cf. Equation (3.55)). This, however, says nothing about the amplitude of the pulse, only about the time window the pulse is defined on. We have seen that we need a time window of 800 ps to resolve the vibrational levels. If we restrict the pulse to have a non-zero amplitude only in the first and last few picoseconds of this window, this does not change the spectral resolution, and we should be able to find an optimized pulse that has both a high two-qubit phase and a high vibrational purity. Thus, we would have two short sub-pulses in our much longer pulse time window. To prevent OCT from adding amplitude in the middle section of the pulse, we can set the shape function $S(t)$ to be zero in that region. Propagation on the part of the time grid where the pulse is zero could be done very efficiently, as the system follows its known natural time evolution.

If this approach proves successful, it opens up the possibility to significantly reduce the time scales of larger quantum circuits. If we can address individual lattice sites or at least lattice regions, we could perform gates in parallel by applying the first sub-pulse on a given site, move to a different region where we can perform other pulses that would not affect the original site, and return later to apply the second sub-pulse.

6.2   Improved Fidelities for OCT

From our optimization attempts, it has has become very clear that the fidelity

$$F = \frac{1}{N}\Re\left[\sum_{k=1}^{N}\left\langle n_k \left|\hat{O}^\dagger\hat{U}\right| n_k\right\rangle\right] \tag{6.2}$$

is not a strong indicator towards the generation of a true two-qubit phase. In many cases, a large fidelity > 0.9 can be reached performing just one-qubit operations. In such a case, the fidelity after the first OCT iteration will already

---

[1]By *walltime*, we mean the actual time we need to wait for our runs to finish, as opposed to CPU time, which scales with the use of multiple cores

be very high and will continue to increase at a very slow pace in subsequent iterations. This is a typical behavior that we observed our optimizations (see Figure 5.2.1).

From a another point of view, the choice of fidelity is unnecessarily strict. We would be perfectly happy to find a pulse that does not perform a phasegate, but a transformation that is locally equivalent to a phasegate. We already analyzed all our results with this understanding, calculating the true two-qubit phase χ and the concurrence. However, even though a perfect fidelity also implies a perfect χ and concurrence, these quantities are not driving the optimization. We could greatly improve the optimization if we changed the expression for the fidelity to allow for local equivalence, thereby moving the optimization to the Weyl chamber.

The formula for the pulse update, Equation (3.67), was derived specifically for the fidelity in Equation (6.2). Palao and Kosloff [40] also calculate the pulse update for some closely related types of functionals. Deriving a formula for arbitrary other fidelities is not trivial, but can be done by extending the Krotov method to the second order. For example, we could use the comparison of the local invariants G_1, G_2 between the optimized transformation and the target as the fidelity:

$$F(\hat{U}) = \left(G_1\left(\hat{U}\right) - G_1\left(\hat{O}\right)\right) + \left(G_2\left(\hat{U}\right) - G_2\left(\hat{O}\right)\right), \tag{6.3}$$

remapped to the range $[0, 1]$ if necessary. We might also want to use the two-qubit phase χ or the concurrence directly, or even a geometric distance to some target in the Weyl chamber. This extension of OCT, opening up exciting new possibilities, is under active research.

6.3 Using Dipole-Dipole Interactions in Rydberg Atoms

Our optimization was only successful for trap distances one order of magnitude smaller than experimentally feasible. For larger distances, the interaction between the atoms in the excited states is too small. If we implement our phasegate using Rydberg states, as proposed by Jaksch et al. [41], we can make use of a much stronger dipole interaction. We can easily extend our optimization scheme to test how much interaction strength is needed to obtain a two-qubit phase for realistic trap parameters. To this end, we would set d to several micrometer, but use an analytic interaction potential. The long-range interaction potential is dominated by the dipole term

$$V_{\mathrm{dip}}(R) = \frac{C_3}{R^3}. \tag{6.4}$$

We would then vary the constant C_3, starting for example from the value given by Gaëtan et al. [42] for Rubidium, to find the minimum value for which the optimization of the controlled phasegate is still successful.

6.4   Applying the Controlled Phasegate to Rubidium

Many proposals for quantum computing with neutral atoms in optical lattices work with Rubidium. Therefore, we briefly discuss the foundations of how the phasegate that we have discussed for Calcium applies to the generally more familiar Rubidium.

As opposed to Calcium, where we encoded the qubits in the electronic ground state and excited level, the encoding in Rubidium is usually in the hyperfine states of the electronic ground state.

The ^{87}Rb isotope has a nuclear spin of $I = 3/2$. Due to the interaction of this nuclear spin with the orbital angular momentum $J = \frac{1}{2}$, the ground state splits up into two hyperfine levels $f = I \pm J = 2, 3$. Furthermore, there are the Zeeman sub-levels $m_f = -f \cdots + f$. In total, the qubit state can be written as $\left| f, m_f \right\rangle$. We encode the qubit in two (magnetic) hyperfine states of the electronic ground state:

$$
\begin{aligned}
|0\rangle &= \left| f = f_0, m_f = m_{f_0} \right\rangle \\
|1\rangle &= \left| f = f_1, m_f = m_{f_1} \right\rangle
\end{aligned}
\tag{6.5}
$$

For example, we can choose

$$
|0\rangle = |2, -2\rangle^f, \qquad |1\rangle = |2, +2\rangle^f
\tag{6.6}
$$

The two-qubit states are then

$$
\begin{aligned}
|00\rangle &= \left| f_0, m_{f_0} \right\rangle \left| f_0, m_{f_0} \right\rangle \\
|01\rangle &= \left| f_0, m_{f_0} \right\rangle \left| f_1, m_{f_1} \right\rangle \\
|10\rangle &= \left| f_1, m_{f_1} \right\rangle \left| f_0, m_{f_0} \right\rangle \\
|11\rangle &= \left| f_1, m_{f_1} \right\rangle \left| f_1, m_{f_1} \right\rangle
\end{aligned}
\tag{6.7}
$$

Based on the energies of the hyperfine splitting given by Steck [43], a laser pulse would have to be on the order of 150 ps in order to resolve just the hyperfine states. For the relevant Zeeman levels, with a Landé factor of 0.7 MHz/G, and weak magnetic fields of 10 G, this time scale increases to the order of microsecond. This also gives us the time scale of one-qubit operations.

For shorter pulses on the order of picoseconds, a laser pulse only drives transitions between the singlet and triplet electronic states, written as $|S, M_S\rangle$. To describe the effect of the laser, we have to change from the hyperfine basis of Equation (6.7) to the molecular spin basis, using Clebsch-Gordon-Coefficients.

$$
\left| f_1, m_{f_1} \right\rangle \left| f_0, m_{f_0} \right\rangle = \sum_{SM_S IM_I} M_{(SM_S IM_I)}^{(f_1 m_{f_1} f_0 m_{f_0})} |S, M_S\rangle |I, M_I\rangle
\tag{6.8}
$$

If we write down the phasegate in the logical basis of Equation (6.7), we get:

$$
\hat{O} = \sum_{(ij)} e^{i\phi_{(ij)}} \left| f_i, m_{f_i} \right\rangle \left| f_j, m_{f_j} \right\rangle \left\langle f_j, m_{f_j} \right| \left\langle f_i, m_{f_i} \right|
\tag{6.9}
$$

Rewriting this in the molecular spin basis, this becomes:

$$\hat{O} = \sum_{\substack{(S,M_S,I,M_I), \\ (S',M'_S,I',M'_I)}} O_{(S,M_S,I,M_I)}^{(S',M'_S,I',M'_I)} |S, M_S\rangle\, |I, M_I\rangle\langle I', M'_I|\, \langle S', M'_S| \qquad (6.10)$$

with the matrix elements

$$O_{(S,M_S,I,M_I)}^{(S',M'_S,I',M'_I)} = \sum_{(ij)} e^{i\phi_{ij}} M_{(SM_S IM_I)}^{(f_i m_{f_i} f_j m_{f_j})} M_{(S'M'_S I'M'_I)}^{(f_i m_{f_i} f_j m_{f_j})\,*} \qquad (6.11)$$

As long as we know all the Clebsch-Gordon-Coefficients M, we can write down the explicit controlled phasegate transformation matrix for in the molecular spin basis. This directly gives us the optimization targets for the logical states.

There is a problem, however. When we look at the effect that a pulse has on the spin states, and transform this into the complete hyperfine basis, we find that generally, the pulse will lead out of the logical subspace. This means that it is not sufficient to include only the logical basis in the optimization. We can ease this problem somewhat by searching for a set of hyperfine states as the logical basis so that the subspace reached the laser pulse is as small as possible. Still, there will be some spurious states, which we will have to clean up by applying additional pulses directly at the hyperfine level, i.e. on the time scale of microseconds. In addition, even if we manage to get fast two-qubit gates for Rubidium, we are still limited by the speed of one-qubit operations.

.

Appendix A

Derivation of the Born-Oppenheimer Potentials

The Hamiltonian for a system of two identical atoms is

$$\hat{H} = -\frac{\hbar}{2m_e}\sum_i \nabla^2_{e_i} - \frac{\hbar}{2M}\sum_{A=1,2}\nabla^2_{N_A} -$$
$$-\sum_{A=1,2;i}\frac{Ze^2}{4\pi\epsilon_0 r_{Ai}} + \frac{Z^2 e^2}{R} + \sum_{i>j}\frac{e^2}{4\pi\epsilon_0 r_{ij}}, \tag{A.1}$$

where r_{Ai} is the distance from nucleus A to electron i, r_{ij} is the distance between two electrons i, j, and R is the distance between the two nuclei. M is the mass of one nucleus, m_e is the electron mass, Z the nucleus' mass number. In atomic units this becomes

$$\hat{H} = -\sum_i \frac{\nabla_i^2}{2} - \sum_A \frac{\nabla_A^2}{2M} - \sum_{A,i}\frac{Z_A}{r_{Ai}} + \frac{Z^2}{R} + \sum_{i>j}\frac{1}{r_{ij}} \tag{A.2}$$
$$= \hat{T}_e(\vec{r}) + \hat{T}_N(\vec{R}) + \hat{V}_{eN}(\vec{r},\vec{R}) + \hat{V}_{NN}(\vec{R}) + \hat{V}_{ee}(\vec{r}).$$

The vectors indicate the collection of the various electronic and nuclear coordinates.

We assume that the nuclear motion happens on a much slower time scale than the electronic motion (due to the high ratio of the proton mass to the electron mass), so that the we can solve the electronic problem parametrically for a given nuclear configuration $\vec{R}$:

$$\hat{H}_{el}\Psi(\vec{r};\vec{R}) = E_{el}\Psi(\vec{r};\vec{R}) \tag{A.3}$$

with

$$\hat{H}_{el} = \hat{T}_{el}(\vec{r}) + \hat{V}_{eN}(\vec{r};\vec{R}) + \hat{V}_{ee}(\vec{r}) + V_{NN,\vec{R}}. \tag{A.4}$$

The last term is a constant shift to the energy spectrum.

We assume the electronic Schrödinger equation solved by a set of eigenfunctions $\Psi_k(\vec{r};\vec{R})$. This allows us to expand the solutions to the full Schrödinger

equation as

$$\Psi(\vec{r}, \vec{R}) = \sum_k \chi_k(\vec{R}) \Psi_k(\vec{r}; \vec{R}) \tag{A.5}$$

We write out the full Schrödinger equation and integrate out the electronic degree of freedom:

$$\int \Psi_k^* \hat{H} \sum_{k'} \Psi_{k'} \chi_{k'}(\vec{R}) \; d\vec{r} = \int \Psi_k^* E \sum_{k''} \Psi_{k''} \chi_{k''}(\vec{R}) \; d\vec{r}. \tag{A.6}$$

Due to the orthonormality of the eigenfunctions

$$\langle \Psi_k | \Psi_{k''} \rangle = \delta_{k,k''}, \tag{A.7}$$

the right hand side becomes

$$\int \Psi_k^* E \sum_{k''} \Psi_{k''} \chi_{k''}(\vec{R}) \; d\vec{r} = E \chi_k(\vec{R}). \tag{A.8}$$

For the left hand side, remembering that

$$\hat{H} = \hat{H}_{el} + \hat{T}_N, \tag{A.9}$$

we get

$$\int \Psi_k^* \hat{H} \sum_{k'} \Psi_{k'} \chi_{k'}(\vec{R}) \; d\vec{r}$$
$$= \sum_{k'} \langle \Psi_k | \hat{H}_{el} | \Psi_{k'} \rangle \chi_{k'}(\vec{R}) + \sum_{k'} \left\langle \Psi_k \left| \sum_A \frac{\nabla_A^2}{2M} \right| \Psi_{k'}(\vec{r}; \vec{R}) \chi_{k'}(\vec{R}) \right\rangle \tag{A.10}$$
$$= \langle \Psi_k | \hat{H}_{el} | \Psi_k \rangle \chi_k(\vec{R}) + \sum_{k',A} \frac{1}{2M} \left\langle \Psi_k \left| \nabla_A^2 \right| \Psi_{k'}(\vec{r}; \vec{R}) \chi_{k'}(\vec{R}) \right\rangle$$

In the last line, we used that the electronic Hamiltonian is diagonal in basis of the electronic eigenfunctions $|\Psi_k\rangle$.

We can now expand the rightmost term by applying the chain rule.

$$\left\langle \Psi_k \left| \nabla_A^2 \right| \Psi_{k'}(\vec{r}; \vec{R}) \chi_{k'}(\vec{R}) \right\rangle$$
$$= \left\langle \Psi_k \left| \nabla_A^2 \right| \Psi_{k'} \right\rangle \chi_{k'} + 2 \left\langle \Psi_k | \nabla_A | \Psi_{k'} \right\rangle \nabla_A \chi_{k'} + \left\langle \Psi_k | \Psi_{k'} \right\rangle \nabla_A^2 \chi_{k'} \tag{A.11}$$
$$= \left\langle \Psi_k \left| \nabla_A^2 \right| \Psi_{k'} \right\rangle \chi_{k'} + 2 \left\langle \Psi_k | \nabla_A | \Psi_{k'} \right\rangle \nabla_A \chi_{k'} + \delta_{kk'} \nabla_A^2 \chi_{k'}$$

At this point, we neglect the terms $\langle \Psi_k | \nabla_A | \Psi_{k'} \rangle$, and $\langle \Psi_k | \nabla_A^2 | \Psi_{k'} \rangle$, so that if we insert everything back into Equation (A.10), we get

$$\int \Psi_k^* \hat{H} \sum_{k'} \Psi_{k'} \chi_{k'}(\vec{R}) \; d\vec{r} = \langle \Psi_k | \hat{H}_{el} | \Psi_k \rangle \chi_k(\vec{R}) + \sum_A \frac{\nabla_A^2}{2M} \chi_k(\vec{R}) \tag{A.12}$$

Comparing Equations (A.12) and (A.8), we see that

$$\frac{\nabla_A^2}{2M} \chi_k(\vec{R}) + \langle \Psi_k | \hat{H}_{el} | \Psi_k \rangle \chi_k(\vec{R}) = E \chi_k(\vec{R})) \tag{A.13}$$

which is a Schrödinger equation for the nuclear wave function $\chi_k(\vec{R})$. The nuclei move in a so-called Born-Oppenheimer potential

$$\hat{V}_{BO} \equiv \left\langle \Psi_k \left| \hat{H}_{el} \right| \Psi_k \right\rangle. \qquad \text{(A.14)}$$

consisting of the expectation values of the electronic energy at each point.

$$\left(\hat{T}_N + \hat{V}_{BO}(\vec{R}) \right) \chi_k(\vec{R}) = E\, \chi_k(\vec{R})) \qquad \text{(A.15)}$$

For a detailed discussion of the justifications for the approximations made in the derivation of the Born-Oppenheimer potential, and a treatment in polar coordinates, see Chapter 11 of Haken and Wolf [44].

Appendix B

Trap-Hamiltonian in Relative Coordinates

We prove the equivalence of the trap Hamiltonian

$$\hat{H}_{\text{trap}}(R, X) = -\frac{\hbar^2}{2M} \nabla_X^2 + \frac{1}{2} M \omega^2 X^2 - \frac{\hbar^2}{2\mu} \nabla_R^2 + \frac{1}{2} \mu \omega^2 (R - d)^2 \qquad \text{(B.1)}$$

in center-of-mass coordinates

$$X = \frac{x_1 + x_2}{2} \qquad \text{(B.2)}$$

$$M = 2m \qquad \text{(B.3)}$$

and relative coordinates

$$R = x_2 - x_1 \qquad \text{(B.4)}$$

$$\mu = m/2, \qquad \text{(B.5)}$$

to the trap Hamiltonian in single particle coordinates x_1, x_2

$$H_{\text{trap}}(x_1, x_2) = -\frac{\hbar^2}{2m} \left(\nabla_1^2 + \nabla_2^2 \right) +$$
$$+ \frac{1}{2} m \omega^2 \left(x_1 + \frac{d}{2} \right)^2 + \frac{1}{2} m \omega^2 \left(x_2 - \frac{d}{2} \right)^2. \qquad \text{(B.6)}$$

We start with the Hamiltonian in COM/relative coordinates and work backwards. At first, let us consider the terms $\frac{1}{2} M \omega^2 X^2$ and $\frac{1}{2} \mu \omega^2 (R - d)^2$. We note that

$$R - d = x_2 - x_1 - d$$
$$= \left(x_2 - \frac{d}{2} \right) - \left(x_1 + \frac{d}{2} \right) \qquad \text{(B.7)}$$
$$= x_2' - x_1'$$

with the abbreviation

$$x_1' = x_1 + \frac{d}{2} \tag{B.8}$$

$$x_2' = x_2 - \frac{d}{2} \tag{B.9}$$

We can write

$$
\begin{aligned}
\frac{1}{2} M\omega^2 X^2 + \frac{1}{2}\mu\omega^2 (R-d)^2 &= \\
&= \frac{1}{2} 2m\omega^2 \frac{1}{4}\left(x_1^2 + x_2^2 + 2x_1 x_2\right) + \frac{1}{2}\frac{m}{2}\omega^2\left(x_1'^2 + x_2'^2 - 2x_1' x_2'\right) \\
&= \frac{1}{4} m\omega^2 \left[x_1^2 + x_2^2 + 2x_1 x_2 + x_1'^2 + x_2'^2 - 2x_1' x_2'\right]
\end{aligned}
\tag{B.10}
$$

We can easily show shat the expression in the square brackets evaluates to

$$\left[x_1^2 + x_2^2 + 2x_1 x_2 + x_1'^2 + x_2'^2 - 2x_1' x_2'\right] = 2\left[\left(x_1 + \frac{d}{2}\right)^2 + \left(x_2 - \frac{d}{2}\right)\right] \tag{B.11}$$

by verifying that

$$x_1^2 + x_2^2 + 2x_1 x_2 - 2\left(x_1 + \frac{d}{2}\right)\left(x_2 - \frac{d}{2}\right) = \left(x_1 + \frac{d}{2}\right)^2 + \left(x_2 - \frac{d}{2}\right)^2 \tag{B.12}$$

Taking all this together, this means

$$\frac{1}{2} M\omega^2 X^2 + \frac{1}{2}\mu\omega^2 (R-d)^2 = \frac{1}{2} m\omega^2\left(x_1 + \frac{d}{2}\right)^2 + \frac{1}{2} m\omega^2\left(x_2 - \frac{d}{2}\right)^2 \tag{B.13}$$

The kinetic operator can be handles analogously, using

$$\nabla_X^2 = (2\nabla_1 + 2\nabla_2)^2 = 4\left[\nabla_1^2 + \nabla_2^2 + 2\nabla_1\nabla_2\right] \tag{B.14}$$

$$\nabla_R^2 = (2\nabla_1 - \nabla_2)^2 = \left[\nabla_1^2 + \nabla_2^2 - 2\nabla_1\nabla_2\right] \tag{B.15}$$

Together, this proves the equivalence of Equation (B.1) to Equation (B.6).

Appendix C

Table of Optimization Results

The table on the following page summarizes the results discussed in Chapter 5.

Each run is identified by an ID number in the first column.

The number of photons indicates the central frequency ω_L of the guess pulse. For a single-photon pulse, $\omega_L^{(1)} = 23653 \text{cm}^{-1}$. For a three-photon pulse $\omega_L^{(3)} = \omega_L^{(1)}/3$. The factor given in the superscript for three-photon pulses indicates the increase in the intensity compared to a single-photon pulse of the same duration T.

The pulse duration T is given in picoseconds.

ϕ indicates the target phase; the *iters* column gives the number of OCT iterations that were done.

The last four columns show the run results: the fidelity F, the achieved two-qubit phase χ in units of πa, the concurrence, and the vibrational purity on the $|00\rangle$ surface.

Fidelities that were obtained in the reduced optimization scheme are indicated with an asterisk. All other fidelities were obtained in the full optimization scheme. Both the reduced and the full optimization scheme are summarized in Table 4.1.

Run	photons	T [ps]	ϕ	iters	F	χ/π	C	$|00\rangle$ pur.
3220	1	1.23	π	41	0.622	0.162	0.251	0.844
9817	1	1.23	π	50	0.624	0.165	0.256	0.836
3185	1	2.00	π	15	0.639	0.190	0.294	0.807
3250	1	5.00	π	15	0.719	0.354	0.528	0.589
3251	1	8.00	π	15	0.787	0.560	0.780	0.367
3466	1	12.3	π	50	0.779	0.662	0.862	0.229
3464	1	15.0	π	25	0.774	0.773	0.937	0.141
4764	1	15.0	π	200	0.773*	0.784	0.943	0.343
3189	1	30.0	π	4	0.630	0.174	0.270	0.014
2846	1	50.0	π	10	0.653	0.266	0.405	0.000
4646	1	150.0	π	20	0.898*	0.982	1.000	0.639
9464	1	290.0	π	70	0.984*	1.004	1.000	0.936
9268	1	430.0	π	40	0.998*	0.998	1.000	0.991
9104	1	800.0	π	30	0.999*	0.998	1.000	0.997
Partial Phasegate								
2853	1	1.23	$\pi/3$	200	0.955	0.064	0.102	0.964
2854	1	1.23	$\pi/2$	200	0.890	0.066	0.104	0.963
3426	1	5.00	$\pi/3$	40	0.924	0.259	0.396	0.608
Three-Photon-Pulses								
3501	$3^{(\times 10)}$	1.23	π	50	0.500	0.000	0.001	1.000
3502	$3^{(\times 100)}$	1.23	π	50	0.618	0.151	0.235	0.885
3503	$3^{(\times 1000)}$	1.23	π	50	0.602	0.131	0.204	0.888
2990	$3^{(\times 1)}$	12.3	π	10	0.430	0.002	0.002	1.000
3173	$3^{(\times 100)}$	12.3	π	10	0.662	0.238	0.365	0.694
4596	$3^{(\times 1000)}$	12.3	π	75	0.752*	0.643	0.847	0.272
8888	3503 extended to 15 ps			300	0.869*	0.780	0.941	0.622
Short Pulses & Small Phases								
4380	$3^{(\times 1000)}$	0.10	$\pi/10$	50	0.995*	0.008	0.012	0.997
4375	$3^{(\times 1000)}$	0.10	$\pi/4$	50	0.970*	0.007	0.012	0.997
4374	1	0.10	$\pi/10$	50	0.996*	0.008	0.013	0.998
4381	1	0.10	$\pi/4$	50	0.947*	0.006	0.010	0.999
9270	$3^{(\times 1000)}$	0.17	$\pi/10$	20000	0.996*	0.016	0.026	0.997
9103	$3^{(\times 1000)}$	0.50	$\pi/10$	10000	0.995*	0.036	0.057	0.989
4383	$3^{(\times 1000)}$	0.50	$\pi/4$	50	0.974*	0.041	0.065	0.980
4376	1	0.50	$\pi/10$	50	0.993*	0.032	0.050	0.983
4377	1	0.50	$\pi/4$	50	0.973*	0.034	0.054	0.983
4585	$3^{(\times 1000)}$	1.23	$\pi/4$	300	0.973*	0.088	0.139	0.944
4593	$3^{(\times 1000)}$	1.23	$\pi/10$	300	0.986*	0.087	0.136	0.946
4378	1	1.23	$\pi/10$	50	0.991*	0.050	0.079	0.969
4379	1	1.23	$\pi/4$	50	0.971*	0.052	0.082	0.963
9808	9270 repeated $\times$ 61			10	0.709*	0.683	0.879	0.250
9809	9103 repeated $\times$ 28			10	0.705*	0.709	0.897	0.229

Bibliography

[1] M. Nielsen and I. L. Chuang, *Quantum Computation and Quantum Information* (Cambridge University Press, 2000).

[2] D. P. DiVincenzo, Fortschr. Phys. **48**, 771 (2000).

[3] M. Greiner, O. Mandel, T. Esslinger, T. W. Hänsch, and I. Bloch, Nature **415**, 39 (2002).

[4] P. S. Jessen and I. H. Deutsch, Adv. At. Mol. Opt. Phys. **36**, 95 (1996).

[5] I. Bloch, Nature Physics **1**, 23 (2005).

[6] S. E. Hamann, D. L. Haycock, G. Klose, P. H. Pax, I. H. Deutsch, and P. S. Jessen, Phys. Rev. Lett. **80**, 4149 (1998).

[7] C. P. Koch, F. Masnou-Seeuws, and R. Kosloff, Phys. Rev. Lett. **94**, 193001 (2005).

[8] W. Yi, A. J. Daley, G. Pupillo, and P. Zoller, New J. Phys. **10**, 073015 (2008).

[9] L. Pasternack, D. R. Yarkony, P. J. Dagdigian, and D. M. Silver, J. Phys. B **13**, 2231 (1980).

[10] O. Mandel, M. Greiner, A. Widera, T. Rom, T. W. Hänsch, and I. Bloch, Nature **425**, 937 (2003).

[11] N. Lundblad, M. Schlosser, and J. V. Porto, Phys. Rev. A **81**, 031611 (2010).

[12] B. Bussery-Honvault, J.-M. Launay, and R. Moszynski, Phys. Rev. A **68**, 032718 (2003).

[13] O. Allard, A. Pashov, H. Knöckel, and E. Tiemann, Phys. Rev. A **66**, 042503 (2002).

[14] C. P. Koch and R. Moszynski, Phys. Rev. A **78**, 043417 (2008).

[15] A. J. Daley, M. M. Boyd, J. Ye, and P. Zoller, Phys. Rev. Lett. **101**, 170504 (2008).

[16] A. V. Gorshkov, A. M. Rey, A. J. Daley, M. M. Boyd, J. Ye, P. Zoller, and M. D. Lukin, Phys. Rev. Lett. **102**, 110503 (2009).

[17] S. Peil, J. V. Porto, B. L. Tolra, J. M. Obrecht, B. E. King, M. Subbotin, S. L. Rolston, and W. D. Phillips, Phys. Rev. A **67**, 051603 (2003).

[18] M. Ohliger, *Thermodynamic properties of spinor bosons in optical lattices*, Diplomarbeit. Freie Universität Berlin (2008), URL `http://users.physik.fu-berlin.de/~pelster/Theses/ohliger.pdf`.

[19] W. Nagourney, J. Sandberg, and H. Dehmelt, Phys. Rev. Lett. **56**, 2797 (1986).

[20] J. C. Bergquist, R. G. Hulet, W. M. Itano, and D. J. Wineland, Phys. Rev. Lett. **57**, 1699 (1986).

[21] T. Sauter, W. Neuhauser, R. Blatt, and P. E. Toschek, Phys. Rev. Lett. **57**, 1696 (1986).

[22] M. A. Finn, G. W. Greenlees, and D. A. Lewis, Opt. Comm. **60**, 149 (1986).

[23] D. J. Tannor, *Introduction to Quantum Mechanics: A Time-Dependent Perspective* (University Science Books, Sausalito, California, 2007).

[24] R. Kosloff, J. Chem. Phys. **92**, 2087 (1988).

[25] C. E. Shannon, Proc. IRE **37**, 10 (1949).

[26] M. Nest and H.-D. Meyer, Chem. Phys. Lett. **352**, 486 (2002).

[27] E. Fattal, R. Baer, and R. Kosloff, Phys. Rev. E **53**, 1217 (1996).

[28] V. Kokoouline, O. Dulieu, R. Kosloff, and F. Masnou-Seeuws, J. Chem. Phys. **110**, 9865 (1999).

[29] K. Willner, O. Dulieu, and F. Masnou-Seeuws, J. Chem. Phys. **120**, 548 (2004).

[30] S. Kallush and R. Kosloff, Chem. Phys. Lett. **433**, 221 (2006).

[31] M. Feit, J. F. Jr., and A. Steiger, J. Comput. Phys. **47**, 412 (1982).

[32] H. Tal-Ezer and R. Kosloff, J. Chem. Phys. **81**, 3967 (1984).

[33] M. Abramowitz and I. A. Stegun, *Handbook of Mathematical Functions* (Dover, 1972), 9th ed.

[34] R. Kosloff and H. Tal-Ezer, Chem. Phys. Lett. **127**, 223 (1986).

[35] S. E. Sklarz and D. J. Tannor, Phys. Rev. A **66**, 053619 (2002).

[36] J. P. Palao, R. Kosloff, and C. P. Koch, Phys. Rev. A **77**, 063412 (2008).

[37] C. P. Koch, J. P. Palao, R. Kosloff, and F. Masnou-Seeuws, Phys. Rev. A **70**, 013402 (2004).

[38] J. Zhang, J. Vala, S. Sastry, and K. B. Whaley, Phys. Rev. A **67**, 042313 (2003).

[39] B. Kraus and J. I. Cirac, Phys. Rev. A **63**, 062309 (2001).

[40] J. P. Palao and R. Kosloff, Phys. Rev. A **68**, 062308 (2003).

[41] D. Jaksch, J. I. Cirac, P. Zoller, S. L. Rolston, R. Côté, and M. D. Lukin, Phys. Rev. Lett. **85**, 2208 (2000).

[42] A. Gaëtan, Y. Miroshnychenko, T. Wilk, A. Chotia, M. Viteau, D. Comparat, P. Pillet, A. Browaeys, and P. Grangier, Nature Physics **5**, 115 (2009).

[43] D. A. Steck, *Rubidium 87 D Line Data* (2009), URL `http://steck.us/alkalidata`.

[44] H. Haken and H. C. Wolf, *Molecular Physics and Elements of Quantum Chemistry* (Springer, 2003), 4th ed.

Erklärung:

Ich versichere, dass ich diese Arbeit selbständig verfasst und keine anderen als die angegebenen Quellen und Hilfsmittel benutzt habe.

_____   _____
Ort, Datum   Unterschrift